

M2LW-23OR04020311

Light Water Reactor Sustainability Program

FY 2023 Progress on Stress Corrosion Crack Testing of Ni-Base Alloys in PWR Primary Water



August 2023

U.S. Department of Energy
Office of Nuclear Energy

DISCLAIMER

This information was prepared as an account of work sponsored by an agency of the U.S. Government. Neither the U.S. Government nor any agency thereof, nor any of their employees, makes any warranty, expressed or implied, or assumes any legal liability or responsibility for the accuracy, completeness, or usefulness, of any information, apparatus, product, or process disclosed, or represents that its use would not infringe privately owned rights. References herein to any specific commercial product, process, or service by trade name, trade mark, manufacturer, or otherwise, does not necessarily constitute or imply its endorsement, recommendation, or favoring by the U.S. Government or any agency thereof. The views and opinions of authors expressed herein do not necessarily state or reflect those of the U.S. Government or any agency thereof.

FY 2023 Progress on Stress Corrosion Crack Testing of Ni-Base Alloys in PWR Primary Water

**Ziqing Zhai
Ferdinan C. Colon
Mychailo B. Toloczko**

August 2023

**Prepared for the
U.S. Department of Energy
Office of Nuclear Energy**

ABSTRACT

This report documents the research progress accomplished in FY 2023 in two topic areas. The first part of this report documents the final year progress of a three-year research effort on evaluating the stress corrosion cracking (SCC) initiation and growth behavior of Ni-base alloys in lithium hydroxide (LiOH) vs. potassium hydroxide (KOH)-containing PWR primary water. The material types and the specific water chemistry conditions evaluated in this research were selected based on discussions with EPRI, who is assisting the U.S. pressurized water reactor utilities in a potential transition from LiOH to KOH. In FY 2023, the testing focused on the last material to evaluate – a first-generation Ni-base weld metal Alloy 82. Direct comparisons of SCC initiation and crack growth behavior were made on Alloy 82 in a LiOH vs. KOH-containing environment, followed by post-test characterizations and statistical analysis. Results suggest that replacing LiOH with KOH as the pH moderator in PWR primary water would not adversely impact the SCC initiation and propagation behavior of Alloy 82. The second part of this report provides a status update of the ongoing Phase V long-term SCC initiation testing on cold-worked Alloy 690 materials, where the effect of key material, mechanical, and environmental factors on the long-term grain boundary degradation and crack initiation behavior of Alloy 690 are being evaluated in state-of-the-art SCC initiation testing systems equipped with in-situ detection of macroscopic crack initiation. A detailed summary of the microscopy analyses performed in FY 2023 is also provided to evaluate precursor damage and crack evolution in all tested Alloy 690 specimens after Phase IV exposure. Insights obtained from the latest testing and characterization results are discussed to facilitate the prediction of Alloy 690 degradation in service-relevant conditions.

ACKNOWLEDGEMENTS

The authors gratefully acknowledge the financial support from U.S. Department of Energy, Office of Nuclear Energy, through the Light Water Reactor Sustainability Program Materials Research Pathway. In addition, support is recognized from EPRI for technical guidance on material selection and determination of test methods and the U.S. Nuclear Regulatory Commission for providing test systems for the SCC growth rate testing performed in this study. Dr. Dave Morton from the Naval Nuclear Laboratory is acknowledged for providing the Alloy 82 material used for the SCC testing in LiOH vs. KOH-containing PWR primary water. The authors would also like to acknowledge Dr. Peter Andresen (formerly with GE Global Research Center and currently with Andresen Consulting) for helpful discussions on testing ideas. Dr. Jia Liu and Dr. Karen Kruska at Pacific Northwest National Laboratory (PNNL) are recognized for performing FIB serial milling on selected Alloy 690 specimens. Key technical assistance from Javier Gutierrez, Robert Fluor, Anthony Guzman, and Michael Blazon at PNNL is acknowledged for testing and materials preparation activities.

CONTENTS

ABSTRACT.....	ii
ACKNOWLEDGEMENTS.....	iii
ACRONYMS.....	xiv
1. Project Background.....	1
1.1 Objective.....	1
1.2 Focus of Current Report.....	1
2. Evaluation of the SCC Initiation and Crack Growth Behavior of Alloy 82 in KOH vs. LiOH-Containing PWR Primary Water.....	2
2.1 Chapter Overview.....	2
2.2 Experimental Methods.....	2
2.2.1 SCC Initiation Test Systems and Testing Approach.....	2
2.2.2 SCC Crack Growth Test Systems and Testing Approach.....	6
2.2.3 Material and specimen preparation.....	11
2.3 SCC Initiation Behavior of Alloy 82 in KOH vs. LiOH-Containing PWR Primary Water.....	15
2.3.1 Test Procedure and DCPD Response.....	15
2.3.2 Post-Test Cracking Morphology.....	19
2.4 SCC Crack Growth Behavior of Alloy 82 in KOH vs. LiOH-Containing PWR Primary Water.....	27
2.4.1 In-Situ Crack Growth Rate Response.....	28
2.4.2 Post-Test Fractography Examination.....	39
2.5 Discussion.....	41
3. Update on the Long-Term SCC Initiation Testing of Cold Worked Alloy 690.....	45
3.1 Chapter Overview.....	45
3.2 Materials and Specimen Preparation.....	45
3.2.1 Alloy 690 Materials and Pre-Test Microstructures.....	45
3.3 Test Update.....	53
3.3.1 Test Overview.....	53
3.3.2 Characterization of Precursor Damage and Crack Evolution in Cold Worked Alloy 690.....	62
3.4 Discussion.....	76
3.4.1 Current Knowledge.....	76
3.4.2 Future Plans.....	79
4. Summary and Conclusions.....	80
REFERENCES.....	81

FIGURES

Figure 1. PNNL initiation specimen design. The gauge diameter is selected based on material strength and can vary from 2.75-4.5 mm (0.11-0.18 inches). The gauge length is set at 4.0 mm (0.157 inches). Overall height is 30.5 mm (1.2 inches). Illustrated dimensions are in inch units.....	2
Figure 2. The load trains used at PNNL in the (a) medium-size SCC initiation test system with a capacity of testing up to 6 fully instrumented specimens and the (b) large-size SCC initiation test system with a capacity of testing up to 24 instrumented specimens and up to 36 specimens in total.....	4
Figure 3. Example of stress versus strain plot during the initial loading of tensile specimens for SCC initiation testing. The displacement in the actuator and the total load is plotted in the secondary x (upper) and y (right) axis, respectively.	5
Figure 4. Non-referenced and referenced DCPD strain response for IN052, an 8% CW specimen from Alloy 600MA plate heat NX6106XK-11.	5
Figure 5. The typical SCCGR test system used at PNNL.	7
Figure 6. Schematic drawing of a 0.5T CT specimen. Oversized loading holes (~9.5 mm diameter) are used to accommodate ceramic inserts that provide electrical isolation between the CT specimen and clevises.....	8
Figure 7. Simplified schematic of the modified water board setup for on-the-fly chemistry changes used in the SCCGR test system. The red arrows indicate the direction of the water flow.	10
Figure 8. The as-received Alloy 82H (Heat 21719-2) block for this study.....	12
Figure 9. Schematic of the A82 block cutting plan for specimen preparation.	13
Figure 10. Examples of pre-existing welding defects observed on the gauge surface of several 30% CF Alloy 82 initiation specimens after they were polished to a colloidal silica finish.	14
Figure 11. Non-referenced DCPD strain response of the four 30%CF Alloy 82 specimens IN445-48 tested at material yield stress in 360°C PWR primary water containing 1500 ppm B and 2.2 ppm Li.	15
Figure 12. The stress vs. strain plot during the initial loading of the six 15%CF Alloy 82 specimens IN479-84 in 360°C PWR primary water containing 1500 ppm B and 12.4 ppm K.....	16
Figure 13. The stress vs. strain plot during the initial loading of the six 15%CF Alloy 82 specimens IN485-90 in 360°C PWR primary water containing 1500 ppm B and 2.2 ppm Li.....	16
Figure 14. Overall non-referenced DCPD strain response of the six 15%CF Alloy 82 specimens IN479-84 tested at material yield stress in 360°C PWR primary water containing 1500 ppm B and 12.4 ppm K. The SCC initiation time of each specimen is marked in the legend.	18
Figure 15. Overall non-referenced DCPD strain response of the six 15%CF Alloy 82 specimens IN479-84 tested at material yield stress in 360°C PWR primary water containing 1500 ppm B and 2.2 ppm Li. The SCC initiation time of each specimen is marked in the legend.	18

Figure 16. SCC initiation time of all the tested 15%CF Alloy 82 specimens as a function of total plastic strain accumulated during every loading run.....	19
Figure 17. SCC initiation time of all the tested 15%CF Alloy 82 specimens as a function of applied stress.....	19
Figure 18. Post-test SEM-BSE montage of the first initiated 15%CF Alloy 82 specimen IN480 in 360°C PWR primary water with 1500 ppm B and 12.4 ppm K.....	20
Figure 19. Post-test SEM-BSE montage of the second initiated 15%CF Alloy 82 specimen IN483 in 360°C PWR primary water with 1500 ppm B and 12.4 ppm K.....	21
Figure 20. Post-test SEM-BSE montage of the third initiated 15%CF Alloy 82 specimen IN482 in 360°C PWR primary water with 1500 ppm B and 12.4 ppm K.....	21
Figure 21. Post-test SEM-BSE montage of the fourth initiated 15%CF Alloy 82 specimen IN484 in 360°C PWR primary water with 1500 ppm B and 12.4 ppm K.....	22
Figure 22. Post-test SEM-BSE montage of the fifth initiated 15%CF Alloy 82 specimen IN479 in 360°C PWR primary water with 1500 ppm B and 12.4 ppm K.....	22
Figure 23. Post-test SEM-BSE montage of the six initiated 15%CF Alloy 82 specimen IN481 in 360°C PWR primary water with 1500 ppm B and 12.4 ppm K.....	23
Figure 24. Post-test SEM-BSE montage of the first initiated 15%CF Alloy 82 specimen IN485 in 360°C PWR primary water with 1500 ppm B and 2.2 ppm Li.....	24
Figure 25. Post-test SEM-BSE montage of the second initiated 15%CF Alloy 82 specimen IN487 in 360°C PWR primary water with 1500 ppm B and 2.2 ppm Li.....	24
Figure 26. Post-test SEM-BSE montage of the third initiated 15%CF Alloy 82 specimen IN486 in 360°C PWR primary water with 1500 ppm B and 2.2 ppm Li.....	25
Figure 27. Post-test SEM-BSE montage of the fourth initiated 15%CF Alloy 82 specimen IN489 in 360°C PWR primary water with 1500 ppm B and 2.2 ppm Li.....	25
Figure 28. Post-test SEM-BSE montage of the fifth initiated 15%CF Alloy 82 specimen IN488 in 360°C PWR primary water with 1500 ppm B and 2.2 ppm Li.....	26
Figure 29. Post-test SEM-BSE montage of the non-initiated 15%CF Alloy 82 specimen IN490 in 360°C PWR primary water with 1500 ppm B and 2.2 ppm Li.....	26
Figure 30. Optical micrographs of the polished side grooves of the 30%CF Alloy 82 specimen CT228. The length of the precrack produced by air fatigue is marked in both side grooves.....	27
Figure 31. Optical micrographs of the polished side grooves of the 30%CF Alloy 82 specimen CT229. The length of the precrack produced by air fatigue is marked in both side grooves.....	27
Figure 32. Test overview of crack growth response in the two Alloy 82 specimens CT228 & 229 tested in T-S orientation. The effect of KOH vs. LiOH on the SCCGR of both specimens was evaluated in 360°C simulated PWR primary water at a constant stress intensity of 30 MPa \sqrt{m}	29
Figure 33. Crack growth response of CT228 & 229 during the initial cyclic loading transition steps in 360°C simulated PWR primary water.....	30

Figure 34. SCCGR response of CT228 & 229 in 360°C PWR primary water BOC chemistry with on-the-fly changes between LiOH and KOH. The concentrations of B, Li, and K in the plot are shown in ppm.....	30
Figure 35. SCCGR response of CT228 & 229 in 360°C PWR primary water during the transition from BOC LiOH to EOC LiOH water chemistry.	31
Figure 36. Crack growth response of CT228 & 229 during the first attempt to adjust crack growth behavior after the water chemistry change from BOC LiOH to EOC LiOH.....	31
Figure 37. The 2 nd attempt to measure SCCGR response of CT228 & 229 in 360°C PWR primary water EOC LiOH water chemistry.....	32
Figure 38. Crack growth response of CT228 & 229 during the second attempt to adjust crack growth behavior in the EOC LiOH water chemistry.	32
Figure 39. The 2 nd attempt to measure the SCCGR response of CT228 & 229 in 360°C PWR primary water EOC water chemistry with on-the-fly changes between LiOH and KOH.....	33
Figure 40. Crack length measurement in the side grooves of CT228 after 6929 hours of testing in 360°C simulated PWR primary water: (a) immediately after the specimen was removed from testing and (b) after additional fatigue in air to grow the crack in the specimen.	34
Figure 41. Crack length measurement in the side grooves of CT229 after 6929 hours of testing in 360°C simulated PWR primary water: (a) immediately after the specimen was removed from testing and (b) after additional fatigue in air to grow the crack in the specimen.	34
Figure 42. CGR response of CT228 & 229 in transition steps after the specimens were fatigued in air for the 1 st time to adjust the crack length.....	35
Figure 43. The 3 rd attempt to measure the SCCGR response of CT228 & 229 in 360°C PWR primary water EOC LiOH water chemistry.....	35
Figure 44. Crack length measurement in the side grooves of CT228 after 8076 hours of testing in 360°C simulated PWR primary water: (a) immediately after the specimen was removed from testing and (b) after additional fatigue in air to grow the crack in the specimen.	36
Figure 45. Crack length measurement in the side grooves of CT229 after 8076 hours of testing in 360°C simulated PWR primary water: (a) immediately after the specimen was removed from testing and (b) after additional fatigue in air to grow the crack in the specimen.	37
Figure 46. CGR response of CT228 & 229 in transition steps after the specimens were fatigued in air for the 2 nd time to adjust the crack length.	37
Figure 47. SCCGR response of CT228 & 229 in 360°C PWR primary water EOC chemistry with on-the-fly changes between LiOH and KOH.....	38
Figure 48. SCCGR response of CT228 & 229 in 360°C PWR primary water with on-the-fly changes from EOC LiOH to mid-cycle water chemistry.	38
Figure 49. Post-test optical image of the crack growth surface in the 2/3-thickness slice of CT228. The extent of the fatigue pre-crack is highlighted by the blue dotted line. The average pre-crack length and environmental crack length are marked in yellow on the left.	40

Figure 50. Post-test SEM BSE image showing the crack morphology in the cross-section of the 1/3-thickness slice sectioned from CT228.	40
Figure 51. Post-test optical image of the crack growth surface in the 2/3-thickness slice of CT229. The extent of the fatigue pre-crack is highlighted by the blue dotted line. The average pre-crack length and environmental crack length are marked in yellow on the left.	41
Figure 52. Post-test SEM BSE image showing the crack morphology in the cross-section of the 1/3-thickness slice sectioned from CT229.	41
Figure 53. Standard Weibull analysis (cumulative failure vs. hours) with a 95% confidence interval based on the SCC initiation times acquired on Alloy 82 at yield stress in 360°C water with 1500 ppm B and 12.4 ppm K. All six specimens have initiated and are considered failures in this analysis.	42
Figure 54. Non-censored (standard) Weibull analysis (cumulative failure vs. hours) with a 95% confidence interval based on the SCC initiation times acquired on Alloy 82 at yield stress in 360°C water with 1500 ppm B and 2.2 ppm Li. This fit only takes into account the five initiated specimens as failures. The non-initiated sample is excluded from this analysis.	43
Figure 55. Censored Weibull analysis (cumulative failure vs. hours) with a 95% confidence interval based on the SCC initiation times acquired on Alloy 82 at yield stress in 360°C water with 1500 ppm B and 2.2 ppm Li. Five out of the six specimens have initiated and are considered failures in this analysis. This censored analysis also accounts for the one non-failure event.	43
Figure 56. Illustration showing the orientation of specimens and cold work direction in the Alloy 690 materials.	47
Figure 57. SCCGR response of TT/MA Alloy 690 materials at ~ 30 MPa \sqrt{m} acquired from the NRC SCC crack growth program [7, 22]. The heat and cold work levels selected for SCC initiation evaluation at each stage were checked in the label box and circled in the plots.	47
Figure 58. SEM-BSE images illustrating the GB microstructures for the three Alloy 690TT CRDM materials in the as-received condition.	48
Figure 59. SEM-BSE images illustrating differences in the GB carbide microstructures for each of the four Alloy 690 plate/bar materials in the as-received condition.	49
Figure 60. EBSD pattern quality maps showing the general microstructure and grain size for the seven Alloy 690TT/MA materials in the as-received condition.	50
Figure 61. SEM-BSE images illustrating the permanent damage (highlighted by arrows) induced by cold work in four 31%CF Alloy 690TT materials. All images are shown at the same scale.	51
Figure 62. Representative pre-existing defect distribution in the thermally treated Valinox CRDM material cold forged to 12, 21, and 31% reduction in thickness.	52
Figure 63. Up-to-date exposure time of the CW Alloy 690 materials evaluated in the long-term SCC initiation testing under LWRS. The arrows suggest that the test is ongoing as of August 2023 for the specified material and cold work conditions.	54
Figure 64. Non-referenced DCPD strain response during the Phase IV exposure, indicating macroscopic crack initiation in the Sumitomo CRDM TT+31%CF specimen IN179	

tested at 0.9 YS initiated after 31,645 hours of exposure in 360 °C PWR primary water.....	57
Figure 65. Overall non-referenced DCPD strain response during the Phase V exposure for all the specimens monitored in the LWRS1 (36-specimen) SCC initiation test system in 360 °C PWR primary water. The test is ongoing as of August 2023. Specimens are all being tested at materials yield stress unless otherwise specified.	58
Figure 66. Non-referenced DCPD strain response during the Phase V exposure for the specimens introduced in Phase I and monitored in the LWRS1 (36-specimen) test system in 360 °C PWR primary water. The test is ongoing as of August 2023.....	58
Figure 67. Non-referenced DCPD strain response during the Phase V exposure for the specimens introduced in Phase II and monitored in the LWRS1 (36-specimen) test system in 360 °C PWR primary water. The test is ongoing as of August 2023.....	59
Figure 68. Non-referenced DCPD strain response during the Phase V exposure for the specimens introduced in Phase III and monitored in the LWRS1 (36-specimen) test system in 360 °C PWR primary water. The test is ongoing as of August 2023.....	59
Figure 69. Non-referenced DCPD strain response during the Phase V exposure for the specimens introduced in Phase IV and monitored in the LWRS1 (36-specimen) test system in 360 °C PWR primary water. The test is ongoing as of August 2023.....	60
Figure 70. Overall non-referenced DCPD strain response during the Phase V exposure for all the specimens monitored in the LWRS2 (6-specimen) SCC initiation test system in 360 °C PWR primary water. The test is ongoing as of August 2023.....	61
Figure 71. Overall referenced DCPD strain response during the Phase V exposure for all the specimens monitored in the LWRS2 (6-specimen) SCC initiation test system in 360 °C PWR primary water. The test is ongoing as of August 2023.....	61
Figure 72. (a) Creep strain rates and (b) resistivity evolution as a function of applied stress of the six specimens tested in LWRS2. The strain rates were calculated based on their DCPD response up to ~5830 hours of exposure during Phase V. The test is ongoing as of August 2023.	62
Figure 73. SEM-BSE images of (a) the gauge cross-section of the TT+31% CF Valinox CRDM specimen IN037 removed after DCPD detected crack initiation. Aggregations of GB cavities are highlighted in yellow and continuous IG cracks in red, with higher magnification IG damage examples (b) inside the specimen and (c) near the surface.	64
Figure 74. SEM-BSE images of the representative surface and cross-section morphology of IG damage found in the TT+31% CF Sumitomo CRDM specimen IN179 after 2.1 (left) and 3.4 (right) years of exposure in 360°C simulated PWR primary water. GB cavities are highlighted in yellow in the FIB trench cross-sections.	65
Figure 75. SEM-BSE montage images of the evolution of surface-breaking IG cracks (highlighted in red) found on the gauge surface of the TT+31% CF Sumitomo CRDM specimen IN179 before (left) and after (right) DCPD detection of crack initiation.	66
Figure 76. SEM-BSE montage images of the IG cracks (marked in red) observed on the TT+31% CF Doosan CRDM specimen IN039 after 4.2 years of exposure in 360°C simulated PWR primary water (right). The surface morphology evolution of the IG crack found after 4.2 years at the marked site is also presented (left).	67

Figure 77. Low-kV FIB-SE images taken during FIB serial milling on the IG crack highlighted in Figure 76 in the TT+31% CF Doosan CRDM specimen IN039 after 4.2 years of exposure at 100% yield stress in 360°C simulated PWR primary water.	67
Figure 78. (a) SEM-BSE image of representative surface morphology of the HAGBs in the SA+31%CF Valinox CRDM specimen IN175 after 4.1 years of exposure at 100% yield stress in 360°C simulated PWR primary water. (b) Low-kV FIB-SE images taken during FIB serial milling on a segment of HAGB highlighted in (a).....	68
Figure 79. Distribution of surface-breaking IG cracks (marked in red) and possible cracks (marked in green) observed on the gauge surface of the TT+21% CF Sumitomo CRDM specimen IN024 tested at 100% YS after 4.2 years of exposure in 360°C simulated PWR primary water (upper right). Higher-magnification SEM-BSE images are also shown for the evolution of IG damage on a selected site from 2.1–4.2 years of exposure.	70
Figure 80. Low-kV FIB-SE images taken during FIB serial milling on (a) the IG crack identified in Site 1 in Figure 81 and (b) a random HAGB without surface-breaking crack in the gauge section of the 1 μm finish, TT+21%CF Sumitomo CRDM specimen IN024 tested at 100% YS after Phase IV (4.2 years) exposure in 360°C simulated PWR primary water.	70
Figure 81. Distribution of surface-breaking IG cracks (marked in red) and possible cracks (marked in green) observed on the gauge surface of the TT+21% CF Valinox CRDM specimen IN027 tested at 100% YS after 4.2 years of exposure in 360°C simulated PWR primary water (upper right). Higher-magnification SEM-BSE images are also shown for the evolution of IG damage on three selected sites from 2.1–4.2 years of exposure.	71
Figure 82. Low-kV FIB-SE images taken during FIB serial milling on a selected GB in the gauge section of the 1 μm finish, TT+21%CF Valinox CRDM specimen IN027 tested at 100% YS after Phase III (3.2 years) exposure in 360°C simulated PWR primary water. GB cavities revealed at the cross-sections are highlighted with arrows.	73
Figure 83. Selected low-kV FIB-SE images taken during FIB serial milling on the IG crack identified in Site 1 in Figure 81 in the gauge section of the TT+21%CF Valinox CRDM specimen IN027 tested at 100% YS after 4.2 years exposure in 360°C simulated PWR primary water. GB cavities revealed at the cross-sections are highlighted with arrows.	73
Figure 84. Distribution of possible IG cracks (marked in green) observed on the gauge surface of the TT+21.6% CF Doosan CRDM specimen IN030 tested at 100% YS after 5.1 years of exposure in 360°C simulated PWR primary water in (a). (b, c) Video of cross-sections revealed during serial FIB trenching on two possible IG cracks.	74
Figure 85. SEM-BSE montage images of surface-breaking IG cracks (marked in red) and possible cracks (marked in green) observed on the TT+11.7% CF Valinox CRDM specimen IN065 tested at 100% YS after 4.9 years of exposure in 360°C simulated PWR primary water (left). Selected cross-sections revealed during serial FIB trenching are also shown for one obvious crack (upper right) and one uncracked GB (lower right).	76
Figure 86. Summary of precursor morphology and crack mechanism observed in the long-term tested CW Alloy 690 SCC initiation specimens as a function of starting microstructure and cold work level.	78

Figure 87. The first occurrence of surface-breaking IG cracks observed in the Alloy 690TT Valinox CRDM material as a function of exposure time. Key characteristics of the cracks were also summarized..... 78

Figure 88. Crack initiation or total exposure time of all the tested Alloy 690 materials as a function of applied stress. 79

TABLES

Table 1. Nominal PWR primary water chemistries identified by EPRI for the KOH vs. LiOH study.	9
Table 2. Environmental parameter tracking at each autoclave volume exchange during the trial on-the-fly water chemistry changeover from 1500 ppm B/2.2 ppm Li to 1500 ppm B/12.4 ppm K.	11
Table 3. Chemical composition (wt. %) of Alloy 82H Heat 21719-2 in comparison to the Alloy 82H specifications.	11
Table 4. Summary of the SCC initiation test status of the 15%CF Alloy 82 specimens.	17
Table 5. Mean, standard deviation, and failure times at lower and upper 95% confidence intervals for 10%, 50%, and 90% cumulative failures of Alloy 82. The mean and standard deviation for the LiOH water chemistry were calculated with the inclusion of the non-initiated value.	44
Table 6. Average SCCGR measured by DCPD in each water chemistry tested for CT228 and CT229.	44
Table 7. Percentage change in SCCGR during the last 200 hours before and the first 200 hours after on-the-fly change between LiOH and KOH in the BOC and EOC water chemistries for the Alloy 82 CT specimens.	44
Table 8. Composition of the AR Alloy 690 materials.	46
Table 9. Heat treatment and mechanical properties of the AR Alloy 690 materials (RT: room temperature, WQ: water quenched, AC: air cool, NM: not measured).	46
Table 10. Summary of grain size and carbide distributions for materials selected for SCC initiation testing.	50
Table 11. Summary of carbide microstructure and damage morphology in Alloy 690TT CRDM materials in different cold work levels evaluated in the SCC initiation test.	53
Table 12. Summary of carbide microstructure and damage morphology in Alloy 690 plate and bar materials in different cold work levels evaluated in the SCC initiation test.	53
Table 13. Summary of material condition and SCC initiation testing status of all the tested Alloy 690 specimens as of August 2023.	55
Table 14. Summary of the GB microstructure, pre-existing damage, and IG precursor damage status for all the Alloy 690 materials tested in highly cold worked conditions. Cells highlighted in orange in the last column are new observations made after Phase IV exposure.	64
Table 15. Summary of the GB microstructure, pre-existing damage, and IG precursor damage status for all the Alloy 690 materials tested in moderately CW conditions. Cells highlighted in orange in the last column are new observations gained after Phase IV exposure.	69
Table 16. Summary of the GB microstructure, pre-existing damage, and IG precursor damage status for all the Alloy 690 materials tested in low CW conditions. Cells highlighted in orange in the last column are new observations made after Phase IV exposure.	75

ACRONYMS

AR	As received
ASTM	American Society for Testing and Materials
BOC	Beginning-of-cycle
BSE	Backscatter electron
CF	cold-forged
CGR	Crack growth rate
CRDM	Control rod drive mechanism
CR	Cold-rolled
CT	Compact tension
CW	Cold-worked
DCPD	Direct current potential drop
DIGM	Diffusion-induced grain boundary migration
EBSA	Electron backscatter diffraction
EOC	End-of-cycle
EPRI	Electric Power Research Institute
FIB	Focused ion beam
FY	Fiscal year
GB	Grain boundary
HAGB	High-angle grain boundary
IG	Intergranular
K	Stress intensity
KOH	Potassium hydroxide
LiOH	Lithium hydroxide
LWR	Light water reactor
MA	Mill-annealed
NNL	Naval Nuclear Laboratory
NRC	Nuclear Regulatory Commission
PNNL	Pacific Northwest National Laboratory
PWHT	Post-weld heat treatment
PWR	Pressurized water reactor
SA	Solution-annealed
SCC	Stress corrosion cracking
SCCGR	Stress corrosion crack growth rate

SEM	Scanning electron microscopy
SGB	Solidification grain boundary
TG	Transgranular
TT	Thermally-treated
YS	Yield stress

FY 2023 Progress on Stress Corrosion Crack Initiation Test of Ni-Base Alloys in PWR Primary Water

1. Project Background

1.1 Objective

The first objective of the LWRS task at Pacific Northwest National Laboratory (PNNL) is to identify underlying mechanisms controlling stress corrosion cracking (SCC) initiation and other possible long-term degradation modes that can potentially degrade SCC resistance in Ni-base alloys. Understanding and modeling the fundamental processes causing crack nucleation is a key step in predicting and mitigating SCC in the primary and secondary water systems of light water reactors (LWRs). It is also important to understand the long-term microstructural stability and performance of these alloys as a crucial step moving forward to fulfill their promise for broader applications in LWRs. Mechanistic information obtained could provide key insights to mitigate or control SCC in these materials, optimize inspection and maintenance schedules for the most susceptible materials and locations, and potentially define SCC-resistant materials. The second objective of this task is to evaluate the impact of emerging technologies proposed for sustaining reliable and economical operation of LWRs on SCC resistance of Ni-base alloys. The research scope is defined with regulatory and industry needs and is linked to state-of-the-art laboratory testing and microscopic characterizations.

1.2 Focus of Current Report

This report documents the research progress accomplished in fiscal year (FY) 2023 on two topic areas. The first part of this report (Chapter 2) documents the final year progress of a three-year research effort on evaluating the SCC initiation and growth behavior of Ni-base alloys in lithium hydroxide (LiOH) vs. potassium hydroxide (KOH)-containing PWR primary water. The material types and the specific water chemistry conditions evaluated in this research were selected based on discussions with the Electric Power Research Institute (EPRI), who is assisting the U.S. pressurized water reactor (PWR) utilities in a potential transition from LiOH to KOH. Direct comparisons of SCC initiation and crack growth behavior were made on Alloy 82 in a LiOH vs. KOH-containing environment to assess whether the change in water chemistry impacts the crack initiation and propagation behavior of this Ni-based weld metal. The second part of this report (Chapter 3) provides a status update of the ongoing Phase V long-term SCC initiation testing on cold-worked (CW) Alloy 690 materials, where the effect of key material, mechanical, and environmental factors on the long-term grain boundary (GB) degradation and crack initiation behavior of Alloy 690 are being evaluated in state-of-the-art SCC initiation testing systems equipped with in-situ detection of macroscopic crack initiation. A detailed summary of the microscopy analyses performed in FY 2023 is also provided to evaluate precursor damage and crack evolution in all tested Alloy 690 specimens after Phase IV exposure. Insights obtained from the latest testing and characterization results are discussed to facilitate the prediction of Alloy 690 degradation in service-relevant conditions.

2. Evaluation of the SCC Initiation and Crack Growth Behavior of Alloy 82 in KOH vs. LiOH-Containing PWR Primary Water

2.1 Chapter Overview

The cost and availability of Li-7 have created an interest in using KOH to replace LiOH for primary system pH control in PWRs. A key concern regarding using KOH is its potential effect on the structural materials employed in the reactor internals, especially on Ni-base alloys with limited prior experience with exposure to KOH water chemistry. In collaboration with an ongoing EPRI-led qualification program to determine if KOH PWR water chemistry is acceptable from a materials degradation perspective as compared to LiOH PWR water chemistry, PNNL is performing supporting tests under LWRS to investigate whether replacing LiOH with KOH has a negative impact on the SCC behavior of Ni-base alloys. The testing materials and water chemistries were determined together with EPRI. SCC testing began in FY 2021 on two high-strength Ni-base Alloy X-750 and Alloy 718, and the results were summarized in two previous milestone reports [1, 2]. In this chapter, the SCC initiation and crack growth testing activities on Alloy 82, the last material evaluated in this task, will be reported in detail. The effect of replacing LiOH with KOH as the pH moderator in PWR primary water on the SCC behavior of Alloy 82 will be discussed based on results obtained from SCC testing, post-test characterization, and statistical analysis.

2.2 Experimental Methods

2.2.1 SCC Initiation Test Systems and Testing Approach

The SCC initiation testing is performed in state-of-the-art multi-specimen autoclave systems equipped with an active loading unit, a flow loop for water chemistry control, and in-situ direct current potential drop (DCPD) monitoring for crack initiation.

30.4 mm (1.2-inch) tall uniaxial tensile specimens are used for the tests (Figure 1). All specimens have an identical gauge length of 4 mm. A precision servo-electric load control system applies the load on the loading string(s) using a target load of 4670 N (~1050 lbs). Different stress levels can be achieved by varying the gauge diameter in the specimens loaded in the same string, allowing multiple specimens to be tested at their yield stress (YS) or any other target stress. For most specimens, a 1 μm surface finish was prepared to facilitate the examination of precursor damage and cracks on the surface.

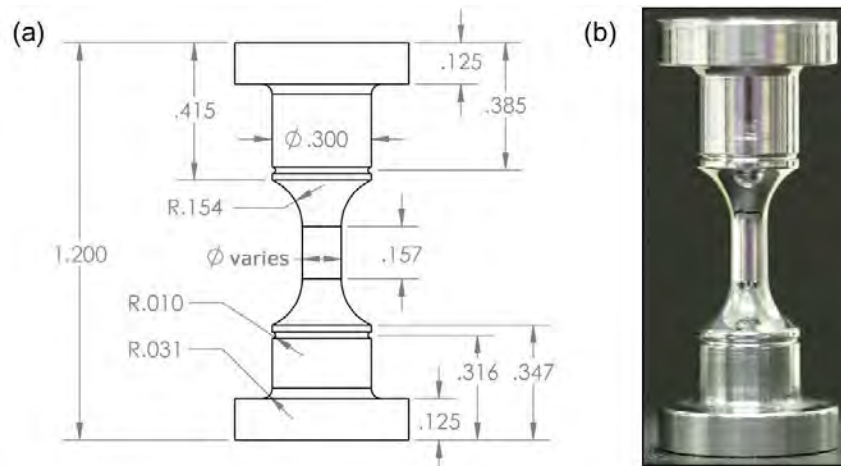
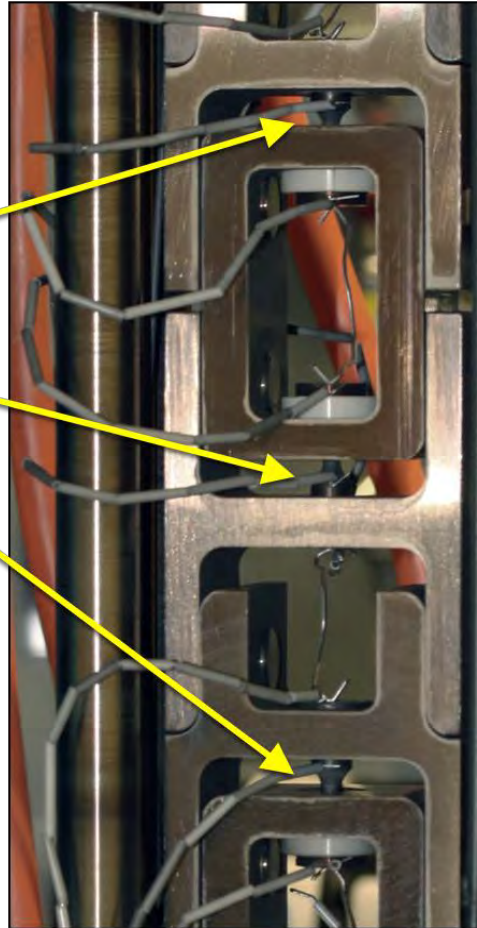
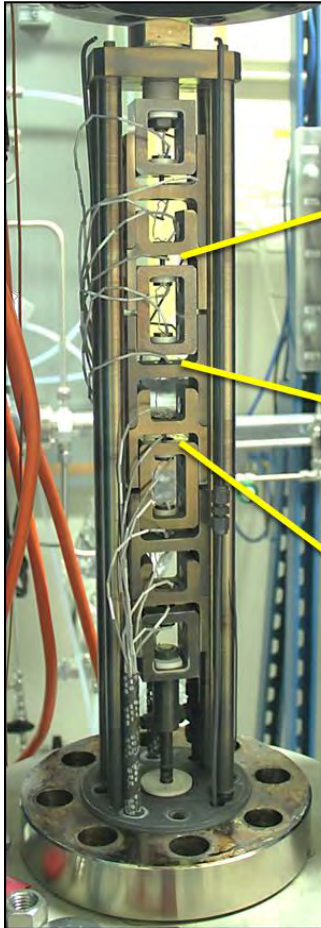


Figure 1. PNNL initiation specimen design. The gauge diameter is selected based on material strength and can vary from 2.75-4.5 mm (0.11-0.18 inches). The gauge length is set at 4.0 mm (0.157 inches). Overall height is 30.5 mm (1.2 inches). Illustrated dimensions are in inch units.

Figure 2 shows the load train and DCPD instrumentation for the serially loaded SCC initiation specimens set up at PNNL. Currently, two medium-size SCC initiation systems and one large SCC initiation system are being used under the scope of LWRS. The two medium-size systems each can test up to 6 fully instrumented specimens, and the large SCC initiation system allows 36 specimens to be tested simultaneously with up to 12 specimens instrumented. The KOH vs. LiOH SCC initiation testing on Alloy 82 utilized one medium-size LWRS test system. This test system was first filled with KOH-based water chemistry. After the completion of the SCC initiation testing in the KOH water chemistry, the system was cleaned following a procedure similar to what is described for on-the-fly water chemistry change during SCC crack growth testing in Section 2.2.2.4. A control study of SCC initiation in the target LiOH-based water chemistry was then performed on the same Alloy 82 material. KOH was used at a concentration that provides the same pH as LiOH (neutral pH at 310°C). Six specimens were tested in each water chemistry. To acquire results within a practical timeframe, the tests were performed with accelerant factors in temperature and dissolved hydrogen level. A higher temperature (360°C) than in service (325°C) was used for these tests. In addition, a dissolved hydrogen concentration was selected that corresponds to an electrochemical corrosion potential at the Ni/NiO stability line, where the SCC initiation susceptibility is believed to be the highest for Ni-base alloys.

A reversing DCPD technique developed by General Electric [3] was adapted for online monitoring of SCC initiation behavior based on original work by KAPL [4]. Details of the PNNL approach were provided in previous publications [5, 6]. In the SCC initiation testing of Alloy 82 to evaluate the KOH vs. LiOH effect, all specimens were tested at or just slightly above their yield stress under constant load. The full load was applied to the specimens within 1–2 days of reaching the test temperature. At the start of a test, the target load (the load at ~0.2% plastic strain) was achieved over 1–2 hours at a constant strain rate of $\sim 1 \times 10^{-5} \text{ s}^{-1}$. This displacement rate allows monitoring of the strain evolution by DCPD with a sufficiently low noise level. For example, in Figure 3, some specimens may yield slightly earlier than others in a multi-specimen load train system due to intrinsic differences in yield strength and/or gauge diameter. In such a case, small amounts of plastic strain up to ~1.5% are allowed in these specimens to achieve a minimum of 0.15% plastic strain in the others. The specimens are then held at an actively controlled constant load until DCPD detects crack initiation. All relevant environmental parameters and DCPD data are monitored and periodically saved to a file. If a test is interrupted for specimen examinations or to remove an initiated specimen, the remaining specimens will be returned to their original load after the test restarts following the same steps described above where stress versus strain response is monitored. Figure 4 shows the evolution of both the non-referenced and the referenced strains throughout the exposure of an Alloy 600 specimen. As mentioned above, by subtracting the reference voltage from the gauge voltage, the contributions of resistivity drift and creep are largely eliminated in the referenced strain response. While cracking and some amount of creep contribute to the observed DCPD response simultaneously, the crack initiation time is determined when an apparent increase occurs in the strain rate above the noise level. This is thought to be the onset of stable crack growth at engineering-relevant rates.

**(a) 6-Specimen
SCC Initiation System**



**(b) 36-Specimen
SCC Initiation System**



Figure 2. The load trains used at PNNL in the (a) medium-size SCC initiation test system with a capacity of testing up to 6 fully instrumented specimens and the (b) large-size SCC initiation test system with a capacity of testing up to 24 instrumented specimens and up to 36 specimens in total.

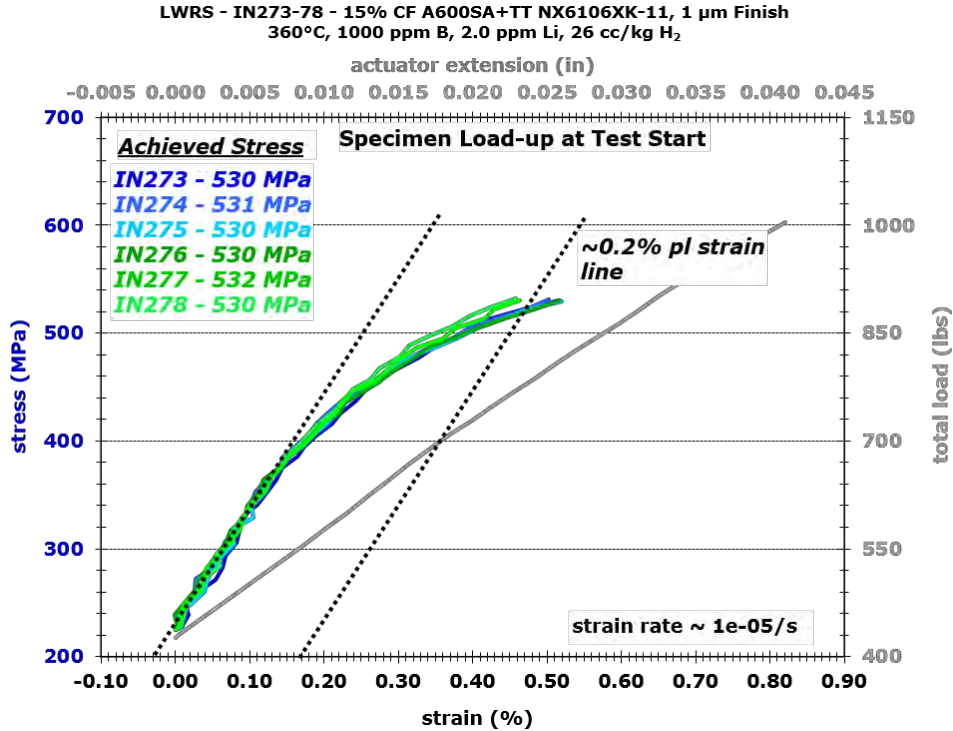


Figure 3. Example of stress versus strain plot during the initial loading of tensile specimens for SCC initiation testing. The displacement in the actuator and the total load is plotted in the secondary x (upper) and y (right) axis, respectively.

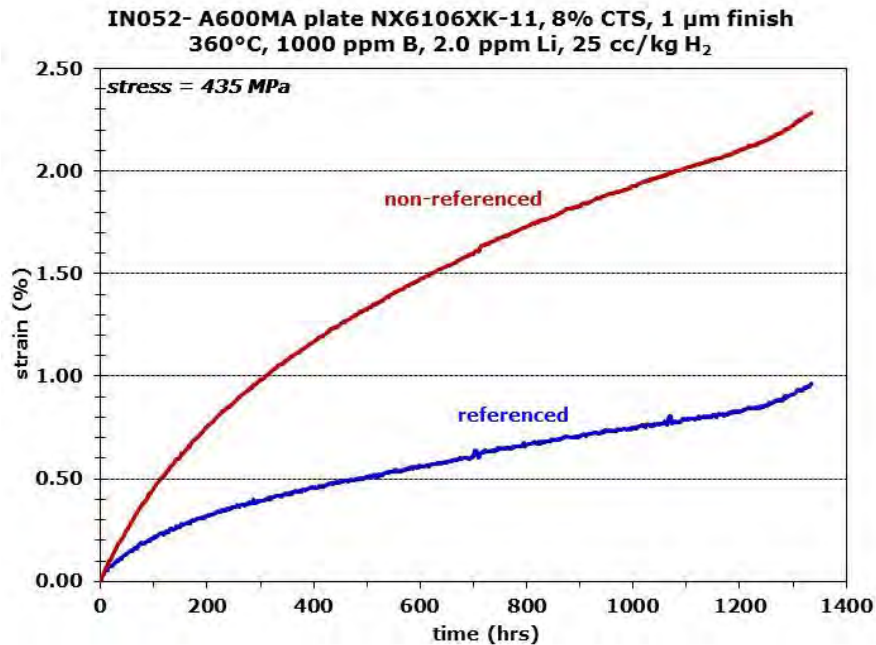


Figure 4. Non-referenced and referenced DCPD strain response for IN052, an 8% CW specimen from Alloy 600MA plate heat NX6106XK-11.

2.2.2 SCC Crack Growth Test Systems and Testing Approach

2.2.2.1 Overview of SCC Crack Growth Test Systems

Although the LWRs SCC initiation test systems can be converted to perform stress corrosion crack growth rate (SCCGR) evaluations, they are fully occupied in FY 2022 and FY 2023 by SCC initiation testing of CW Alloy 690 and Alloy 82. As a result, one U.S. Nuclear Regulatory Commission (NRC) owned SCCGR test system was borrowed under an agreement to investigate the effect of KOH vs. LiOH on the SCC growth behavior of Alloy 82.

The NRC SCCGR test systems at PNNL were designed and constructed to measure crack length under well-defined material and environmental conditions and ensure that the growth rate response is reproducible and characteristic of the test conditions. An example of the SCCGR test system is shown in Figure 5. Detailed information on the development of these test systems can be found elsewhere [7]. However, two key features of these test systems are reviewed here because they are important to the KOH vs. LiOH evaluations.

Firstly, crack length is measured in situ. This has high value because it allows for evaluating SCCGR response before and after "on-the-fly" changes in environmental conditions. For SCCGR testing, it is the best means to ensure that a measurement is not affected by extraneous parameters associated with alternative approaches, such as stopping a test to change water chemistry. On-the-fly evaluations are also time and cost-efficient.

Secondly, control of ion species in the test system recirculating water loop is attained using a mixed bed demineralizer. For simulated standard PWR primary water testing, a controlled amount of boric acid and lithium hydroxide are introduced to the demineralizer. An amount is selected such that stable B and Li values are attained in the test system water, i.e., the demineralizer neither absorbs nor releases B and Li as the water passes through it when no other ions are present. The relevance to the KOH evaluation effort is that this approach to PWR primary water chemistry simulation requires preparing a dedicated demineralizer for each water chemistry to be investigated. It also requires a carefully planned procedure for swapping out water on-the-fly. This approach will be discussed in detail in the next section.



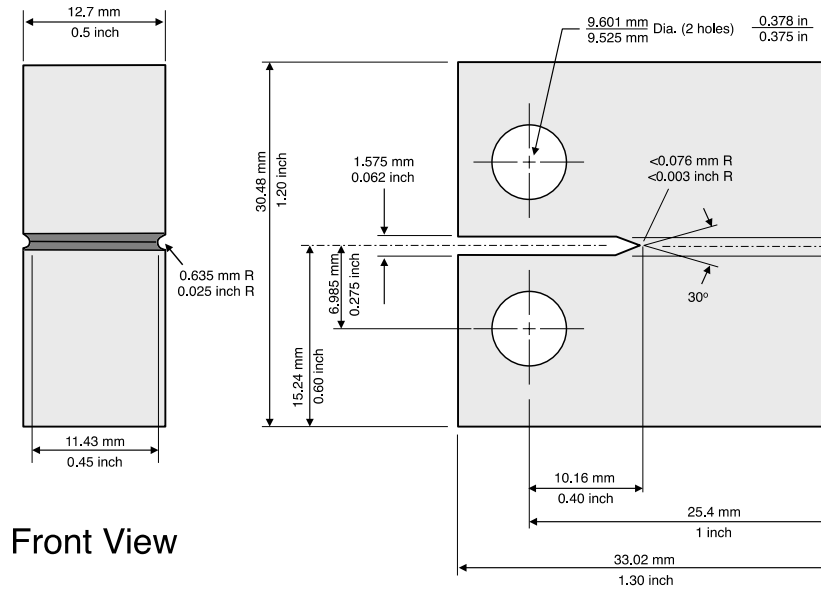
Figure 5. The typical SCCGR test system used at PNNL.

2.2.2.2 General SCC Crack Growth Testing Approach

The PNNL SCCGR test systems have been designed for use with 1T and 0.5T compact tension (CT) specimens, and for this task, side grooved 0.5T CT specimens were used. The details of the specimen geometry are shown in Figure 6. Before loading a specimen in the autoclave, the sample thickness B_{gross} (total thickness) and B_{net} (total thickness subtracting side groove depth), notch depth, and width values were all measured and recorded into the data record for the test. Using the sample dimensions and the YS of the specimen at the test temperature, following American Society for Testing and Materials (ASTM) Standard E-1681, an upper limit on the value of the stress intensity (K) is calculated using the formula:

$$K = \sigma_{\text{ys}} \sqrt{D/1.27} \quad (1)$$

where σ_{ys} is the YS at the test temperature, and D is the smallest among the effective specimen thickness ($B_{\text{eff}} = \sqrt{B_{\text{gross}} \cdot B_{\text{net}}}$), the remaining uncracked specimen width, and the crack length. In the case of materials with large amounts of work hardening (where the ratio of ultimate tensile strength to yield strength is greater than 1.3), such as annealed 300-series stainless steels and low-strength Ni-base alloys, the average of the yield and ultimate stress is used in place of the YS following ASTM guidelines. The tests conducted for this task were within this calculated K limit, but the calculated upper limit on K is not considered a strict value but rather provides a reference point for what may be considered a high-stress intensity for a given material.



Front View

Figure 6. Schematic drawing of a 0.5T CT specimen. Oversized loading holes (~9.5 mm diameter) are used to accommodate ceramic CT inserts that provide electrical isolation between the CT specimen and clevises.

Crack growth tests are usually performed with two specimens loaded in series into a test system, allowing a greater range of material conditions to be examined in a shorter period or assessing test reproducibility by using two samples from the same material condition. After the sample dimensions are measured and spot-weld locations are marked on the sample, it is cleaned and inserted into a test system. Precracking of a sample is done in situ at the test temperature when a single specimen is being tested. Initial precracking of two or more specimens mounted in series in situ is not performed because the time needed to nucleate a precrack is inconsistent which can cause the specimens to have much different precrack lengths. Consequently, precracking two specimens in series likely will lead to specimens having different precrack lengths. The differing precrack lengths would make it impossible to maintain and control the K level in both specimens during and after precracking. Thus, the approach for testing at PNNL is to nucleate a crack individually on each of the two specimens under fatigue in air, followed by continued precracking of the two samples loaded together in situ. Crack transitioning steps are carefully selected to grow the precrack in high-temperature water using the following stages: (1) fatigue, (2) corrosion fatigue, and (3) SCC. Typically, this means producing initial precracks of ~1 mm in air followed by an additional ~1 mm by cycling in situ before transitioning to slow cyclic loading plus hold times to promote SCC. An Instron servohydraulic test frame is used to precrack CT specimens in air, and the same DCPD electronics and system control software used for the crack growth systems is also used for the Instron test frame.

The first step in precracking is to cycle the sample at a relatively high frequency (2–10 Hz) with a large load ratio (R) and K_{\max} less than or equal to the K level chosen for constant K . As the crack begins to grow from the notch, R is increased, and frequency is reduced while the K_{\max} value is increased. By precracking in this way, each precrack segment can grow beyond the plastic zone created by the previous segment. Cyclic loading steps at 0.1 Hz down to 0.001 Hz are performed in high-temperature water for all samples. The final phase involves crack transitioning by very slow cycling with a hold time ranging from 1 h to 24 h. This grows the crack beyond the precracking plastic zone and allows the crack to transition from transgranular (TG) fatigue to the crack growth morphology that normally occurs under constant K conditions. Depending on the material susceptibility, this may be either TG or intergranular (IG) cracking. For materials such as Alloy 82 that readily undergo IGSCC growth in LWR environments, obtaining a

steady SCC growth rate after transitioning to constant K can easily be accomplished by following a standard procedure.

2.2.2.3 **Uncertainties in Crack Growth Data Measurements**

While the noise resolution of the PNNL DCPD test method is no more than $\pm 3 \mu\text{m}$ and allows for establishing trends in the crack growth rate (CGR) down to $\sim 5 \times 10^{-10}$ mm/s, the accuracy of these rates depends on some factors that cannot be fully assessed. For example, crack front irregularity can affect the DCPD-measured CGR. There is no way to document the variation in the shape of the crack front as the crack grew; and therefore, this effect cannot be accurately included in post-test crack length corrections. Another issue is that uniquely identifying each test phase on a crack surface is often impossible after the test has ended. As a result, the post-test correction is typically based on the entire in situ portions of the test. An additional complication is the effect of ligament or contact formation on constant K crack growth. Even though attempts are made to assess these effects during the test, there are no accurate post-test means to assess how well this method works. Crack growth testing experience and interactions with the international expert community have produced many insights into issues, but many uncertainties cannot be effectively quantified. Based on our experience, state-of-the-art testing methods, and data analysis approach, we believe overall uncertainties for CGR measurements are at $\pm 50\%$ for SCC-susceptible materials with steady growth response. Uncertainty in reported stress intensity for a relatively straight final crack front is $\leq 10\%$ after correcting for observed crack length. For a highly uneven final crack, the local variability is not easily quantified and may be substantial.

2.2.2.4 **Water Chemistry Control for the KOH vs. LiOH Study**

This study aims to produce quantitative SCCGR data through in-situ measurement of crack length in KOH-based water chemistries and corresponding reference LiOH-based water chemistries that will serve as the point of comparison. The water chemistries to be evaluated in the SCC growth rate testing were recommended by EPRI, with details listed in Table 1. The effects of KOH relative to LiOH were evaluated in the beginning-of-cycle (BOC) water chemistry and the end-of-cycle (EOC) water chemistry. A mid-cycle water chemistry was also evaluated. This mid-cycle B/K chemistry was evaluated because B-10 decays by thermal neutron absorption during reactor operation to produce Li-7: $^{10}\text{B}(n,\alpha)^7\text{Li}$ [8]. LiOH and KOH concentrations were selected to provide a neutral pH at 310°C. pH at the 360°C test temperature is slightly basic. For these particular bases, this occurs at molar-equivalent concentrations.

Table 1. Nominal PWR primary water chemistries identified by EPRI for the KOH vs. LiOH study.

Environment	ppm B, ppm Li, or ppm K	pH(310°C)	pH(360°C)
BOC	1500 B / 2.2 Li	7.0	8.39
	1500 B / 12.4 K		
EOC	10 B / 0.23 Li	7.0	8.26
	10 B / 1.30 K		
Mid-cycle	1000 B / 3.3 K + 1.0 Li	7.0	8.36

The key to the test is to make on-the-fly changes between Li- and K-containing water chemistries with no change in any other conditions. By following this methodology, a direct comparison of SCCGR of KOH vs. LiOH is obtained with no other changes to the test. The desired test system water and corresponding demineralizer filters were prepared beforehand to achieve this. Mixed bed demineralizer filters were equilibrated to the designated chemistry at room temperature by circulating deaerated water through a loop with the demineralizer and adding the corresponding chemicals until the desired B and Li or K values were attained and stable.

To gain experience and ensure that the on-the-fly water chemistry changes would be successfully implemented during testing, a water chemistry change trial from 1500 ppm B/2.2 ppm Li to 1500 ppm B/12.4 ppm K and then to 10 ppm B/0.23 ppm Li was performed before the start of the actual tests. All the other environmental conditions (e.g., temperature, dissolved hydrogen, etc.) were set to the same target values used in the test. A simplified water board setup in preparation for these changes is illustrated in Figure 7. The on-the-fly changes were accomplished by draining 95 volume% of the old solution inside the water column and then switching the inlet flow to draw water from the prepared new deaerated solution in a five-gallon container. This refills the water column and pushes the new solution through the autoclave and the water board. In addition, the solution being purged from the autoclave was decanted into a disposal container during all autoclave volume exchanges using the outlet before reaching the demineralizer filter (Figure 7). This process is repeated approximately for 5–6 autoclave volume exchanges. The first three exchanges take place with the demineralizer valved out from the water chemistry control board. After the third volume exchange, a demineralizer configured for the new target water chemistry is valved in. Table 2 summarizes the evolution of monitored environmental parameters during the entire process of an on-the-fly water chemistry change trial run from 1500 ppm B/2.2 ppm Li to 1500 ppm B/12.4 ppm K. The changeover usually took ~5 hours to complete, but 24 hours were given for the system to equilibrate. Whether the final concentration of the solution is on par with the target can be determined by acquiring a water sample after the equilibration is reached.

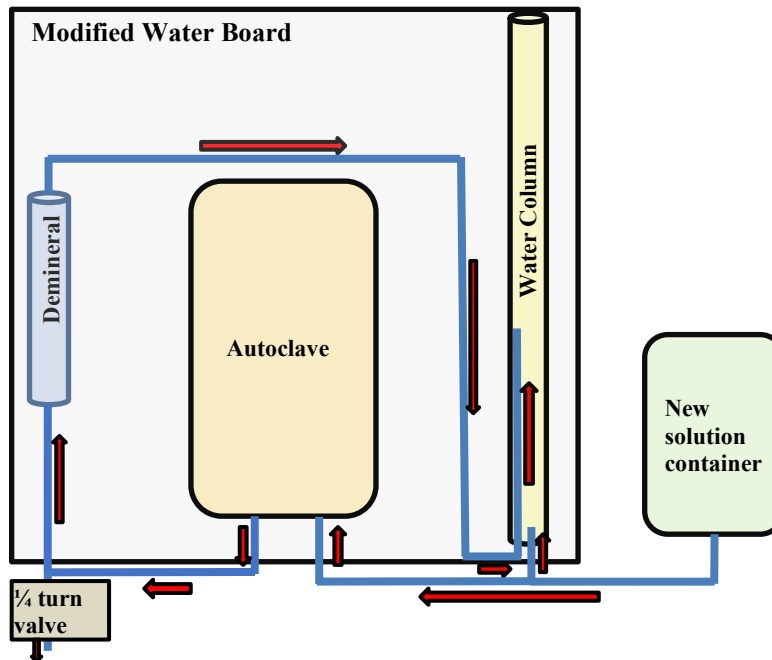


Figure 7. Simplified schematic of the modified water board setup for on-the-fly chemistry changes used in the SCCGR test system. The red arrows indicate the direction of the water flow.

Table 2. Environmental parameter tracking at each autoclave volume exchange during the trial on-the-fly water chemistry changeover from 1500 ppm B/2.2 ppm Li to 1500 ppm B/12.4 ppm K.

Vol. change #	Resistivity (Kohm-cm)	Conductivity (μ S/cm)	pH	Temp ($^{\circ}$ C)	B content (ppm)	Li content (ppm)	K content (ppm)
0	47.32	21.13	6.15	23.45	1512	2.19	0
1	38.78	25.79	N/A	24.89	N/A	N/A	N/A
2	36.62	27.31	N/A	24.97	N/A	N/A	N/A
3	35.17	28.43	N/A	25.00	N/A	N/A	N/A
4	33.90	29.49	N/A	24.94	N/A	N/A	N/A
5	29.83	33.52	6.09	23.55	1637	\sim 0	12.97
6	30.21	33.10	6.18	23.49	1501	\sim 0	12.77

2.2.3 Material and specimen preparation

Alloy 82 is a compatible weld metal for Alloy 600 for automatic gas tungsten arc welding. The Alloy 82H weld (Heat 21719-2) used in this study is an in-house multi-pass build-up by the Naval Nuclear Laboratory (NNL). The composition of this weld compared to the Alloy 82H specification is given in Table 3. As shown in Figure 8, the weld block was received in an “L” shape. It received a post-weld heat treatment (PWHT) at \sim 621 $^{\circ}$ C for 8.5 hours with a heat-up rate of \sim 16.8 $^{\circ}$ C/hour from room temperature to 621 $^{\circ}$ C and a cooling rate of \sim 31 $^{\circ}$ C/hour from 621 to 310 $^{\circ}$ C, followed by air cool.

Table 3. Chemical composition (wt. %) of Alloy 82H Heat 21719-2 in comparison to the Alloy 82H specifications.

Element	A82 Spec	Alloy 82H Heat 21719-2
C	\leq 0.1	0.04
Cr	18–22	20.1
Fe	\leq 3	0.7
Mn	2.5–3.5	2.75
Ni	Bal.	72.8
Ti	\leq 0.75	0.47
Co	\leq 0.1	0.04
P	\leq 0.03	0.01
Cu	\leq 0.5	0.07
S	\leq 0.015	0.002
Si	\leq 0.5	0.07
Nb+Ta	2.0–3.0	2.5 (Ta: 0.069)
Pb		0.002

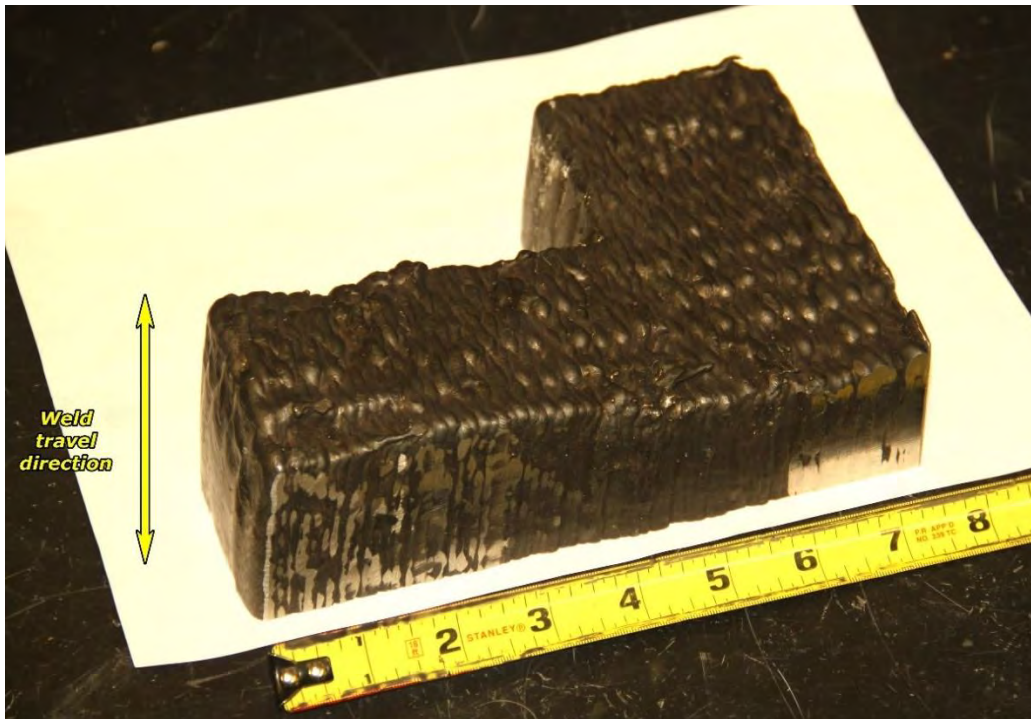


Figure 8. The as-received Alloy 82H (Heat 21719-2) block for this study.

Figure 9 illustrates the cutting plan of the as-received A82 block for this study. A piece was first cut from the bottom of the “L” shaped block and divided into three sub-blocks. The sub-blocks were each cold-forged (CF) to a 30% reduction in thickness along the direction identified in the figure. Although our baseline cold work condition for Alloy 600 and 182 were 15% reduction in thickness, it was decided to first test Alloy 82 in a 30%CF condition because it contains a higher Cr content than Alloy 600 and 182, and literature data has shown that it could be much more resistant to SCC initiation and propagation in high-temperature water. Three CT specimens were machined from the first sub-block, while six initiation specimens were each extracted from the second and third sub-block. Both the CT and the initiation specimens were oriented in the T-S orientation of the weld. Like what we normally do for Alloy 182 weld specimens, all the 30%CF Alloy 82 initiation specimens were polished to a very fine surface finish in the gauge section ending with colloidal silica and then examined in SEM before the initiation testing. Quite unexpectedly, large, irregularly shaped welding defects were found in three specimens, with examples shown in Figure 10. While these specimens were excluded from testing, four specimens went in the first SCC initiation test in BOC LiOH chemistry, and three of them initiated immediately after loading up to 100% yield stress (Figure 11). These data clearly suggest that the 30% CF condition was too aggressive for meaningful evaluation of the SCC initiation behavior of this Alloy 82 material. As a result, another block was sectioned from the top of the “L” shaped block, cold-forged to a 15% reduction in thickness along the same forging direction as the 30%CF block. Fourteen specimens were machined, and their gauge section was again polished to a colloidal silica finish. This time, only two specimens exhibited obvious welding defects on the surface during the pre-test examinations, so the remaining twelve specimens were used for SCC initiation testing, six in the BOC LiOH condition and the other six in the BOC KOH condition.

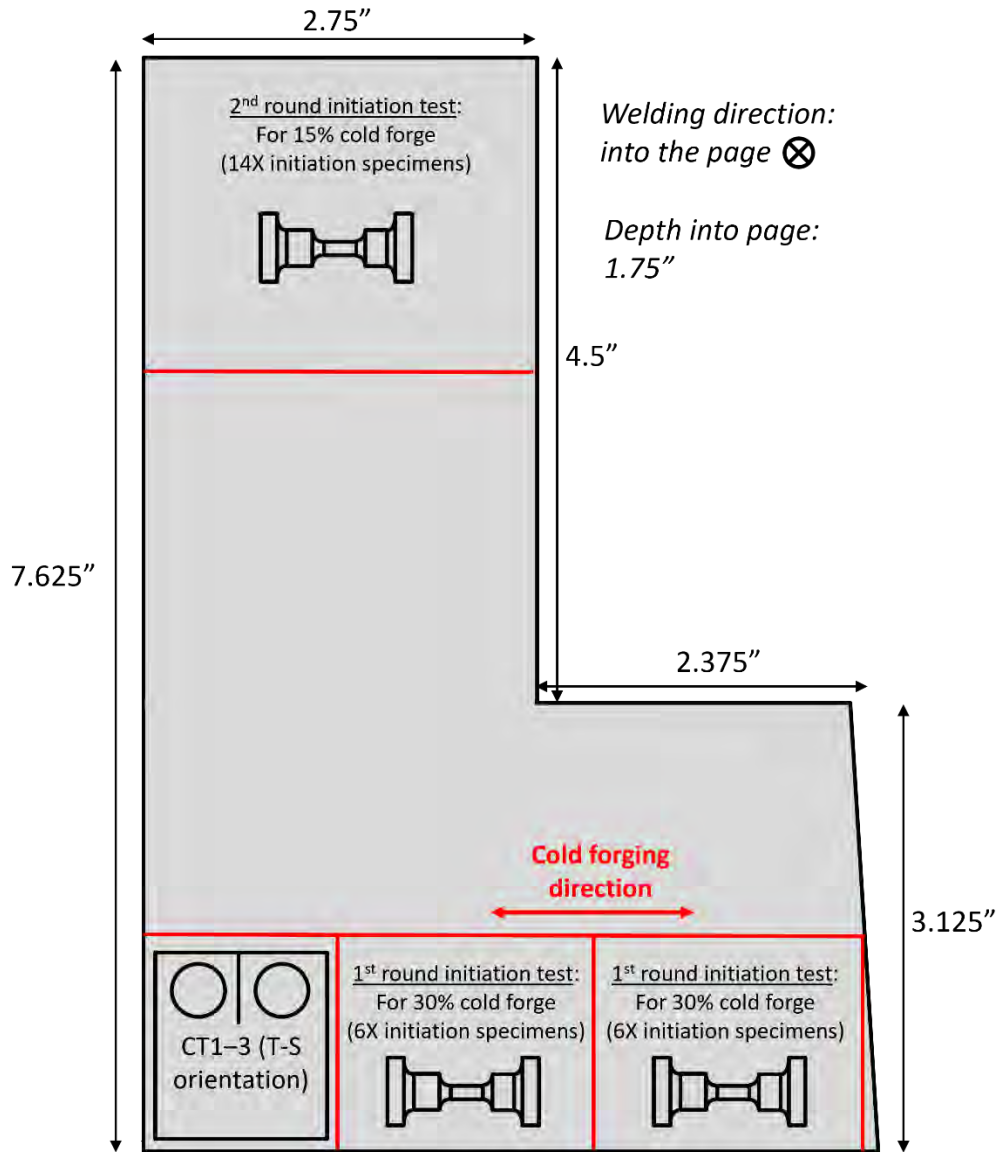


Figure 9. Schematic of the A82 block cutting plan for specimen preparation.

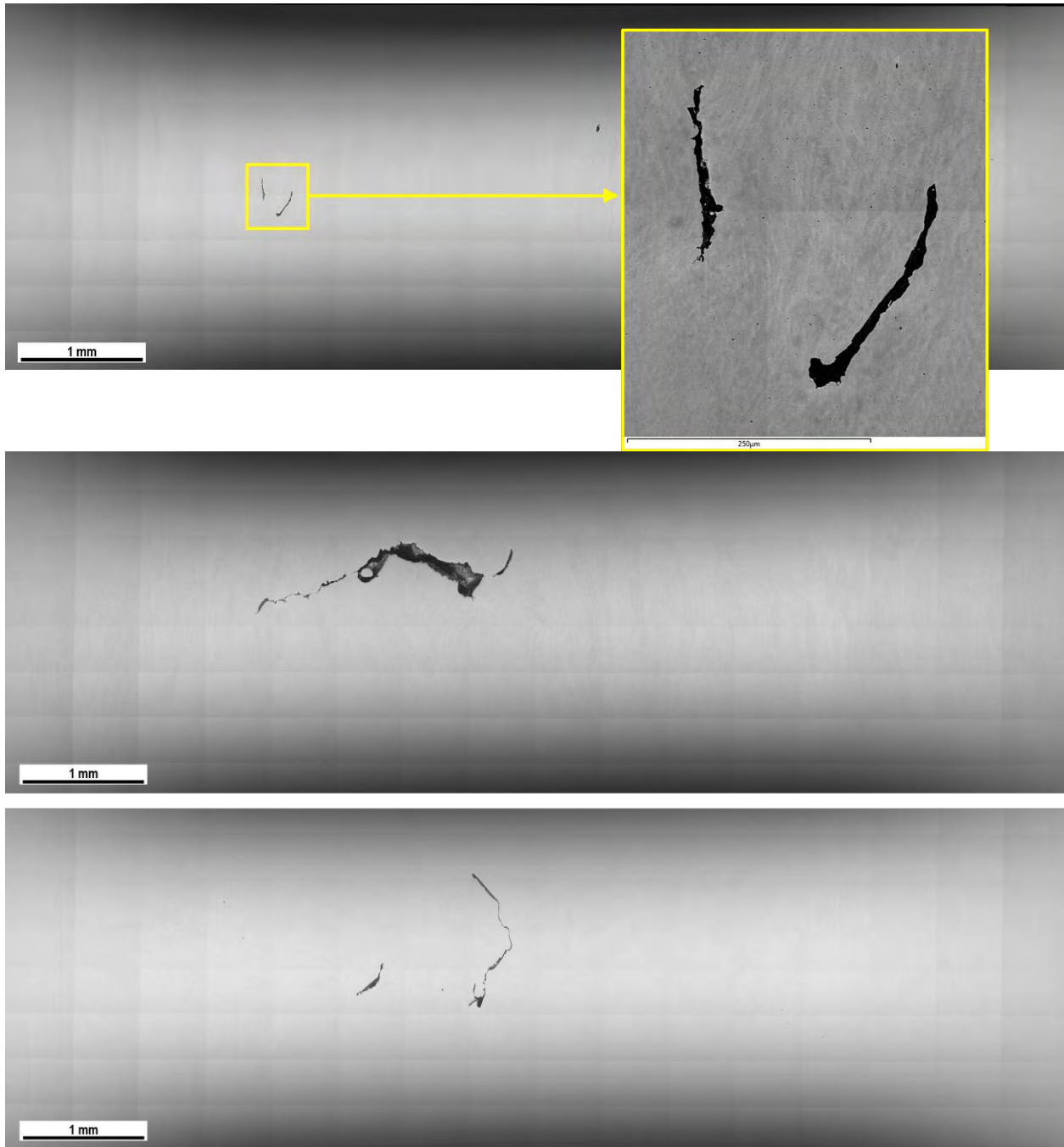


Figure 10. Examples of pre-existing welding defects observed on the gauge surface of several 30% CF Alloy 82 initiation specimens after they were polished to a colloidal silica finish.

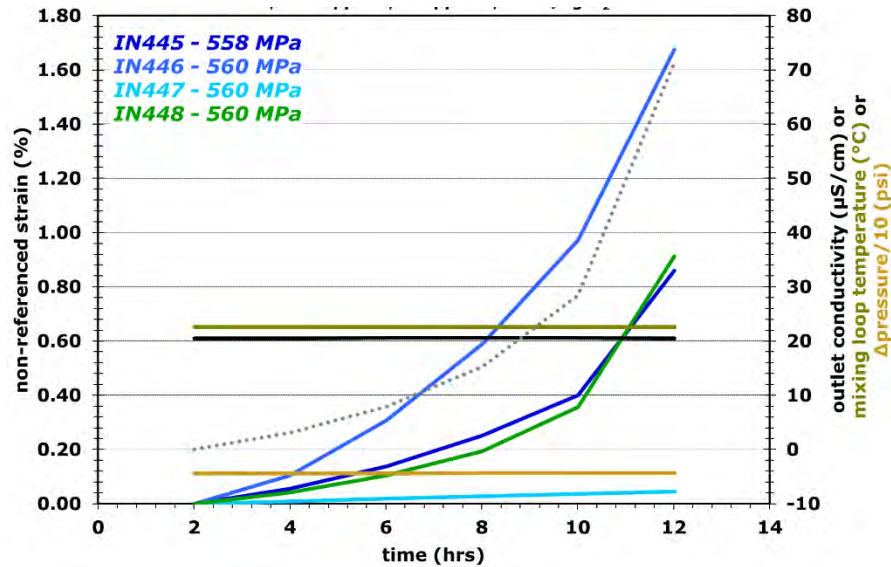


Figure 11. Non-referenced DCPD strain response of the four 30%CF Alloy 82 specimens IN445-48 tested at material yield stress in 360°C PWR primary water containing 1500 ppm B and 2.2 ppm Li.

2.3 SCC Initiation Behavior of Alloy 82 in KOH vs. LiOH-Containing PWR Primary Water

2.3.1 Test Procedure and DCPD Response

As mentioned above, twelve 15% CF Alloy 82 specimens were tested for SCC initiation, six in BOC KOH water chemistry and six in BOC LiOH water chemistry, as specified in Table 1. While the number of specimens is insufficient for any definitive statistical analysis of the initiation behavior, it can provide some insight into the distribution of initiation times. The tests were performed in 360°C water with a dissolved hydrogen content of 26 cc/kg to maintain an electrochemical corrosion potential at the Ni/NiO stability line, where the SCC initiation susceptibility is believed to be the highest for Ni-base alloys.

The target test stress is the 0.2% offset YS for all specimens. As described in Section 2.2.1, PNNL tracks the stress versus strain response of all these specimens during the specimen loading process, often with a resolution of 0.01% plastic strain, allowing us to measure the plastic strain of each specimen precisely. The loading of these specimens began within 1–2 days after the systems reached the target test temperature and water chemistry, and the target load was achieved over 1–2 hours at a constant strain rate of $\sim 1 \times 10^{-5} \text{ s}^{-1}$. The initial loading run in the two sets of specimens is presented in Figure 12 for the reference BOC KOH water chemistry and Figure 13 for the BOC LiOH water chemistry, respectively. Due to intrinsic differences in microstructure and/or gauge diameters, there is always some variability in the attained plastic strain among the specimens. PNNL attempts to ensure that most specimens reach 0.2% plastic strain and tries not to allow any specimen to have less than 0.15% plastic strain. Due to the elongated dendritic microstructure and the potential presence of welding defects, weld specimens have often shown a larger scatter in plastic strain during the load-up process. These Alloy 82 specimens were no exception, but the plastic strain range attained in the specimens for the two different water chemistries was similar. Both tests showed a maximum plastic strain of $\sim 0.8\%$ and a minimum plastic strain of $\sim 0.12\%$ among the six specimens. During the constant load observation period, both tests were interrupted a few times to remove initiated specimens. The remaining specimens were then reloaded to their original load following the same procedure. Additional plastic strain was sometimes incurred during reloading the specimens (this is commonly observed for many materials that PNNL has tested for SCC initiation) and was recorded to calculate the total plastic strain for each specimen upon completion of the

test. The data is shown in Table 4 together with other test status information, including the SCC initiation time of all specimens.

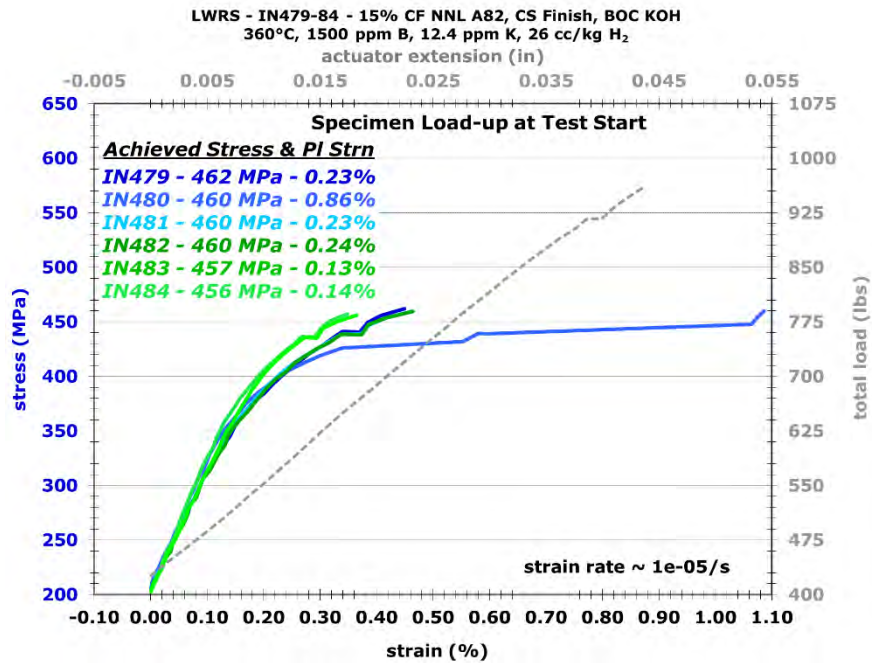


Figure 12. The stress vs. strain plot during the initial loading of the six 15%CF Alloy 82 specimens IN479-84 in 360°C PWR primary water containing 1500 ppm B and 12.4 ppm K.

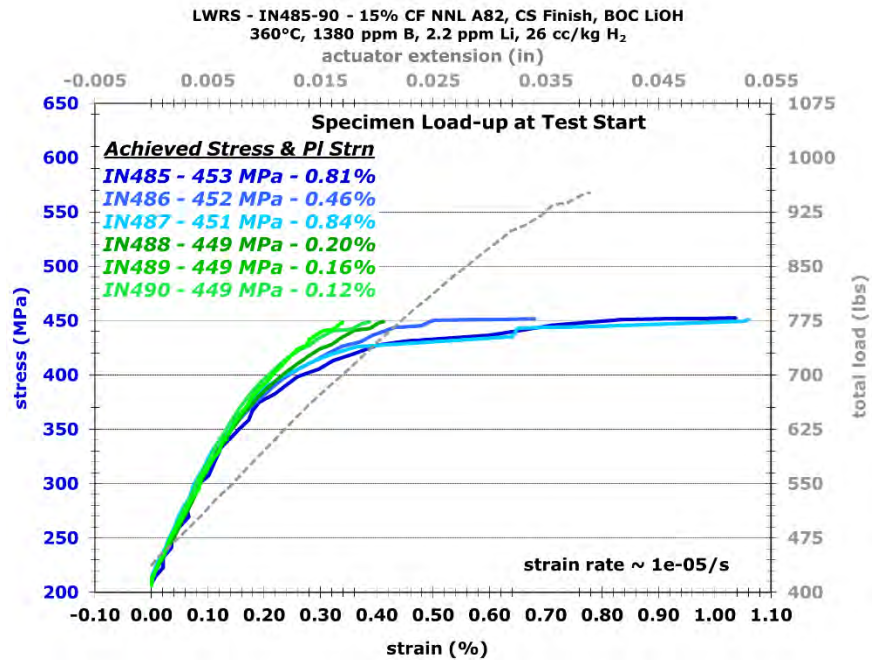


Figure 13. The stress vs. strain plot during the initial loading of the six 15%CF Alloy 82 specimens IN485-90 in 360°C PWR primary water containing 1500 ppm B and 2.2 ppm Li.

Table 4. Summary of the SCC initiation test status of the 15%CF Alloy 82 specimens.

Spec. ID	ppm B, ppm Li, or ppm K	Finish	Temp (°C)	Applied Stress (MPa)	Total accumulated plastic strain (%)	Time to SCC initiation (h)
IN485	1500 B/2.2 Li	1 μm	360	465	0.81	16
IN486	1500 B/2.2 Li	1 μm	360	452	0.46	100
IN487	1500 B/2.2 Li	1 μm	360	451	0.84	33
IN488	1500 B/2.2 Li	1 μm	360	449	0.20	374
IN489	1500 B/2.2 Li	1 μm	360	449	0.16	125
IN490	1500 B/2.2 Li	1 μm	360	449	0.12	NI (2152)*
IN479	1500 B/12.4 K	1 μm	360	462	0.23	667
IN480	1500 B/12.4 K	1 μm	360	460	0.86	40
IN481	1500 B/12.4 K	1 μm	360	460	0.23	704
IN482	1500 B/12.4 K	1 μm	360	460	0.23	523
IN483	1500 B/12.4 K	1 μm	360	457	0.13	135
IN484	1500 B/12.4 K	1 μm	360	456	0.13	662

*NI = no initiation. The time in the parenthesis indicates the total exposure time of the specimen when the test ended.

An overview of the non-referenced DCPD strain response for the six specimens tested in the KOH and LiOH BOC water chemistries is presented in Figures 14 and 15, respectively. SCC initiation is considered to occur when an obvious increase in strain rate occurs in the DCPD strain response, as noted in the figure legends. For the six specimens tested in the KOH BOC water chemistry, two specimens initiated relatively early, within 150 hours, while the other four initiated between 500 and 700 hours. In comparison, four specimens tested in the LiOH BOC water chemistry initiated within 150 hours, one at 374 hours, but the last one did not exhibit any indication of SCC initiation up to the point the test ended at 2152 hours. The SCC initiation times acquired from both test systems were also plotted as a function of total plastic strain and applied stress, as shown in Figures 16 and 17, respectively. The results suggested that higher plastic strain had contributed to faster initiation in both water chemistries (Figure 16), but no systematic trend was found between SCC initiation and applied stress (Figure 17).

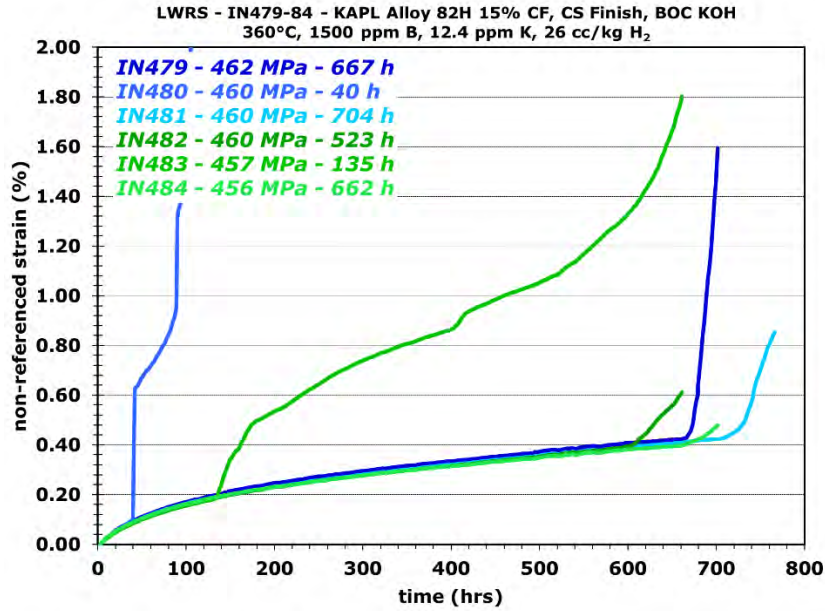


Figure 14. Overall non-referenced DCPD strain response of the six 15%CF Alloy 82 specimens IN479-84 tested at material yield stress in 360°C PWR primary water containing 1500 ppm B and 12.4 ppm K. The SCC initiation time of each specimen is marked in the legend.

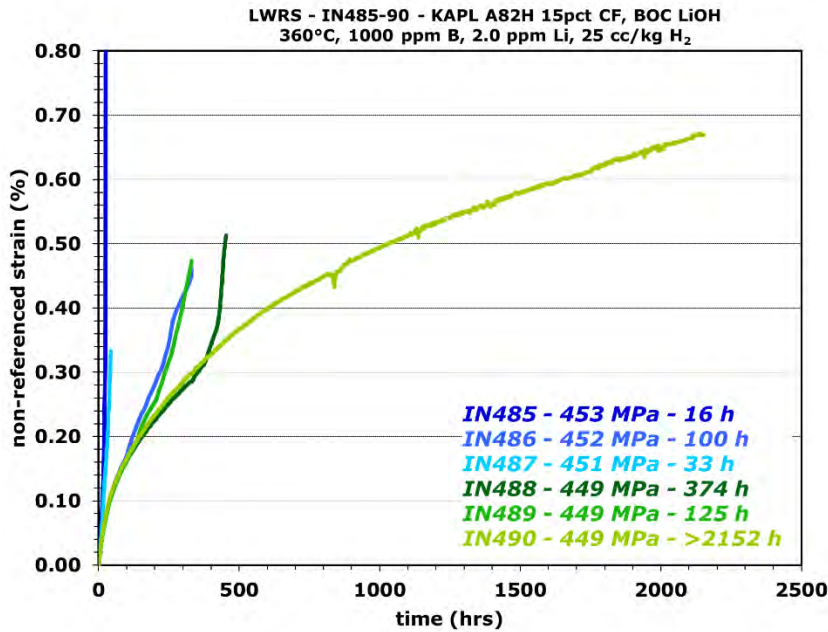


Figure 15. Overall non-referenced DCPD strain response of the six 15%CF Alloy 82 specimens IN479-84 tested at material yield stress in 360°C PWR primary water containing 1500 ppm B and 2.2 ppm Li. The SCC initiation time of each specimen is marked in the legend.

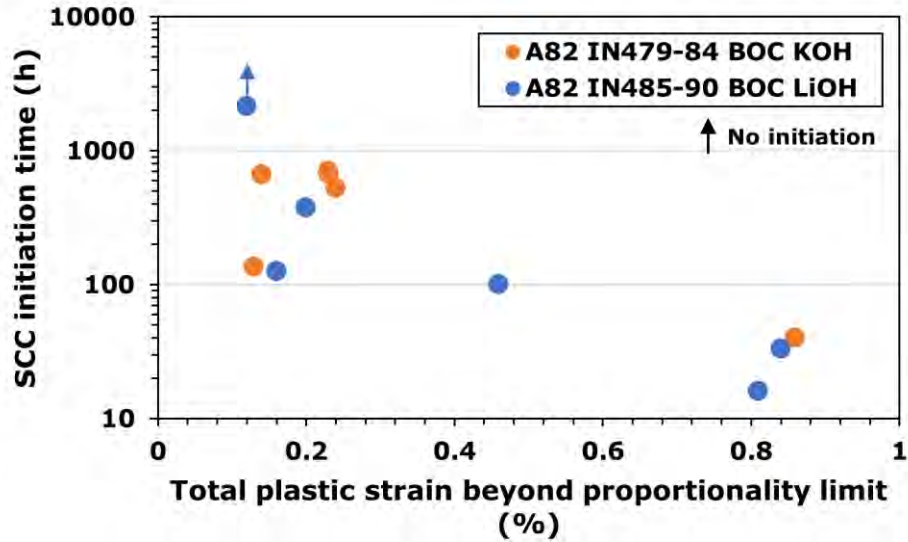


Figure 16. SCC initiation time of all the tested 15%CF Alloy 82 specimens as a function of total plastic strain accumulated during every loading run.

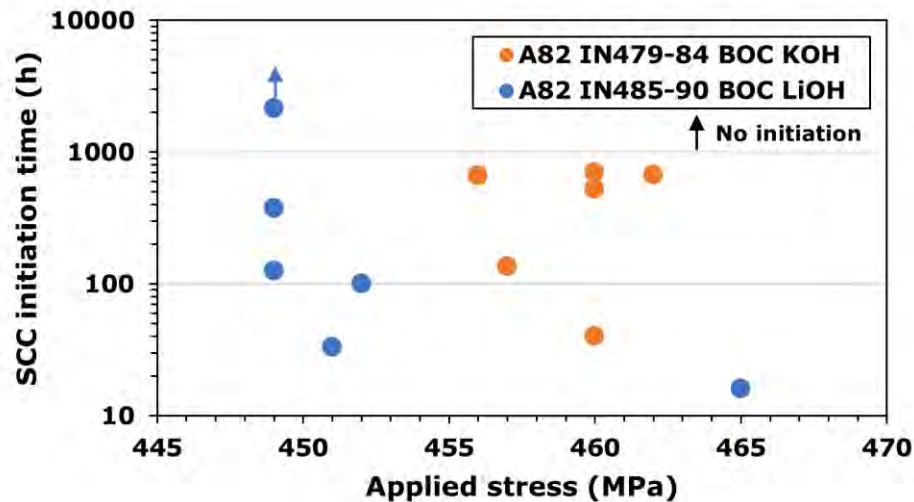


Figure 17. SCC initiation time of all the tested 15%CF Alloy 82 specimens as a function of applied stress.

2.3.2 Post-Test Cracking Morphology

The main goal of the post-test scanning electron microscopy (SEM) characterization on the initiated specimens is to examine whether any obvious difference is present in the initiation morphology of the specimens tested in the KOH vs. LiOH BOC water chemistries. When specifically studying SCC initiation crack morphology, PNNL stops a test immediately after SCC initiation is detected in a specimen to allow examination of the crack morphology at the time of initiation. However, because the primary goal of this KOH vs. LiOH SCC initiation study is to measure SCC initiation time, the tests were only interrupted when a specimen was nearing failure. This allows for the chance of having multiple specimens initiate before a test interruption is needed, reducing the number of test interruptions and making more effective use of time and project funds. In the following sections, the SCC initiation morphology of the specimens tested in the LiOH and the KOH BOC water chemistries will be presented and compared in detail.

2.3.2.1 SCC Initiation Morphology in the BOC KOH Water Chemistry

The post-test surface morphology of the six Alloy 82 specimens IN479-84 tested in the BOC KOH water chemistry are presented in Figures 18–23. The specimens are reported in order of increasing SCC initiation time. The loading direction was parallel to the axial direction of the specimens (i.e., left-to-right in the figures). For each specimen, obvious cracks are highlighted in red in the montage image. The primary crack(s) considered responsible for DCPD detection of SCC initiation are also shown at higher magnifications in the same figure. Variations in cracking morphology were observed for these specimens. Some specimens exhibited a single large crack with very few small cracks (IN481 and IN482), while some showed one or two primary cracks with a higher density of small cracks (IN479, 480, 483, and 484). No systematic relationship was found between the degree of cracking and the time elapsed between DCPD-detected SCC initiation and specimen removal. One piece of supporting evidence is that while SCC initiation was detected by DCPD in IN484 and IN479 almost simultaneously and were removed after the same total exposure in the test (701 hours), they featured distinctively different cracking morphology on the gauge section. IN479 exhibited two wide-opened large cracks of more than 1 mm long in the gauge (Figure 22), suggesting significantly accelerated cracking upon macroscopic SCC initiation. Meanwhile, the cracks were much tighter and shorter in IN484 (Figure 21). Indication was also captured by DCPD strain response, where a much higher increase in strain rate was observed in IN479 than in IN484 after detection of SCC initiation (Figure 14). Table 4 shows that IN479 was loaded to a higher plastic strain than IN484 (0.23% vs. 0.13%) and reached slightly higher stress (462 vs. 456 MPa). However, the higher stress and strain state alone does not seem sufficient to explain the observed difference in cracking morphology. For example, IN481 and 482 were also loaded to the same total plastic strain and stress as IN479. Despite undergoing longer exposure times between DCPD-detected crack initiation and specimen removal than IN479, they exhibited a much lesser extent of cracking (Figures 20 and 23). In such cases, variation in SCC susceptibility due to local chemistry and grain orientation may have also come into play, but their effects are difficult to deconvolute without further investigation. In addition, welding defects, if present inside the specimens, could accelerate crack growth.

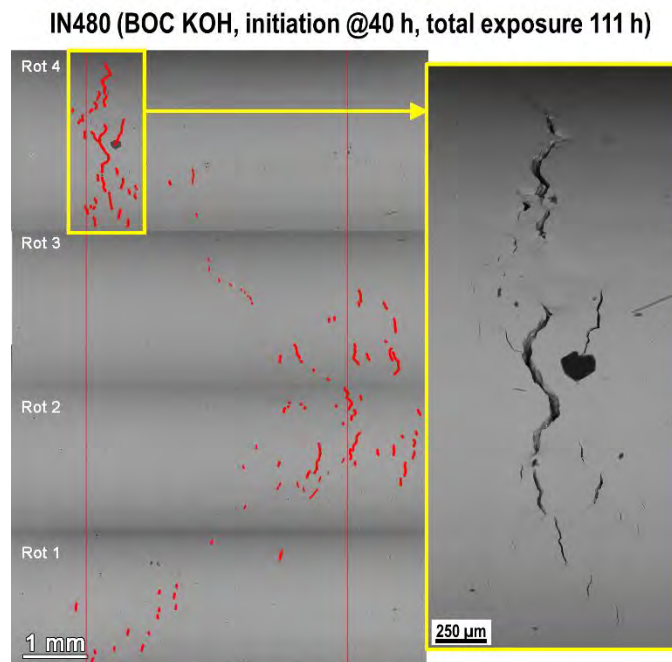


Figure 18. Post-test SEM-BSE montage of the first initiated 15%CF Alloy 82 specimen IN480 in 360°C PWR primary water with 1500 ppm B and 12.4 ppm K.

IN483 (BOC KOH, initiation @135 h, total exposure 661 h)

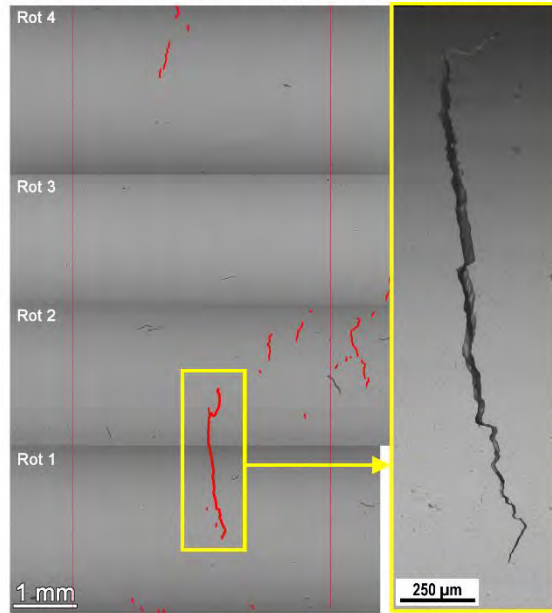


Figure 19. Post-test SEM-BSE montage of the second initiated 15%CF Alloy 82 specimen IN483 in 360°C PWR primary water with 1500 ppm B and 12.4 ppm K.

IN482 (BOC KOH, initiation @523 h, total exposure 661 h)

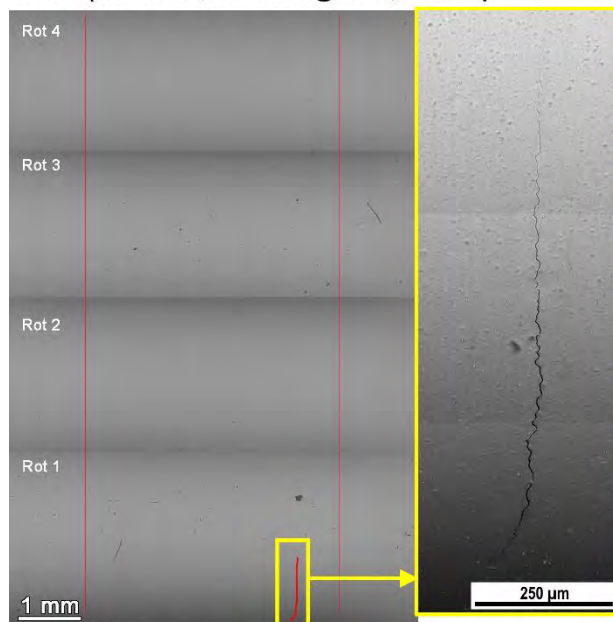


Figure 20. Post-test SEM-BSE montage of the third initiated 15%CF Alloy 82 specimen IN482 in 360°C PWR primary water with 1500 ppm B and 12.4 ppm K.

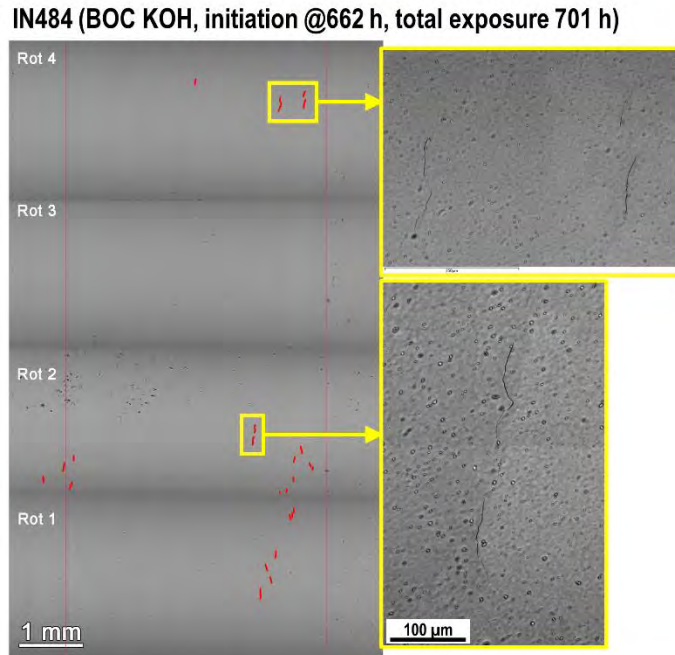


Figure 21. Post-test SEM-BSE montage of the fourth initiated 15%CF Alloy 82 specimen IN484 in 360°C PWR primary water with 1500 ppm B and 12.4 ppm K.

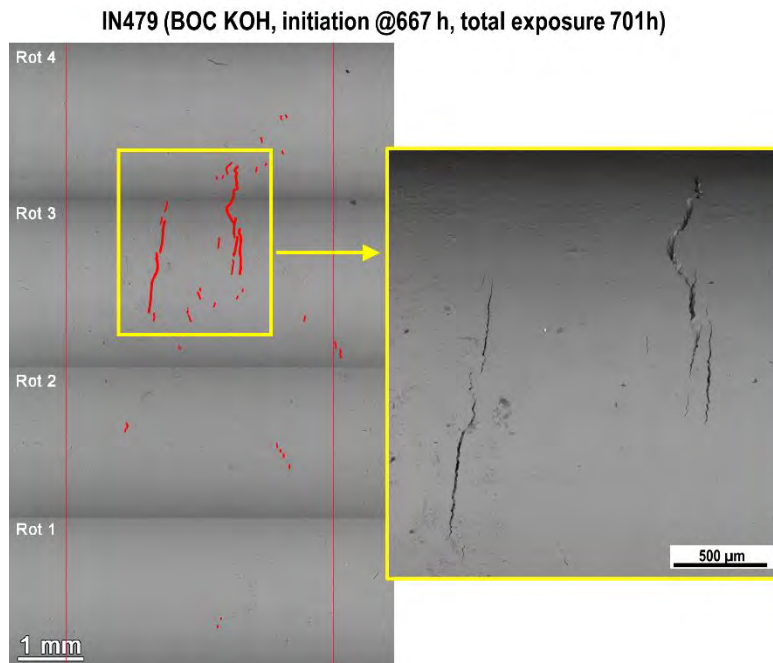


Figure 22. Post-test SEM-BSE montage of the fifth initiated 15%CF Alloy 82 specimen IN479 in 360°C PWR primary water with 1500 ppm B and 12.4 ppm K.

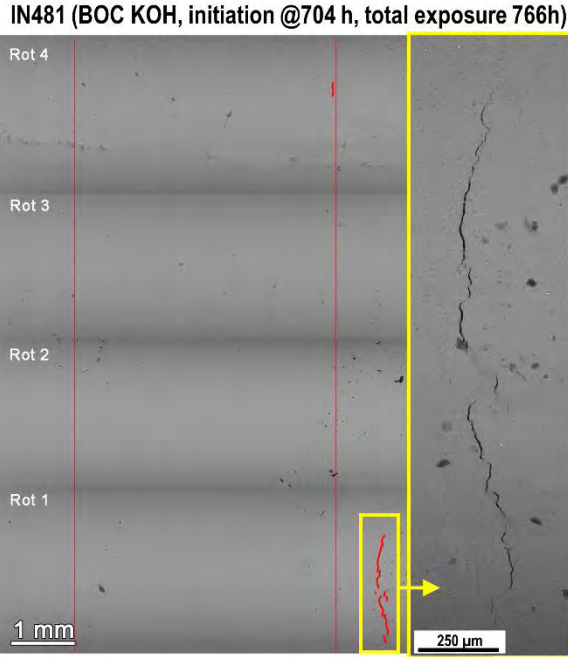


Figure 23. Post-test SEM-BSE montage of the six initiated 15%CF Alloy 82 specimen IN481 in 360°C PWR primary water with 1500 ppm B and 12.4 ppm K.

2.3.2.2 SCC Initiation Morphology in the BOC LiOH Water Chemistry

The post-test surface morphology of the six initiated Alloy 82 specimens IN485–90 tested in the BOC water chemistry containing 1500 ppm B and 2.2 ppm Li are presented in Figures 24–29. These specimens are also reported in order of increasing SCC initiation time, and the loading direction was parallel to the axial direction of the specimens. As shown in Table 4, four out of the six specimens initiated within 150 hours of exposure. IN485 and IN487 reached >0.8% plastic strain during loading and were the first two to show macroscopic SCC initiation after only two to three days in test. They were removed within a half day to one day after DCPD detected SCC initiation, and both showed wide-opened primary cracks close to 1 mm long (Figures 24 and 25). A higher density of cracks was observed in IN486 (Figure 26) and IN489 (Figure 27), which initiated between 100 and 132 hours but stayed in test for another ~200 hours before removal. IN488 initiated at 374 hours and generally showed similar cracking morphology as IN486 and IN489 (Figure 28). Interestingly, the last specimen IN490 underwent 5–50X longer exposure time than the first five specimens but not a single crack was observed on its gauge surface after the test ended. A thicker layer of spinel oxide was formed on the fillet region because of the longer exposure and rougher surface finish (Figure 29).

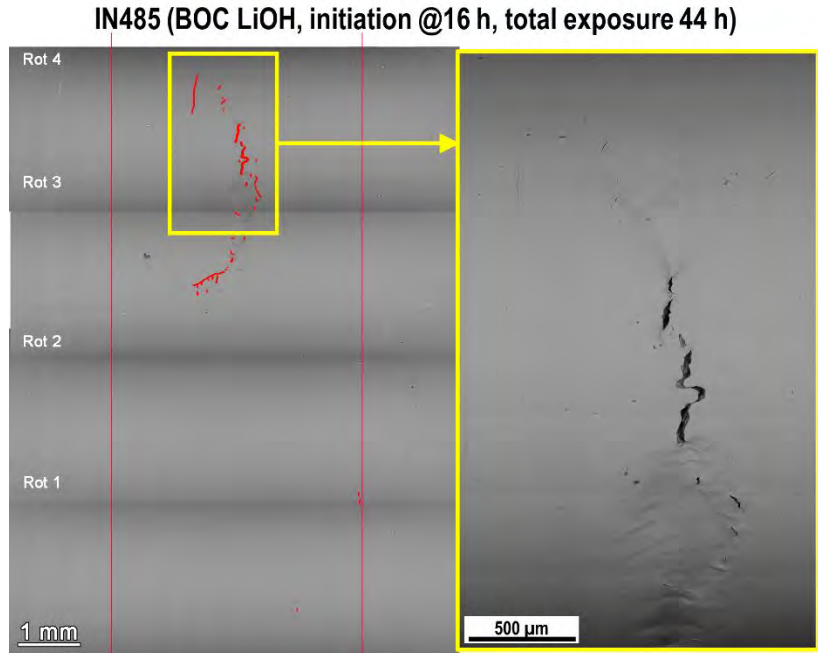


Figure 24. Post-test SEM-BSE montage of the first initiated 15%CF Alloy 82 specimen IN485 in 360°C PWR primary water with 1500 ppm B and 2.2 ppm Li.

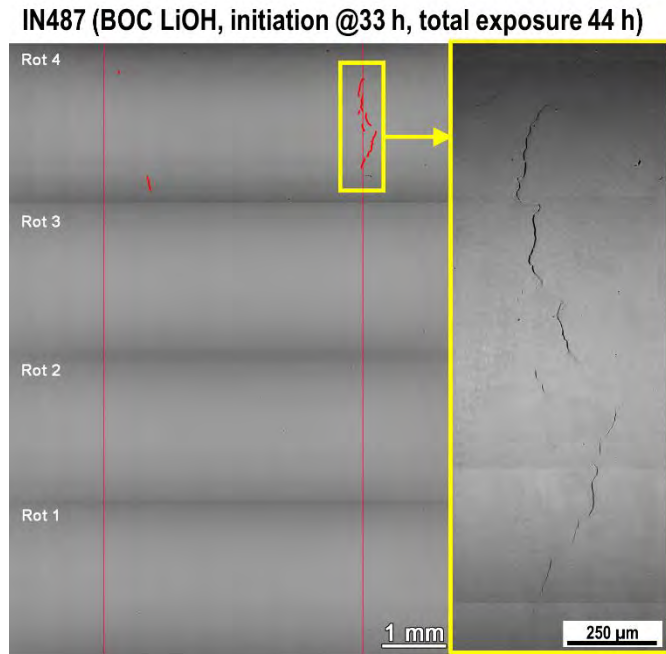


Figure 25. Post-test SEM-BSE montage of the second initiated 15%CF Alloy 82 specimen IN487 in 360°C PWR primary water with 1500 ppm B and 2.2 ppm Li.

IN486 (BOC LiOH, initiation @100 h, total exposure 332 h)

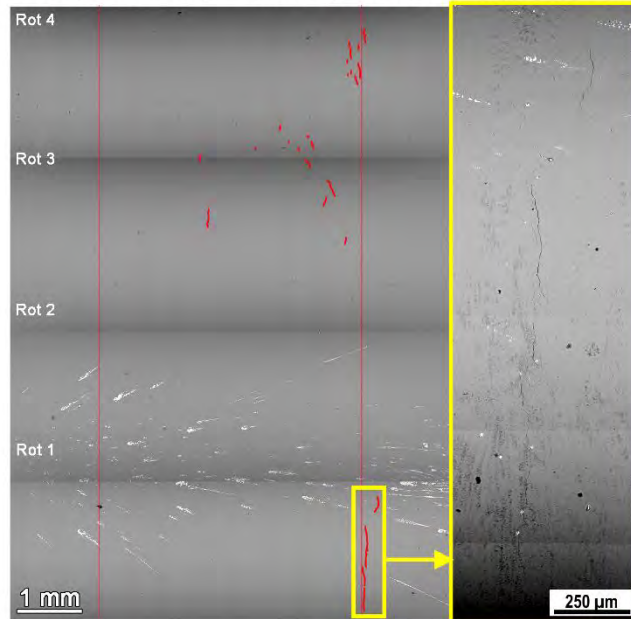


Figure 26. Post-test SEM-BSE montage of the third initiated 15%CF Alloy 82 specimen IN486 in 360°C PWR primary water with 1500 ppm B and 2.2 ppm Li.

IN489 (BOC LiOH, initiation @125 h, total exposure 332 h)

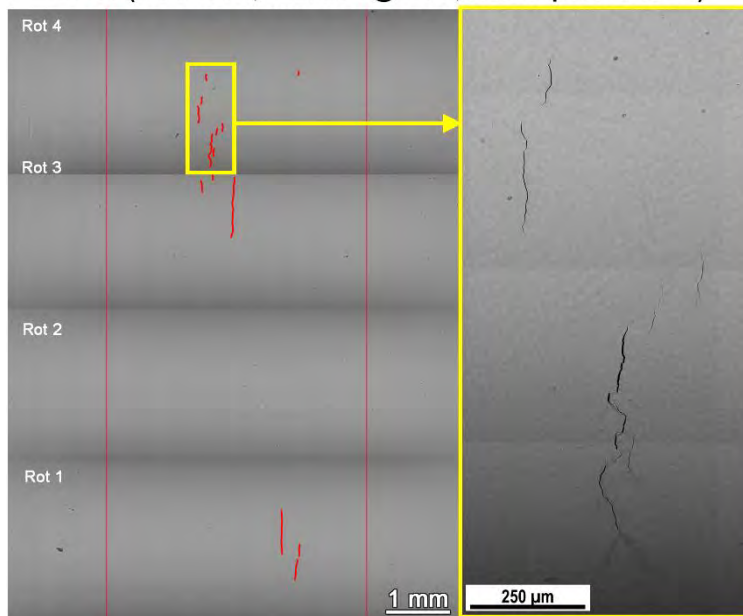


Figure 27. Post-test SEM-BSE montage of the fourth initiated 15%CF Alloy 82 specimen IN489 in 360°C PWR primary water with 1500 ppm B and 2.2 ppm Li.

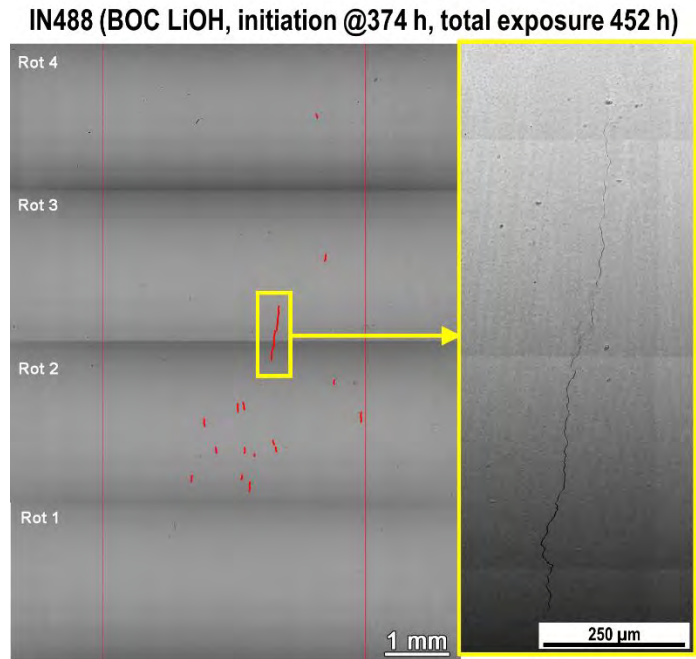


Figure 28. Post-test SEM-BSE montage of the fifth initiated 15%CF Alloy 82 specimen IN488 in 360°C PWR primary water with 1500 ppm B and 2.2 ppm Li.

IN490 (BOC LiOH, no initiation, total exposure 2152 h)



Figure 29. Post-test SEM-BSE montage of the non-initiated 15%CF Alloy 82 specimen IN490 in 360°C PWR primary water with 1500 ppm B and 2.2 ppm Li.

2.4 SCC Crack Growth Behavior of Alloy 82 in KOH vs. LiOH-Containing PWR Primary Water

Two 30%CF Alloy 82 specimens, CT228 and CT229, were machined in the T-S orientation from the weld block provided by NNL (Figure 9). They were fatigue precracked individually in air at room temperature following the procedure described in Section 2.2.2.2. The side grooves of these two specimens were polished to a 1 μm finish, allowing the precrack to be viewed and its length to be measured. Optical micrographs of the side grooves of CT228 and CT229 showing the precracks produced by air fatigue are presented in Figures 30 and 31, respectively. The target precrack length was set at 1.1 mm, and this value was achieved reasonably well in both specimens. Since the crack length measured on both sides of CT228 is slightly longer than in CT229, it was decided to use CT228 as the controlling sample and CT229 as the companion sample in the SCC growth rate test, meaning that the load control during the test is implemented based on the response of CT228. This helps to guard against the possibility of inaccurate DCPD crack length data causing stress intensity to deviate substantially from the target value.

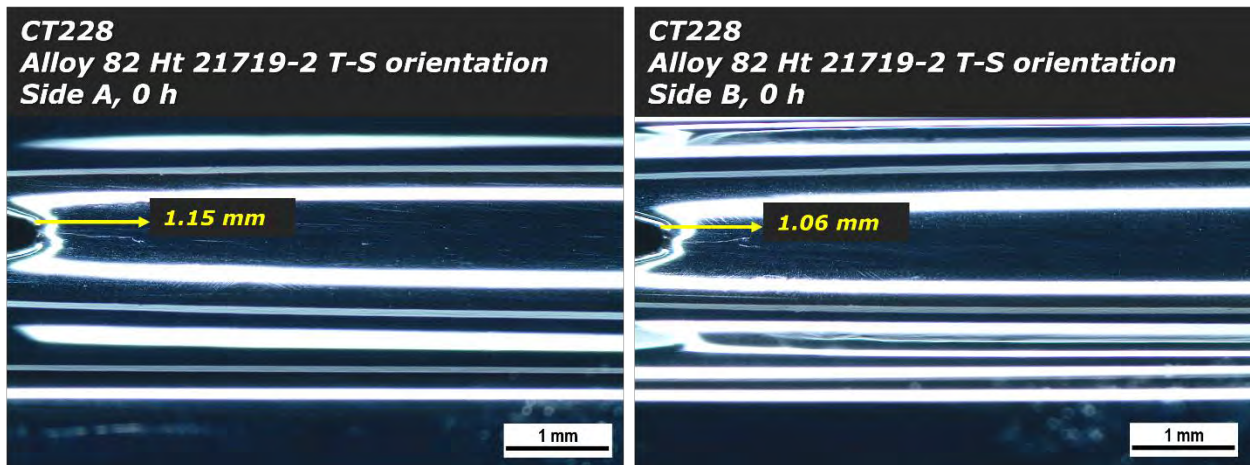


Figure 30. Optical micrographs of the polished side grooves of the 30%CF Alloy 82 specimen CT228. The length of the precrack produced by air fatigue is marked in both side grooves.

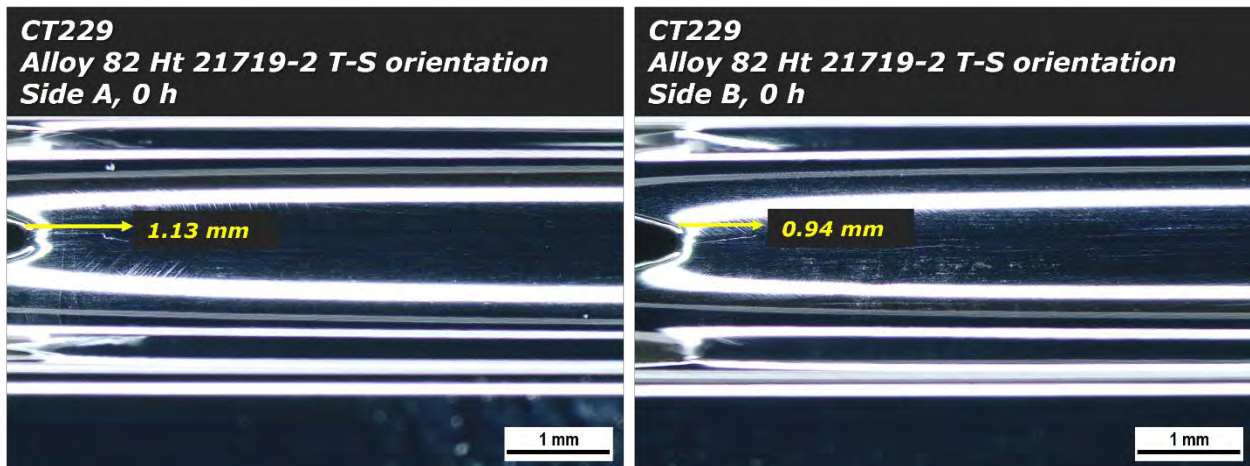


Figure 31. Optical micrographs of the polished side grooves of the 30%CF Alloy 82 specimen CT229. The length of the precrack produced by air fatigue is marked in both side grooves.

2.4.1 In-Situ Crack Growth Rate Response

A test overview of the referenced DCPD crack growth response of CT228 and CT229 is provided in Figure 32. The test was completed in June 2023 with the SCCGR of one or both specimens evaluated in all three water chemistries specified in Table 1 through on-the-fly changes. Not unexpectedly, the unique microstructure of weld metal posed some challenges in obtaining measurable SCC growth in the specimens. As a result, extra time was taken to ensure the SCCGR data obtained was reliable as possible, which will be explained in more detail below. It should be noted that the SCCGRs mentioned in this section are not corrected. As will be shown later in Section 2.4.2, the DCPD estimated total crack length was very close to the actual crack length observed post-test. Therefore, no post-test SCCGR correction was needed.

The two specimens were loaded in series into an NRC SCC test system, and the test was started in the BOC PWR primary water condition containing 1500 ppm B and 2.2 ppm Li at 360 °C and 25 cc/kg H₂. Figure 33 presents the initial aggressive cycling in high-temperature water to further extend the precrack produced by air fatigue. A series of loading conditions were used to transition from the TG precrack to an IGSCC crack front that is typically much more susceptible to SCC growth in Ni-base alloys. Loading conditions started with cyclic loading with decreasing frequency from 1.0 to 0.01 Hz at a load ratio of 0.5 and a peak stress intensity at 30 MPa√m, followed by a final cycling step of a 980 s rise and a 20 s fall (0.001 Hz) with R = 0.5 in a sawtooth form. The two specimens exhibited consistent crack growth behavior during these loading steps, and the CGR continued to drop as the cyclic loading conditions became more and more gentle. As a result, the test proceeded to constant stress intensity (*K*) evaluation at 223 hours at 30 MPa√m. Since weld metals are known to exhibit variability in crack growth behavior due to their unique dendritic microstructure, the crack growth in each water chemistry was monitored for at least 500 hours to establish a reliable trend for SCCGR estimation. As can be seen in Figure 34, despite local fluctuations in SCCGR, especially in CT228, the SCCGR was relatively stable in both specimens during the entire BOC water chemistry evaluation period, including before and after the on-the-fly water chemistry change from LiOH to KOH and back to LiOH, measuring an average SCCGR of 1.0×10^{-8} mm/s for CT228 and 1.5×10^{-8} mm/s for CT229. The test then moved on to evaluate the EOC LiOH water chemistry beginning at ~3350 hours (Figure 35). Some fluctuations in SCCGR occurred in both specimens (with a higher magnitude in CT229 than in CT228) before the water chemistry stabilized at 3623 hours. The SCCGR then gradually increased in CT228 from 6.5×10^{-9} mm/s to 1.1×10^{-8} mm/s during the subsequent ~700 hours of exposure, while the SCCGR in CT229 decreased from 5.4×10^{-9} mm/s to 1.7×10^{-9} mm/s. A few possibilities could explain this slowdown in SCCGR. The crack tip could have reached a region with low SCC susceptibility (either due to orientation or microchemistry), or the crack began lagging along some portions of the crack front, or ligaments may have been left in the wake of the crack. Ni-base weld metals are known for their tendency to form “fingered” growth during SCC growth testing of CT specimens, where IGSCC tends to favor the solidification grain boundaries (SGB) between certain elongated but narrow packets of columnar grains. Although the SCCGR at the crack tips in these local packet regions could be high, the large uncracked ligament between the IG packets can prevent a clear detection of the local SCCGR. Since any SCCGR values below 3×10^{-9} mm/s (i.e., ~60 μm per year) are considered too low for meaningful assessments of crack growth behavior, we decided to go back to fatigue cycling in water to grow the crack for another ~500 μm in the hope to bring the crack tip to a more SCC-susceptible region and straighten the crack from any uncracked ligaments that had already formed. This procedure is shown in Figure 36, where the R ratio was reduced from 0.5 to 0.3 to promote fatigue crack growth. The test returned to constant *K* at 4754 hours after ~600 and 400 μm growth was estimated by DCPD in CT228 and CT229, respectively. Unfortunately, although an elevated SCCGR was measured for CT228, no improvement was observed in CT229 (Figure 37). To alleviate the lack-of-growth situation in CT229, we implemented another round of sequential fatigue cycling with details provided in Figure 38. It turned out that the aggressive loading was ineffective in advancing the crack in CT229: the total crack length only extended for ~200 μm, while CT228 showed a crack extension of ~700 μm during the same cyclic loading period. For the interest of time, we moved forward to constant load again at 5203 hours and

decided to focus only on measuring CT228 for SCC growth response in EOC water chemistry. Figure 39 documents this 2nd attempt to evaluate the water chemistry change effect between LiOH and KOH in the EOC water condition. The SCCGR of CT228 started at 1.2×10^{-8} mm/s and gradually decreased to a very low value of 5×10^{-10} mm/s, essentially suggesting no SCC growth. This is believed to be due to the difficulty in obtaining measurable SCCGR as explained above, instead of the on-the-fly water chemistry changes made during the evaluation period. At this point, it seems that any additional action to try to grow the crack in water would not be effective or efficient. As a result, it was decided to temporarily remove both specimens from the test and try to grow the crack more aggressively by fatigue in air to see if it could alleviate the lack-of-growth issue.

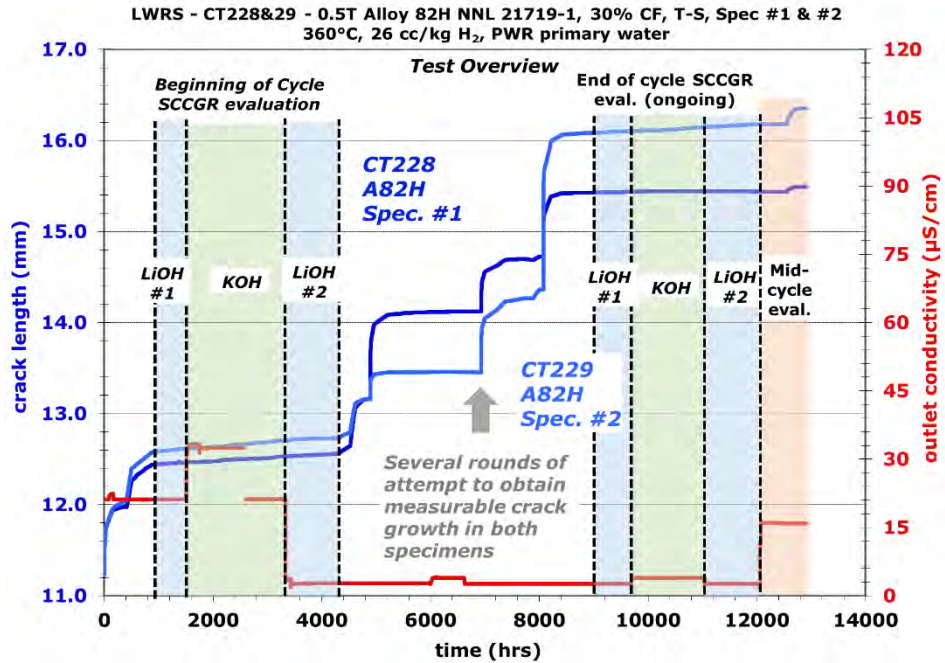


Figure 32. Test overview of crack growth response in the two Alloy 82 specimens CT228 & 229 tested in T-S orientation. The effect of KOH vs. LiOH on the SCCGR of both specimens was evaluated in 360°C simulated PWR primary water at a constant stress intensity of 30 MPa√m.

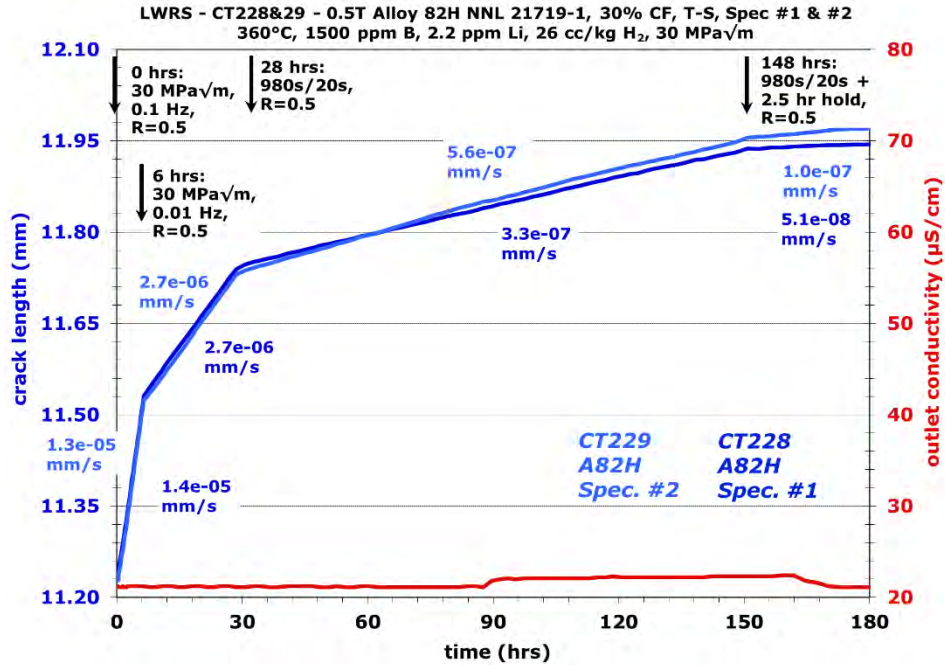


Figure 33. Crack growth response of CT228 & 229 during the initial cyclic loading transition steps in 360°C simulated PWR primary water.

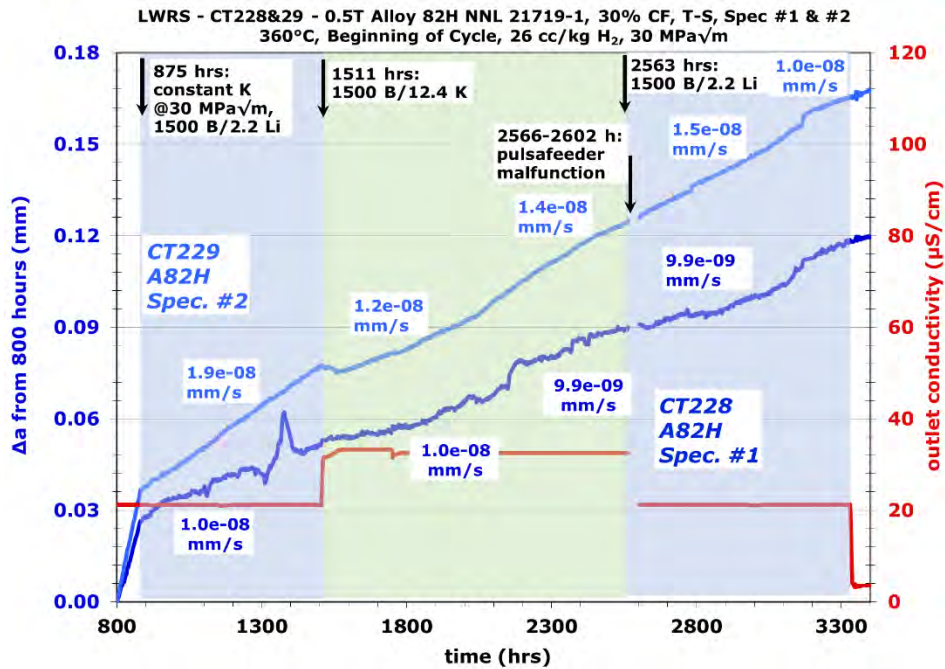


Figure 34. SCCGR response of CT228 & 229 in 360°C PWR primary water BOC chemistry with on-the-fly changes between LiOH and KOH. The concentrations of B, Li, and K in the plot are shown in ppm.

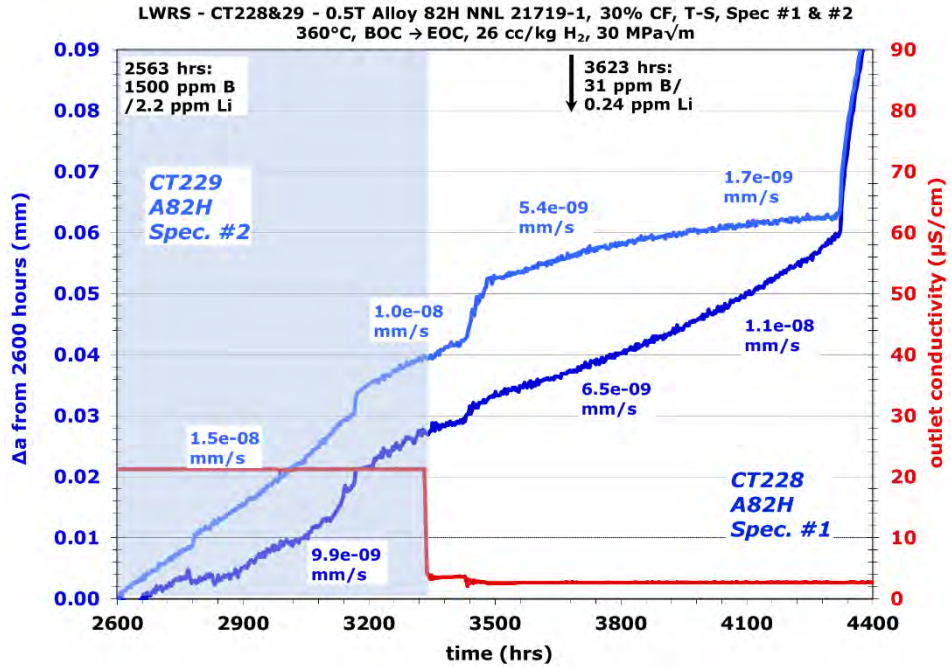


Figure 35. SCCGR response of CT228 & 229 in 360°C PWR primary water during the transition from BOC LiOH to EOC LiOH water chemistry.

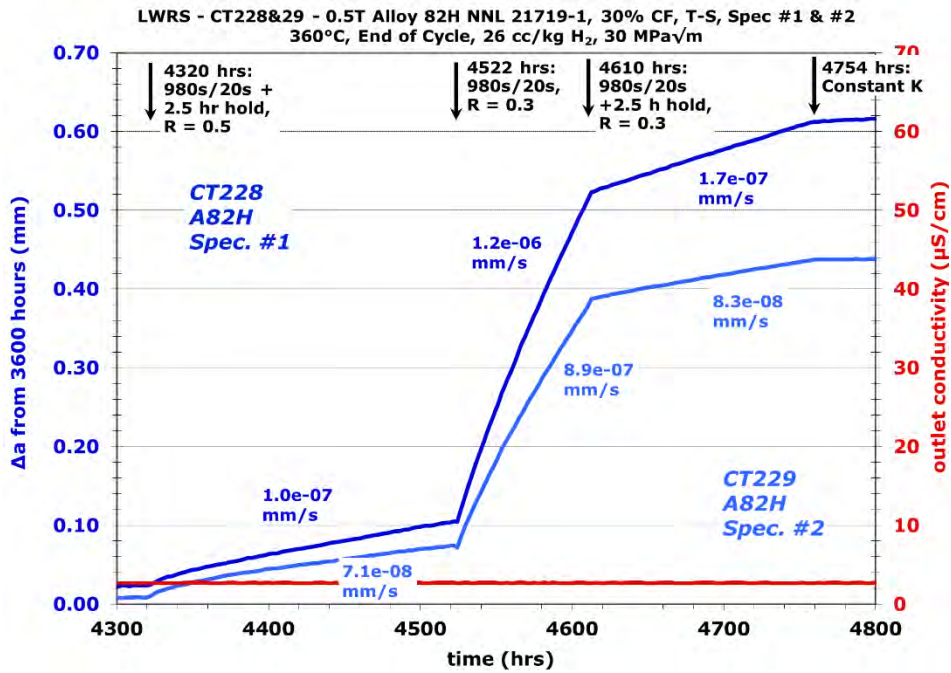


Figure 36. Crack growth response of CT228 & 229 during the first attempt to adjust crack growth behavior after the water chemistry change from BOC LiOH to EOC LiOH.

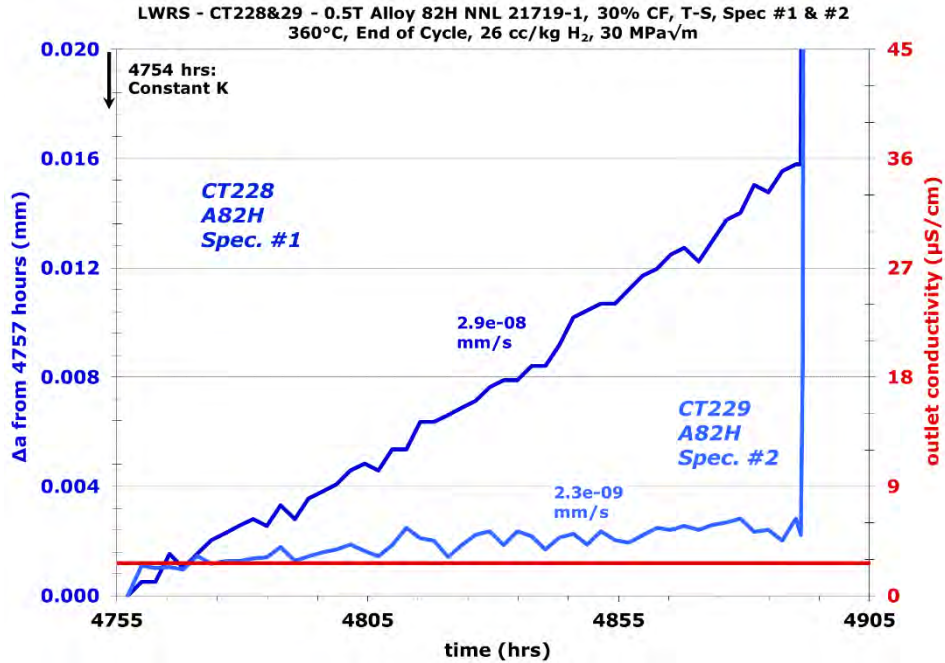


Figure 37. The 2nd attempt to measure SCCGR response of CT228 & 229 in 360°C PWR primary water EOC LiOH water chemistry.

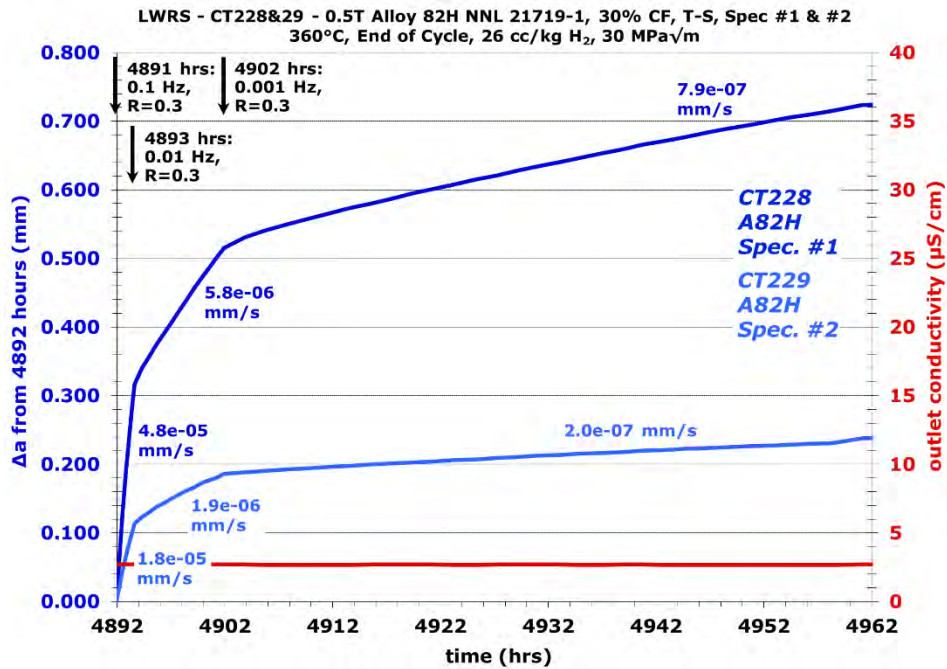


Figure 38. Crack growth response of CT228 & 229 during the second attempt to adjust crack growth behavior in the EOC LiOH water chemistry.

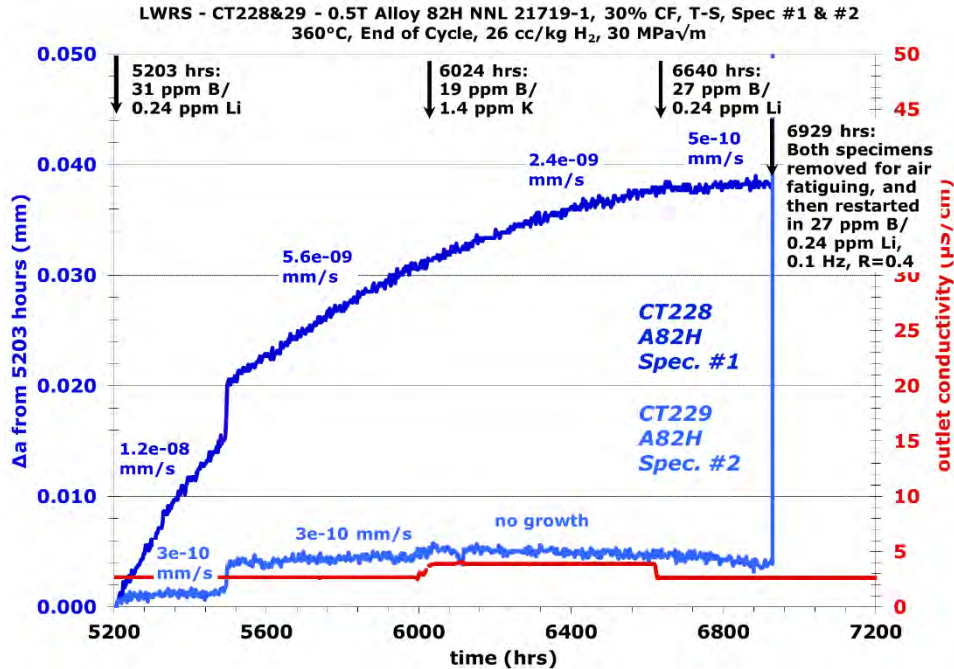


Figure 39. The 2nd attempt to measure the SCCGR response of CT228 & 229 in 360°C PWR primary water EOC water chemistry with on-the-fly changes between LiOH and KOH.

As shown in Figures 40 and 41, the crack length in the side grooves was measured for CT228 and CT229, respectively, before and after further fatiguing in air to ensure the desired crack extension was achieved. Uneven crack length was observed in CT228 before air fatigue, which was improved with additional ~400 µm growth on Side A and ~200 µm growth on Side B with an average crack length estimated at ~3.3 mm from the notch (Figure 40). A similar crack length was achieved in CT229 by growing the crack for another ~1.5 mm in both side grooves, reaching an average crack length of ~3.55 mm (Figure 41). The specimens were then reloaded into the test system, and the test restarted with a series of cyclic loading with decreasing frequency in an effort to transition the fatigue crack into IGSCC crack (Figure 42). CGR was similar to those obtained earlier in the test under the same loading conditions, so we switched to constant K evaluation for the 3rd attempt to evaluate the SCC growth behavior of Alloy 82 in the EOC water chemistry. Stable, acceptable SCCGR (8.3×10^{-9} mm/s) and fast SCCGR ($\sim 2.5 \times 10^{-8}$ mm/s) were measured from CT228 and CT229, respectively, during the first ~400 hours, before a sudden decrease in SCCGR occurred in both specimens at ~7730 hours (Figure 43). Crack growth appeared to have completely stopped in CT228, while the SCCGR of CT229 also dropped by one order of magnitude to 3.3×10^{-9} mm/s, which was considered too slow for meaningful SCCGR assessments. Since both specimens exhibited good SCC growth in the first 400 hours of constant load evaluation, it was suspected that IGSCC growth was still continuing in isolated packets in both specimens, but an increasing fraction of uncracked ligaments hindered DCPD measurements of the actual SCCGR. As a result, a gentle cycle + hold loading was applied at 7893 hours in an effort to break the ligaments and straighten crack front in both specimens. While this method appeared effective in CT229 indicated by the high CGR during the cycle+hold step and then 5X higher SCCGR at the subsequent constant K step, the situation did not improve for CT228. Given the earlier experience that further transition in water did not greatly alleviate the lack of crack growth in these specimens, it was decided to temporarily remove the specimens again from the test to further grow the crack by air fatigue.

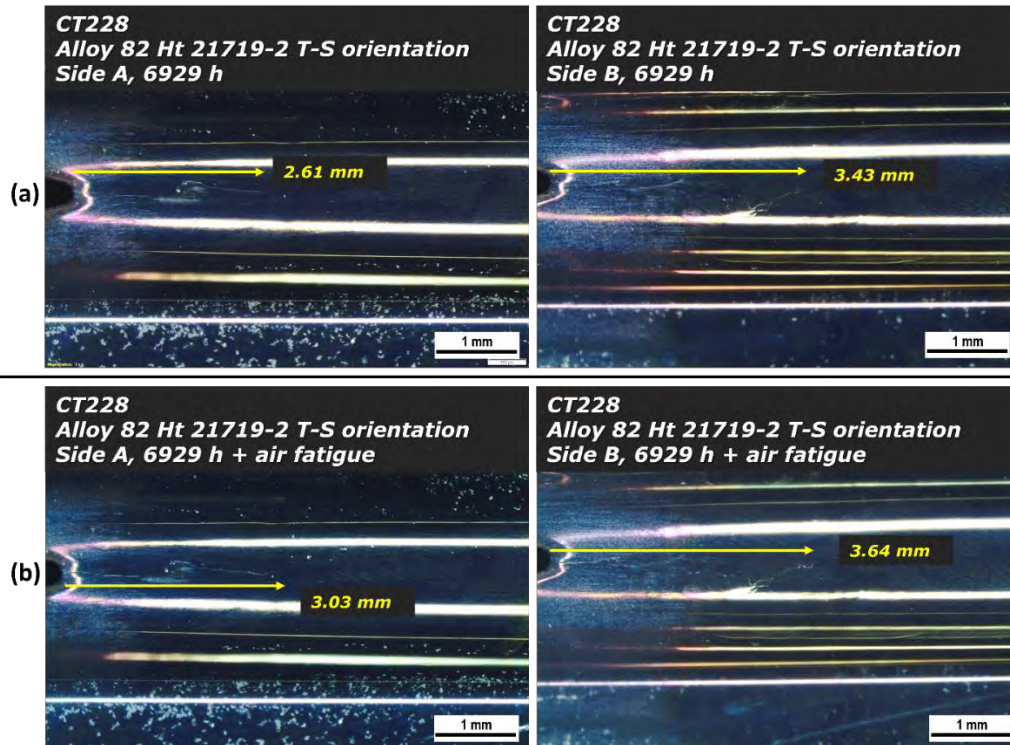


Figure 40. Crack length measurement in the side grooves of CT228 after 6929 hours of testing in 360°C simulated PWR primary water: (a) immediately after the specimen was removed from testing and (b) after additional fatigue in air to grow the crack in the specimen.

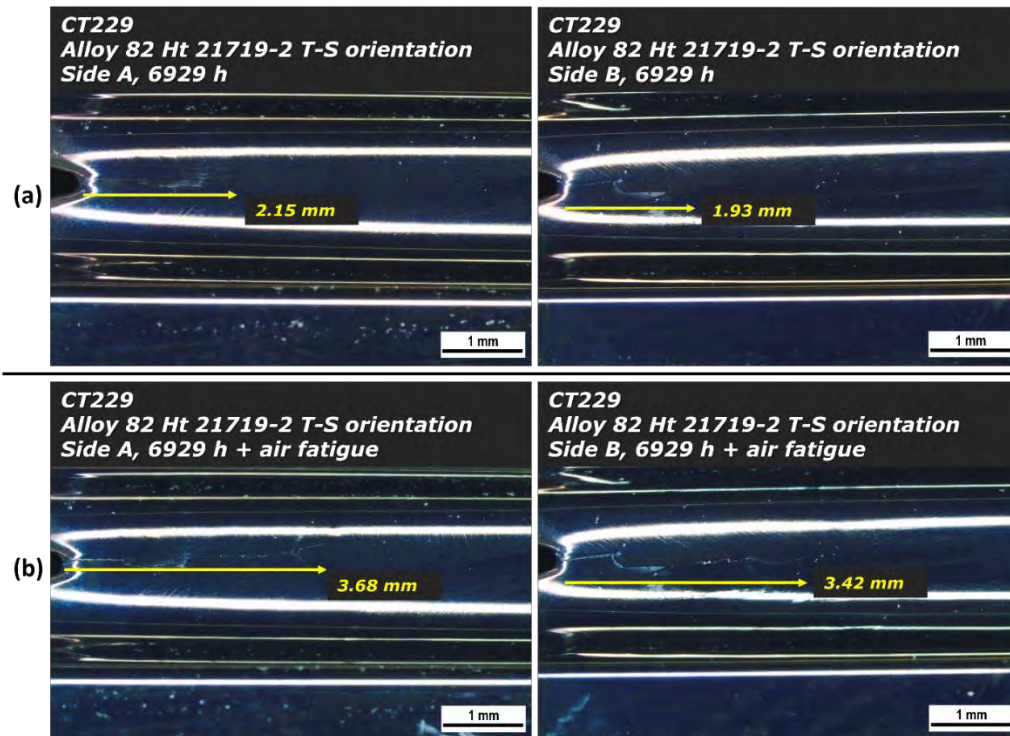


Figure 41. Crack length measurement in the side grooves of CT229 after 6929 hours of testing in 360°C simulated PWR primary water: (a) immediately after the specimen was removed from testing and (b) after additional fatigue in air to grow the crack in the specimen.

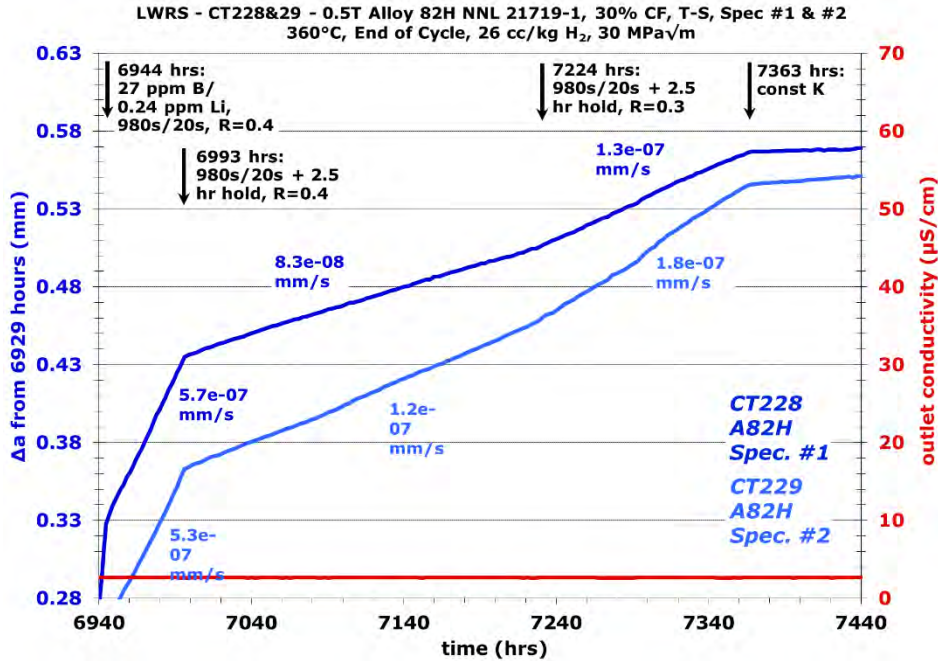


Figure 42. CGR response of CT228 & 229 in transition steps after the specimens were fatigued in air for the 1st time to adjust the crack length.

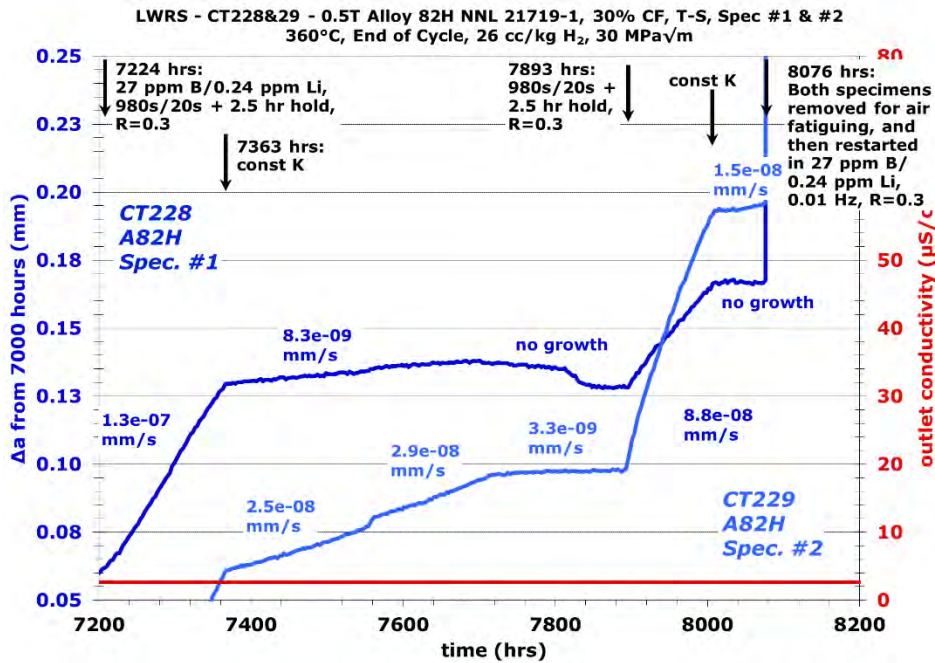


Figure 43. The 3rd attempt to measure the SCCGR response of CT228 & 229 in 360°C PWR primary water EOC LiOH water chemistry.

This next round of air fatiguing appeared to have successfully grown a uniform crack front in CT228, where a similar crack length of 4.21–4.27 mm was measured in the two side grooves post-fatiguing (Figure 44). However, it also appeared to have aggravated the unevenness of the crack front in CT229 and

resulted in an average crack length that was a few 100s of μm longer in CT229 than in CT228 (Figure 45). Nevertheless, to complete the test in time, no further adjustment of crack length was performed, and both specimens were returned to test. The difference in the total crack length in the two specimens soon became apparent during the serial cyclic loading steps after the test resumed in water, where CT229 consistently exhibited a higher CGR at every loading step (Figure 46). The difference further increased after the test transitioned to constant K evaluation, where crack continued to grow in CT229 with measurable SCCGRs but completely stopped in CT228. As a result, it was decided to focus only on the SCCGR response of CT229 for the EOC water chemistry evaluation. As shown in Figure 47, fluctuations of $\pm 2X$ in SCCGR occurred a few times during the entire EOC evaluation period, highlighting the high variability in SCC growth in weld metals. Therefore, a longer evaluation time was given to each LiOH and KOH condition, and on-the-fly changes in water chemistry were only made after stable SCCGR was measured for at least 200 hours at the previous step. No obvious change in SCCGR occurred during the water chemistry switch from LiOH to KOH and back to KOH, and all three phases evaluated exhibited a similar average SCCGR of 1.0×10^{-8} mm/s.

Despite the challenges in obtaining measurable SCCGR, the evaluation in EOC water condition was finally completed at $\sim 12,000$ hours with convincing data measured in CT229, and the test moved directly to the final SCC evaluation by changing to the mid-cycle water chemistry on-the-fly (Figure 48). Coincidentally, SCC growth slowed down in CT229 around the time of this water chemistry change with no measurable SCCGR afterward. However, this was believed to be related to intrinsic SCC growth behavior (likely fingered growth) but not the change in water chemistry. We first continued the test as-is without any intervention to see if the SCCGR could increase in this specimen like it did a few times during the EOC evaluation. However, after waiting for ~ 500 hours without measurable SCCGR, we briefly implemented a gentle cycle plus hold and managed to reactivate crack growth in this specimen. A stable SCCGR of 1.4×10^{-8} mm/s was measured for the last ~ 250 hours of testing, close to the average SCCGR measured in the EOC evaluation period.

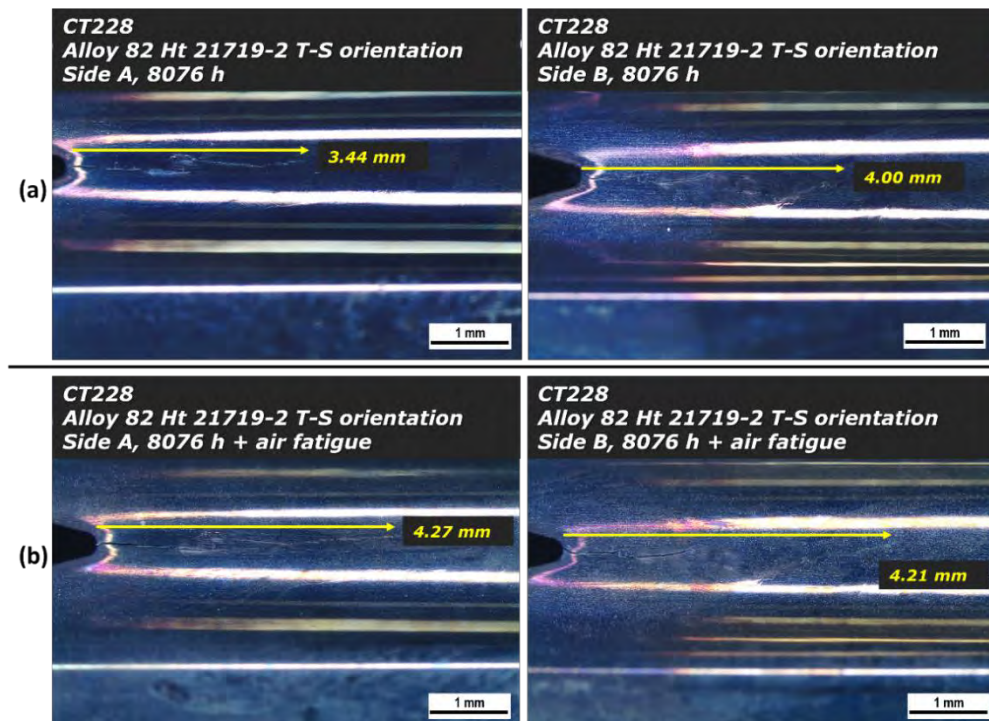


Figure 44. Crack length measurement in the side grooves of CT228 after 8076 hours of testing in 360°C simulated PWR primary water: (a) immediately after the specimen was removed from testing and (b) after additional fatigue in air to grow the crack in the specimen.

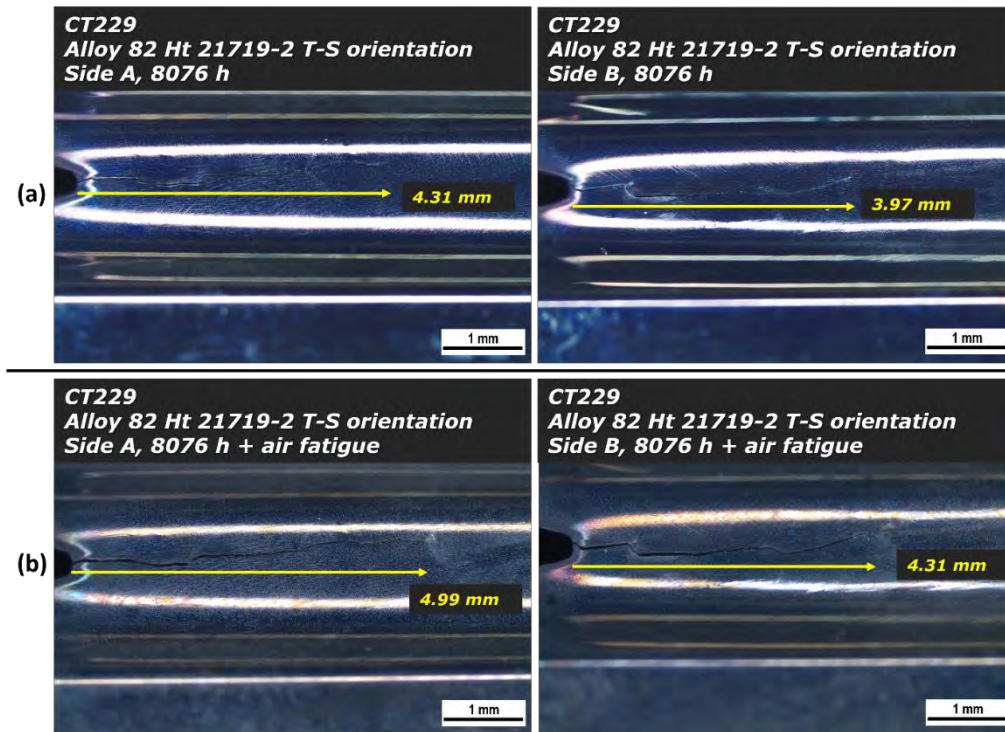


Figure 45. Crack length measurement in the side grooves of CT229 after 8076 hours of testing in 360°C simulated PWR primary water: (a) immediately after the specimen was removed from testing and (b) after additional fatigue in air to grow the crack in the specimen.

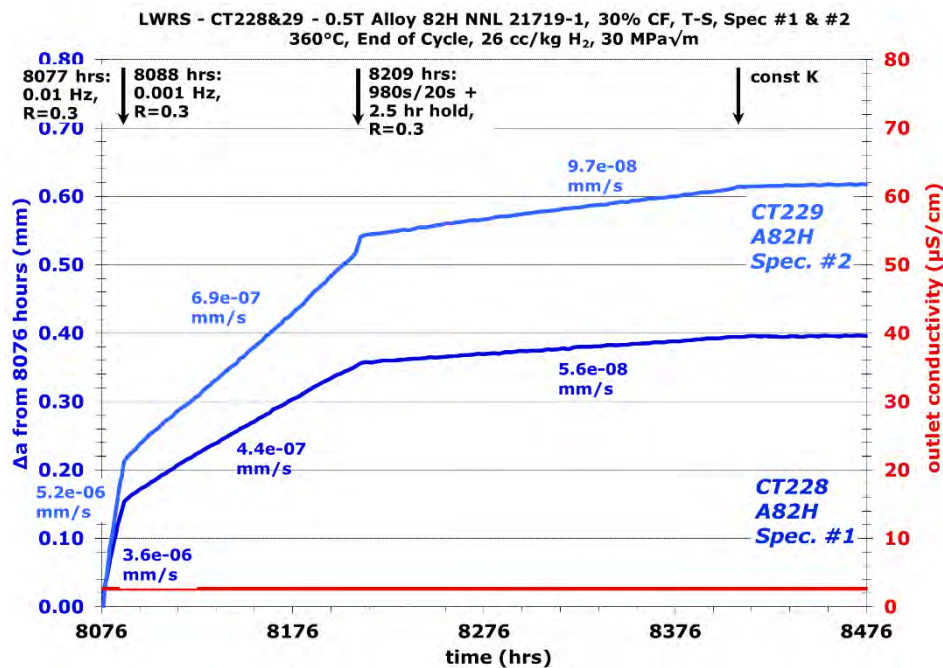


Figure 46. CGR response of CT228 & 229 in transition steps after the specimens were fatigued in air for the 2nd time to adjust the crack length.

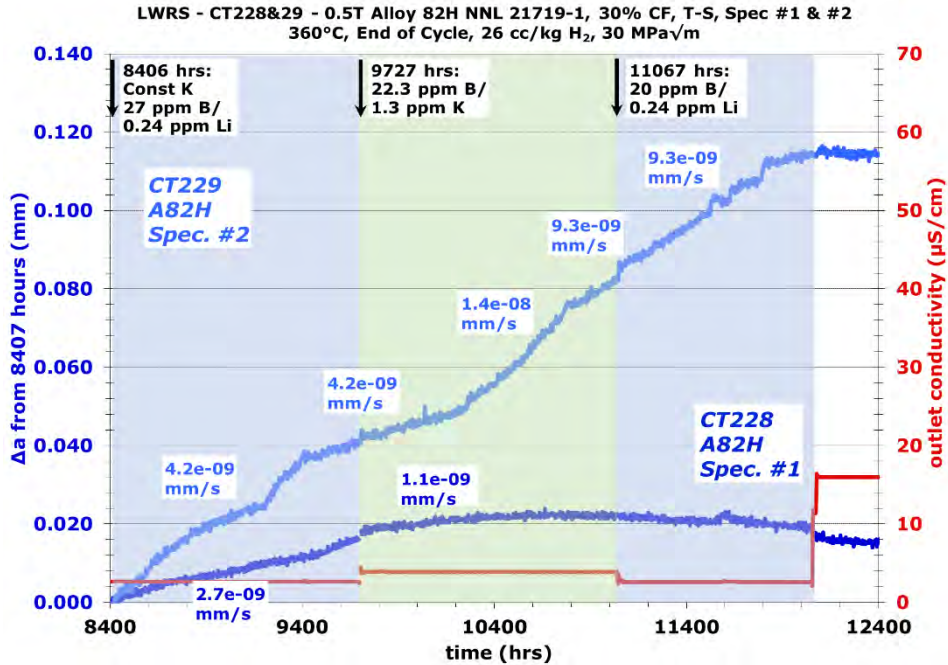


Figure 47. SCCGR response of CT228 & 229 in 360°C PWR primary water EOC chemistry with on-the-fly changes between LiOH and KOH.

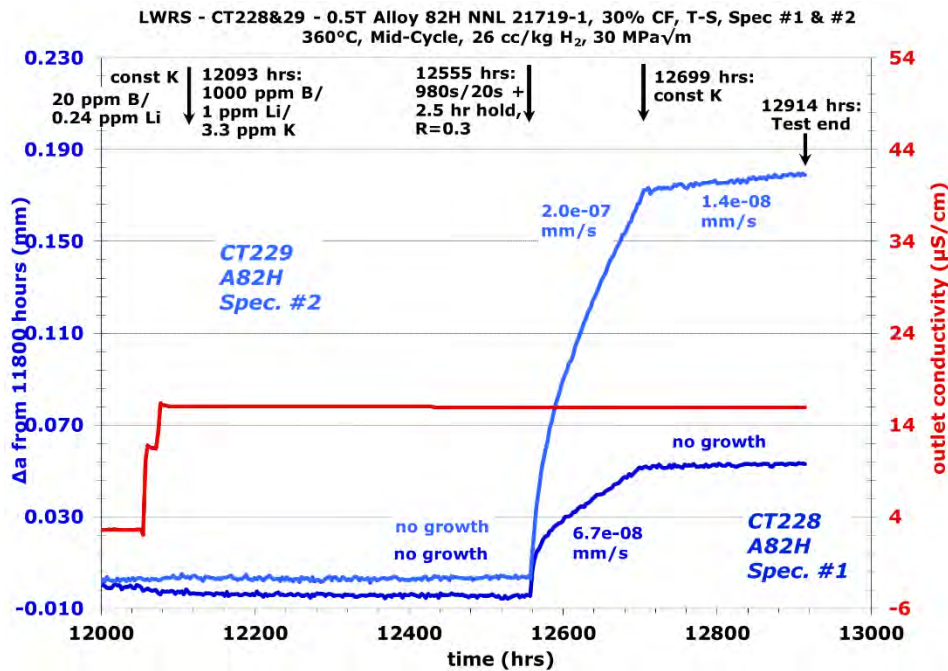


Figure 48. SCCGR response of CT228 & 229 in 360°C PWR primary water with on-the-fly changes from EOC LiOH to mid-cycle water chemistry.

2.4.2 Post-Test Fractography Examination

After completing the SCC growth test, CT228 and CT229 were removed from the test system for post-test characterization. Both specimens were cross-sectioned in the thickness direction into one 1/3 and one 2/3 slices. The 2/3-thickness slice from both specimens was fatigued open in air for crack surface observations, while the 1/3-thickness slices were given an ultrafine (colloidal silica as the last step) in cross-section to provide an alternate observation of crack morphology. The optical images of the crack growth surface on CT228 and CT229 are presented in Figures 49 and 51, respectively. As speculated during testing, both specimens showed significant fingered growth on the crack growth surface. While the maximum crack length from the notch in these “fingered” packets was 6.91 mm for CT228 and 9.23 mm for CT229, the total crack length measured by DCPD was shorter due to the unbroken ligaments between these packets. To calibrate the DCPD estimated crack length to the actual crack growth in the specimens, measurements were conducted on the crack growth surface of CT228 and CT229. Because the DCPD estimation of SCCGR was based on the cross-sectional area change caused by crack growth, the measurement on the crack growth surface focused on determining the location where the surface area across the slice width from the last continuous crack front equals the surface area of IGSCC growth developed in isolated packets beyond this continuous crack front. Following this method, the total crack length from the notch is measured at 5.29 mm in CT228 (Figure 49) and 6.99 mm in CT229 (Figure 51). In comparison, the DCPD estimated total crack length from the notch was 4.74 mm for CT228 and 6.21 mm for CT229. These values suggest that DCPD underestimated the crack length in both specimens, but only by ~11–12%. Because the differences between the actual and estimated crack length were relatively small and would not significantly alter the SCCGR values estimated by DCPD, no further correction was needed.

A closer look at the crack growth surface of these two specimens revealed that while several IG packets had grown continuously from the initial fatigue crack and extended long into the material, they were separated by transgranular regions showing a distinctive purple-brownish metallic sheen. These were likely the unbroken ligaments that had posed challenges to effective SCCGR measurements that were later broken up by fatigue in water or air. In fact, some ligaments remained intact during the test but were torn apart during the post-test fatigue opening, as marked in Figure 49 for CT228.

The SEM examination on the cross-section of the 1/3-thickness slice of CT228 also suggested a complex IGSCC propagation route. As shown in Figure 50, during the last quarter of the crack length (~4 mm from the notch), the crack diverted from the main path, turned upward and disappeared into the metal, re-appeared along an SGB ~1 mm above the primary cracking plane, disappeared again and then showed up parallel along the loading direction before it approached back to the primary cracking plane. Cracking bifurcation was also observed in the 1/3-thickness slice cross-section of CT229 (Figure 52), and the contrast in the SEM-BSE image suggests that it took place when the crack entered from one welding pass into the next, where the original SGB the crack had followed terminated, prompting the crack to find another route for continued growth. In summary, these post-test observations confirmed the complexity of the crack growing path inside this Ni-base weld metal, and the features found during post-test characterizations were consistent with the hypotheses we made when difficulties in growing SCC were encountered during testing. It also suggests that the variability in the measured SCCGR was primarily due to the complexity of the SCC growth path but not the changes made in water chemistry.

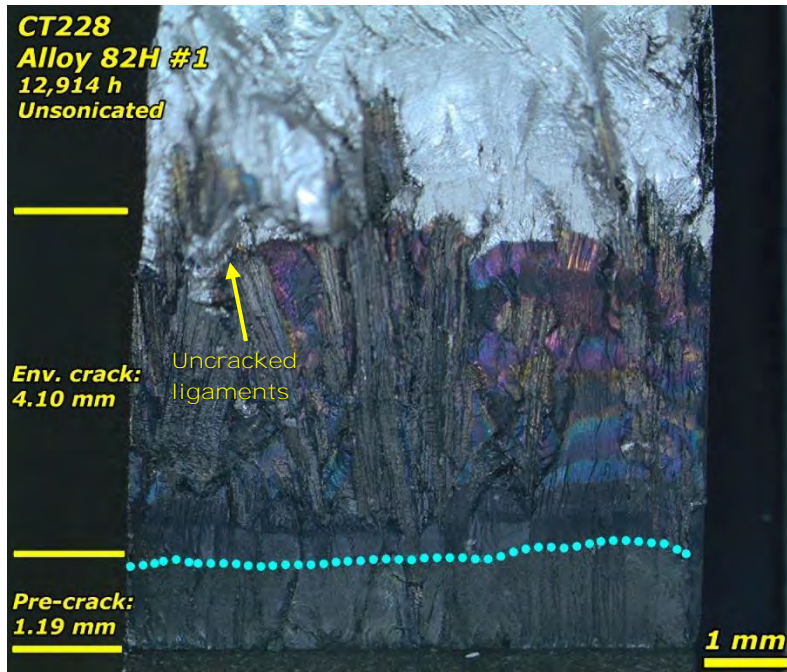


Figure 49. Post-test optical image of the crack growth surface in the 2/3-thickness slice of CT228. The extent of the fatigue pre-crack is highlighted by the blue dotted line. The average pre-crack length and environmental crack length are marked in yellow on the left.



Figure 50. Post-test SEM BSE image showing the crack morphology in the cross-section of the 1/3-thickness slice sectioned from CT228.

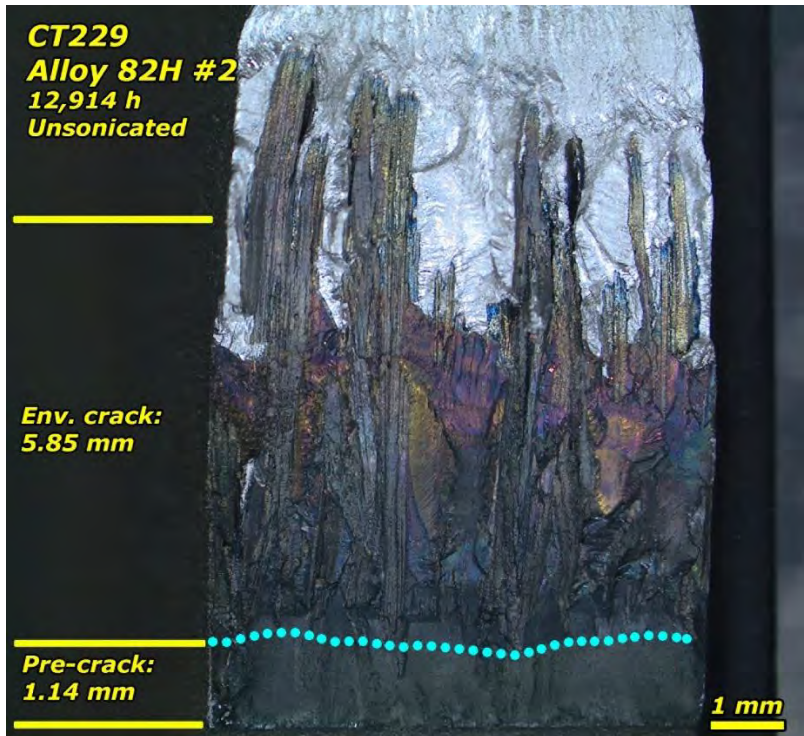


Figure 51. Post-test optical image of the crack growth surface in the 2/3-thickness slice of CT229. The extent of the fatigue pre-crack is highlighted by the blue dotted line. The average pre-crack length and environmental crack length are marked in yellow on the left.

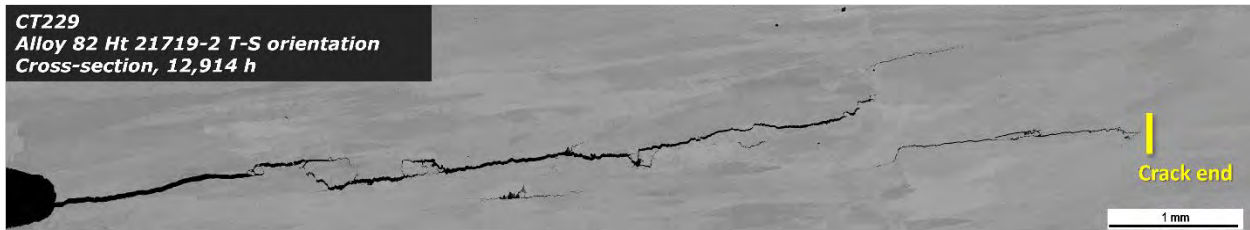


Figure 52. Post-test SEM BSE image showing the crack morphology in the cross-section of the 1/3-thickness slice sectioned from CT229.

2.5 Discussion

Weibull analyses of the SCC initiation data were performed on the two data sets to address the variability observed in SCC initiation times in the BOC KOH and LiOH water chemistries. A standard Weibull analysis was performed on the BOC KOH and BOC LiOH data in which only failed events (i.e., initiated) were considered. A censored Weibull analysis was also performed on the BOC LiOH data to take into account the one “non-failure” (i.e., no initiation) event. A detailed description of the censored Weibull approach as it pertains to SCC initiation data with non-initiated values is presented in Reference [9]. Graphical results of the Weibull analyses are shown in Figure 53 on the BOC KOH initiation data and in Figures 54 (standard) and 55 (censored) on the BOC LiOH initiation data, while Table 5 provides more information on the mean, standard deviation, and the SCC initiation times at the 95% confidence interval of a cumulative failure probability of 10%, 50%, and 90% from the Weibull analyses. A comparison between the standard Weibull analysis results on the BOC KOH and BOC LiOH data suggests that SCC initiation generally occurs 4X earlier in BOC LiOH than in BOC KOH water chemistry and within a tighter band at each failure probability. However, the SCC initiation time band for the BOC LiOH water

chemistry was significantly broadened after adding the one “non-failure” event into the analysis. As shown in Table 5, SCC initiation time at the 95% percentile extends over at least two orders of magnitude for each failure probability specified, which easily envelopes the SCC initiation time range obtained from the standard Weibull analysis on BOC KOH data. Considering the complexity of the microstructure of this weld metal and the potential existence of welding defects, it seems reasonable to attribute the relatively large variability observed in SCC initiation times and the non-failure event to intrinsic material conditions instead of the water chemistry. This notion is also supported by Figure 16, which showed that specimens loaded to a similar degree of plastic strain usually initiated within a similar time interval, whether they were tested in KOH or LiOH-containing water. In addition, no obvious difference was observed in cracking morphology in all specimens tested in these two water chemistries (Section 2.3.2). As a result, it can be concluded that replacing LiOH with KOH as the pH moderator in PWR primary water BOC condition would not adversely affect the SCC initiation behavior of Alloy 82.

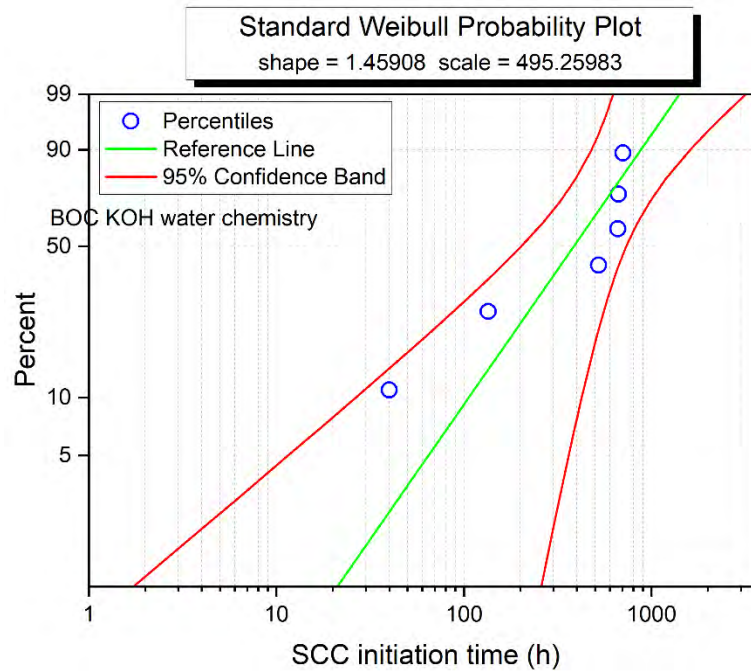


Figure 53. Standard Weibull analysis (cumulative failure vs. hours) with a 95% confidence interval based on the SCC initiation times acquired on Alloy 82 at yield stress in 360°C water with 1500 ppm B and 12.4 ppm K. All six specimens have initiated and are considered failures in this analysis.

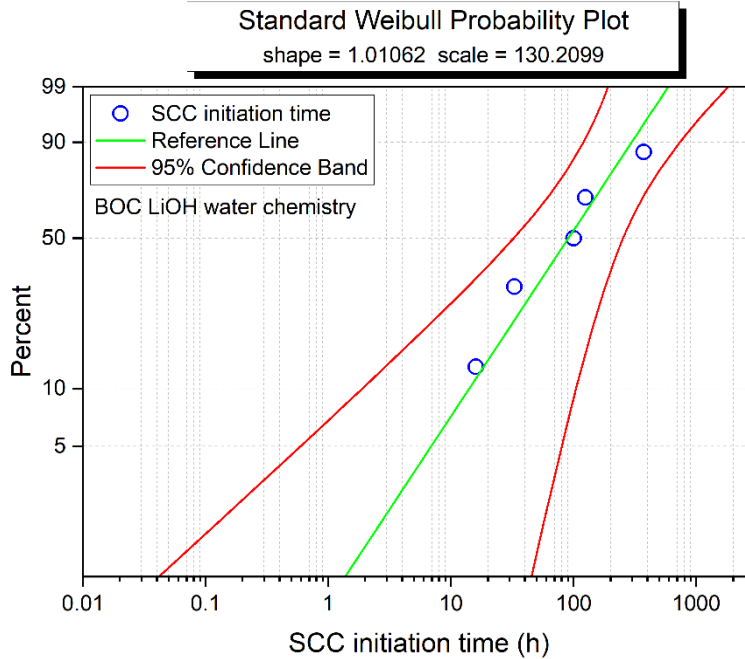


Figure 54. Non-censored (standard) Weibull analysis (cumulative failure vs. hours) with a 95% confidence interval based on the SCC initiation times acquired on Alloy 82 at yield stress in 360°C water with 1500 ppm B and 2.2 ppm Li. This fit only takes into account the five initiated specimens as failures. The non-initiated sample is excluded from this analysis.

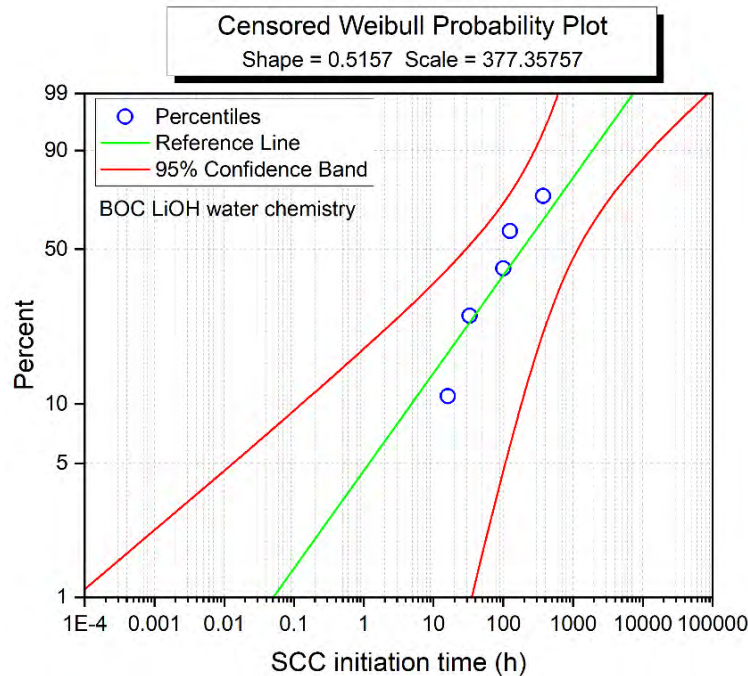


Figure 55. Censored Weibull analysis (cumulative failure vs. hours) with a 95% confidence interval based on the SCC initiation times acquired on Alloy 82 at yield stress in 360°C water with 1500 ppm B and 2.2 ppm Li. Five out of the six specimens have initiated and are considered failures in this analysis. This censored analysis also accounts for the one non-failure event.

Table 5. Mean, standard deviation, and failure times at lower and upper 95% confidence intervals for 10%, 50%, and 90% cumulative failures of Alloy 82. The mean and standard deviation for the LiOH water chemistry were calculated with the inclusion of the non-initiated value.

Water Chemistry, ppm	Mean	Std Dev	10% Failures	50% Failures	90% Failures
1500 B, 12.4 K	455 h	293 h	~26–424 h	~202–734 h	~478–1,608 h
1500 B, 2.2 Li (non-censored)	129 h	144 h	~2–105 h	~32–253 h	~120–734 h
1500 B, 2.2 Li (censored)	467 h	836 h	~0.12–181 h	~29–1,171 h	~281–12,887 h

Despite the challenge in producing measurable SCCGR in CT228 during the later half of the SCC growth test as described in 2.4.1, sufficient data was collected to evaluate the effect of water chemistry change between KOH and LiOH on the SCC growth behavior of Alloy 82. Table 6 summarizes the average SCCGR obtained on each specimen over the entire interim they stayed in each specific water chemistry. Very stable SCCGR was observed in CT228 during the entire BOC water chemistry condition, regardless of the on-the-fly changes made from LiOH to KOH and back to KOH. CT229 showed slightly more fluctuation during the same period with lower SCCGR measured in the BOC KOH phase than in the BOC LiOH phase before and after the chemistry switch, but the largest difference was ~32% and was within the uncertainty (i.e., ±50%) of the measurement method (Section 2.2.2.3). A similar situation was observed during the EOC and mid-cycle evaluation, with minor differences measured in SCCGR at each phase that are within statistical error of the DCPD detectability. In addition, the change in SCCGR was assessed over a 200-hour interim immediately before and after each swap between LiOH and KOH in the BOC and EOC water conditions (Table 7). CT228 exhibited no change in SCCGR during the swaps between LiOH and KOH in the BOC water chemistry. The same was observed for CT229 during evaluations in the EOC water chemistry. The largest percentage change of ~37% in SCCGR occurred during the first on-the-fly change from LiOH to KOH in the BOC water condition in CT229, which was still within the uncertainty of the DCPD detectability. It should be kept in mind that the SCCGR measured in this test does not reflect the local SCCGR in the “fingered” IGSCC packets (shown in Section 2.4.2) that are likely to be much faster. Nevertheless, they provide a means to evaluate the more macroscopic crack growth behavior in bulk, and the results suggest that replacing LiOH with KOH in assessed water chemistries did not negatively impact the SCC growth in Alloy 82.

Table 6. Average SCCGR measured by DCPD in each water chemistry tested for CT228 and CT229.

Specimen ID	Average SCCGR (mm/s)						Mid-cycle
	Beginning-of-cycle			End-of-cycle			
	LiOH	KOH	LiOH	LiOH	KOH	LiOH	
CT228	1.0×10^{-8}	1.0×10^{-8}	9.9×10^{-9}	N/A	N/A	N/A	N/A
CT229	1.9×10^{-8}	1.3×10^{-8}	1.5×10^{-8}	8.3×10^{-9}	8.9×10^{-9}	9.3×10^{-9}	1.4×10^{-8}

Table 7. Percentage change in SCCGR during the last 200 hours before and the first 200 hours after on-the-fly change between LiOH and KOH in the BOC and EOC water chemistries for the Alloy 82 CT specimens.

% change in SCCGR Specimen	Beginning-of-cycle		End-of-cycle	
	LiOH→KOH	KOH→LiOH	LiOH→KOH	KOH→LiOH
CT228	0%	0%	N/A	N/A
CT229	-36.7%	7.1%	0%	0%

3. Update on the Long-Term SCC Initiation Testing of Cold Worked Alloy 690

3.1 Chapter Overview

SCC initiation testing on CW Alloy 600 in PWR primary water has demonstrated that IG oxidation is the precursor to SCC initiation in this material [5, 10, 11]. In comparison, an equivalent degradation and cracking process does not exist in CW Alloy 690. Due to a much higher Cr content in alloy composition, a compact chromia layer readily forms on the surface above GBs that intersect the surface when the material is exposed to high-temperature water. This chromia layer remains protective after long-term exposure to high stresses. As a result, CW Alloy 690 is considered resistant to SCC initiation. However, recent laboratory studies have revealed an alternate mechanism of crack initiation in this material through the formation and growth of GB cavities induced by creep when the material is highly cold worked [12-17]. To better understand the evolution of GB cavities and to predict the degradation of Alloy 690 in realistic PWR operating conditions, systematic long-term SCC initiation testing is being performed at PNNL to evaluate factors influencing GB cavity evolution in Alloy 690 materials. Seven commercial Alloy 690 heats with variations in thermal-mechanical history (solution annealed (SA), mill annealed (MA), and thermally treated (TT)), cold work level (12–31%), and applied stress (1.0 vs. 0.9 YS) are being investigated. To date, the test consists of five phases with ~1-year exposure for Phase I–III, 2-year exposure for Phase IV, and ongoing Phase V. Precursor damage and crack morphology observed during the test interruption after each of the first three phases were reported in detail in previous milestone reports [18-21]. The test completed Phase IV exposure in late summer of 2022, and extensive non-destructive specimen examinations were performed to document precursor damage and crack evolution in the first quarter of FY 2023. After that, the test was restarted for Phase V exposure, which is ongoing as of the writing of this report. This chapter will summarize key results from the Phase IV specimen characterization, and provide a status update on the ongoing Phase V testing.

3.2 Materials and Specimen Preparation

3.2.1 Alloy 690 Materials and Pre-Test Microstructures

Three Alloy 690 control rod drive mechanism (CRDM) heats and four plate/bar heats are being investigated in this project. The chemical composition and heat treatment history for each heat in the as-received condition are listed in Tables 8 and 9. Prior to testing, the materials were either CF in the direction orthogonal to the processing plane or cold-rolled (CR) along the processing direction to produce a cold work level ranging from 12 to 31% reduction in thickness (Figure 56). Most combinations of these material and cold work conditions had already been evaluated for SCC growth behavior as part of an NRC project at PNNL, where six of the seven heats (except Allvac X87N-1) in the 20-30%CW condition exhibited moderate-to-high SCC crack growth rates in simulated PWR primary water (Figure 57[7]). Pre-testing microstructures were characterized for these materials in both the as-received (AR) and CW conditions, which will be summarized below to facilitate results interpretation in the latter sections.

Table 8. Composition of the AR Alloy 690 materials.

Source/Manufacturer and Heat #	Composition, wt%
Valinox/Valinox RE243 CRDM Tube 2360	Ni-28.9Cr-10.4Fe-0.02C-0.3Mn-0.35Si-0.14Al-0.23Ti-0.024N-0.008P-0.0005S
EPRI/Sumitomo E67074C CRDM Tube	Ni-29.8Cr-9.8Fe-0.02C-0.29Mn-0.23Si-0.03Cu-0.0002S
EPRI/TK-VDM (Doosan) 133454 CRDM Bar	Ni-29.1Cr-8.9Fe-0.020C-0.26Mn-0.29Si-0.26Al-0.32Ti-0.01Cu-0.02N-0.005P-<0.002S-0.002B
ANL/Special Metals NX3297HK12 plate	Ni-29.5Cr-9.9Fe-0.03C-0.20Mn-0.07Si-0.01Cu-<0.001S
GEG/Allvac B25K bar	Ni-29.3Cr-9.2Fe-0.034C-0.22Mn-0.06Si-0.26Al-0.37Ti-<0.01Cu-0.03N-0.006P-<0.0003S-<0.001B
EPRI/TK-VDM 114092 plate	Ni-29.5Cr-9.5Fe-0.020C-0.25Mn-0.26Si-0.32Al-0.36Ti-<0.01Cu-0.003P-<0.002S
EPRI/Allvac X87N-1	Ni-30.0Cr-9.2Fe-0.020C-0.20Mn-0.05Si-<0.01Cu-<0.0003S

Table 9. Heat treatment and mechanical properties of the AR Alloy 690 materials (RT: room temperature, WQ: water quenched, AC: air cool, NM: not measured).

Source/Manufacturer and Heat #	Heat Treatments	RT Yield Stress (MPa)	Hardness (HV)
Valinox/Valinox RE243 CRDM Tube 2360	1122°C/~1 min, WQ + 716-725°C/10.5 h, AC	255	157
EPRI/Sumitomo E67074C CRDM Tube	Anneal + 725°C/10 h/AC	NM	NM
EPRI/TK-VDM (Doosan) 133454 CRDM Bar	1045°C/4 h/WQ + 720°C/10 h/AC	263	165
ANL/Special Metals NX3297HK12 plate	1038°C/2 h/AC	NM	173
GEG/Allvac B25K bar	996°C/20 min/AC	294	173
EPRI/TK-VDM 114092 plate	1030°C/1 h/WQ + 715°C/10 h/AC	285	155
EPRI/Allvac X87N-1	1030°C/4 h/WQ +727°C/5 h/AC	265	NM

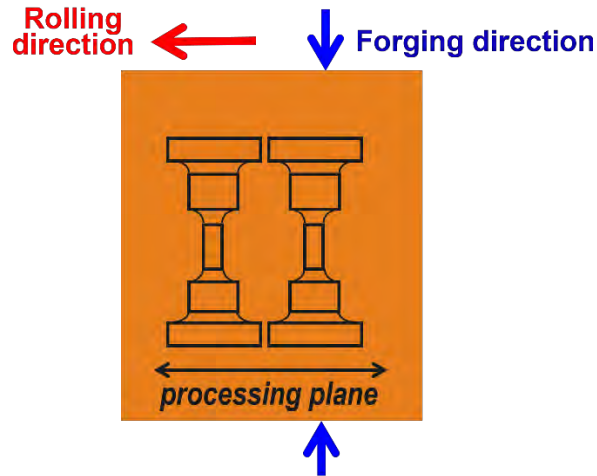


Figure 56. Illustration showing the orientation of specimens and cold work direction in the Alloy 690 materials.

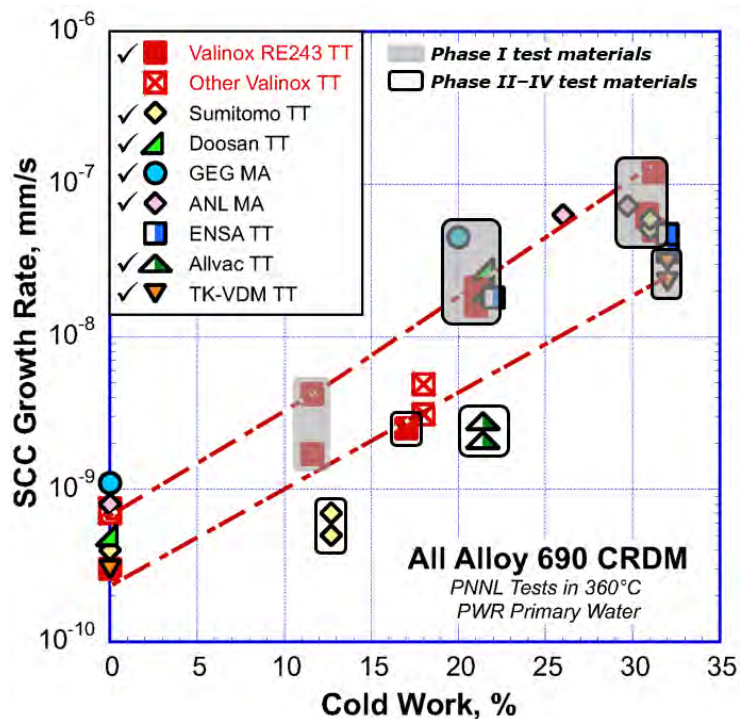


Figure 57. SCCGR response of TT/MA Alloy 690 materials at $\sim 30 \text{ MPa}\sqrt{\text{m}}$ acquired from the NRC SCC crack growth program [7, 22]. The heat and cold work levels selected for SCC initiation evaluation at each stage were checked in the label box and circled in the plots.

3.2.1.1 Examinations of As-Received Alloy 690 Microstructures

Alloy 690 is usually MA or TT for plant applications, which introduces carbide precipitation in the matrix or at high-angle grain boundaries (HAGBs). In all the tested Alloy 690 heats, carbide precipitation was limited to a few isolated GBs in the MA GEG B25K bar heat with a planar banded microstructure. All the other heats exhibit a semi-continuous GB carbide coverage, but the size and spacing between carbides vary significantly from heat to heat, as shown in the SEM backscatter electron (BSE) images in Figure 58 for the CRDM tubing materials and in Figure 59 for the plate/bar materials. The TT CRDM tubing heats

Sumitomo E67074C and Valinox RE243 exhibit the most uniform and closely spaced small, sub-micrometer carbides, while the TT plate heat TK-VDM 114092 exhibits similar size carbides but an up-to-10 times larger spacings in between. In comparison, the TT CRDM bar heat Doosan 133454 and MA plate heat ANL HK3297HK12 have much larger, micrometer-sized IG carbides that are more widely spaced. The MA ANL plate heat also features a unique distribution of extensive intragranular TiN particles. Electron backscatter diffraction (EBSD) pattern quality maps were also acquired on these materials to document grain orientations and size. As shown in the pattern quality maps in Figure 60, the CRDM materials generally have a larger grain size than the plate/bar materials. The Valinox and Doosan CRDM materials have a similar grain size of $\sim 90\ \mu\text{m}$, while the Sumitomo CRDM has a smaller average grain size of $\sim 35\ \mu\text{m}$ with significant twinning. The TK-VDM plate material has a similar grain size to Sumitomo CRDM but much less twinning. The ANL and Allvac plate materials have the same average grain size of $\sim 25\ \mu\text{m}$, and the GEG bar material exhibits the finest microstructure with an average grain size of $\sim 15\ \mu\text{m}$. The grain size measurements did not count the twinning boundaries. Table 10 provides a more detailed summary of the grain size and carbide distribution for all the Alloy 690 CRDM and plate/bar heats currently being evaluated in the SCC initiation test. A summary of the carbide distribution characteristics and grain size in the as-received condition of all the Alloy 690 heats in test is provided in Table 10.

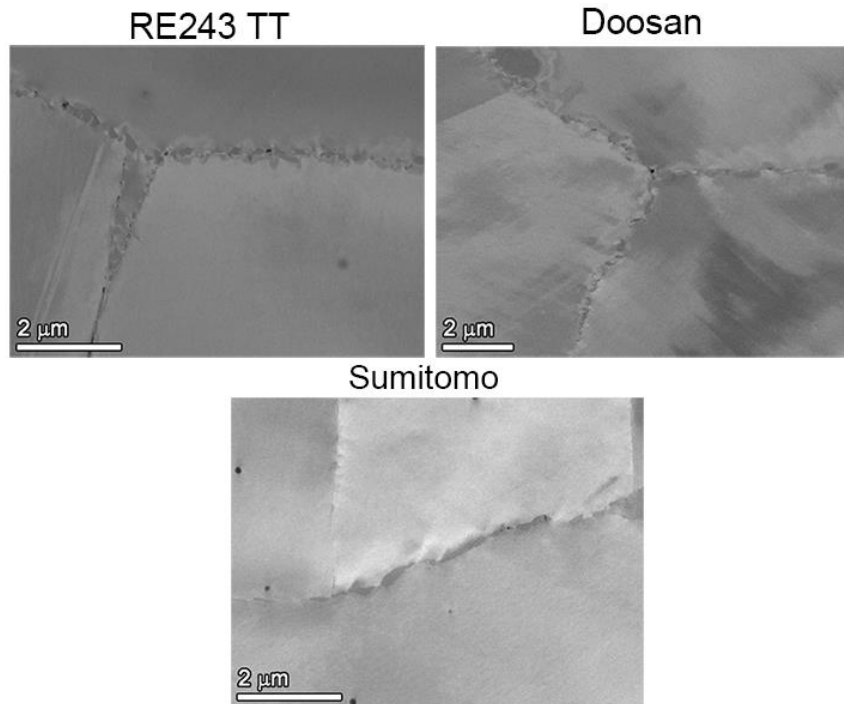


Figure 58. SEM-BSE images illustrating the GB microstructures for the three Alloy 690TT CRDM materials in the as-received condition.

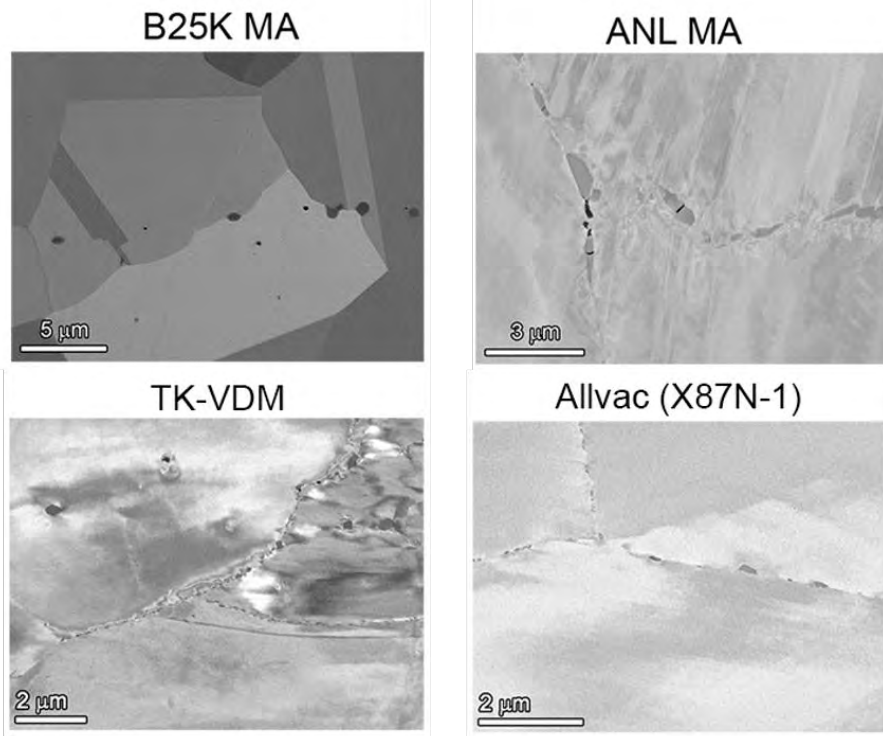
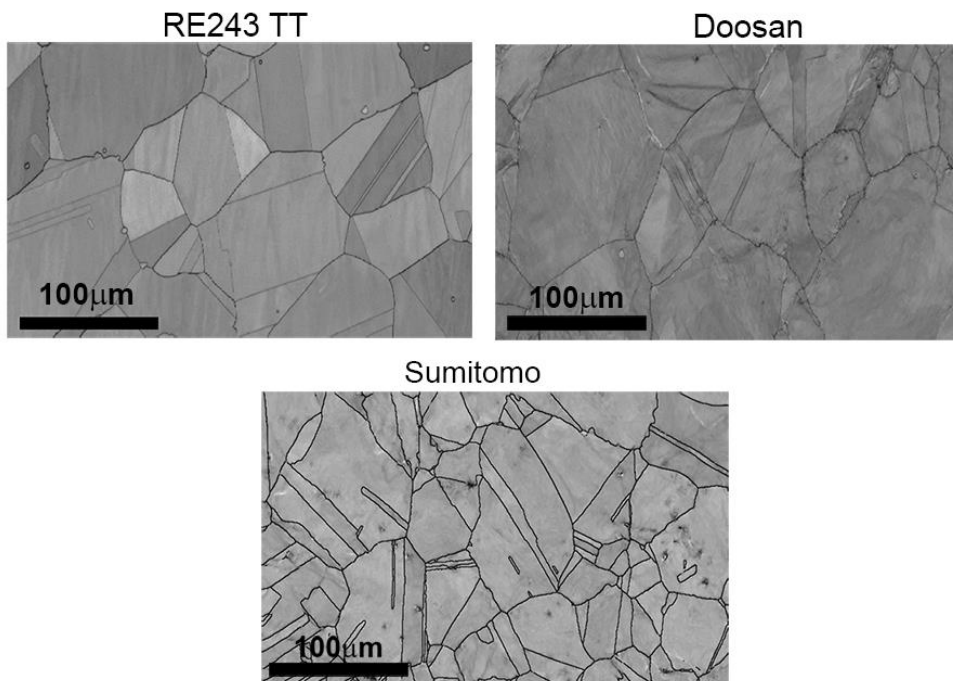


Figure 59. SEM-BSE images illustrating differences in the GB carbide microstructures for each of the four Alloy 690 plate/bar materials in the as-received condition.



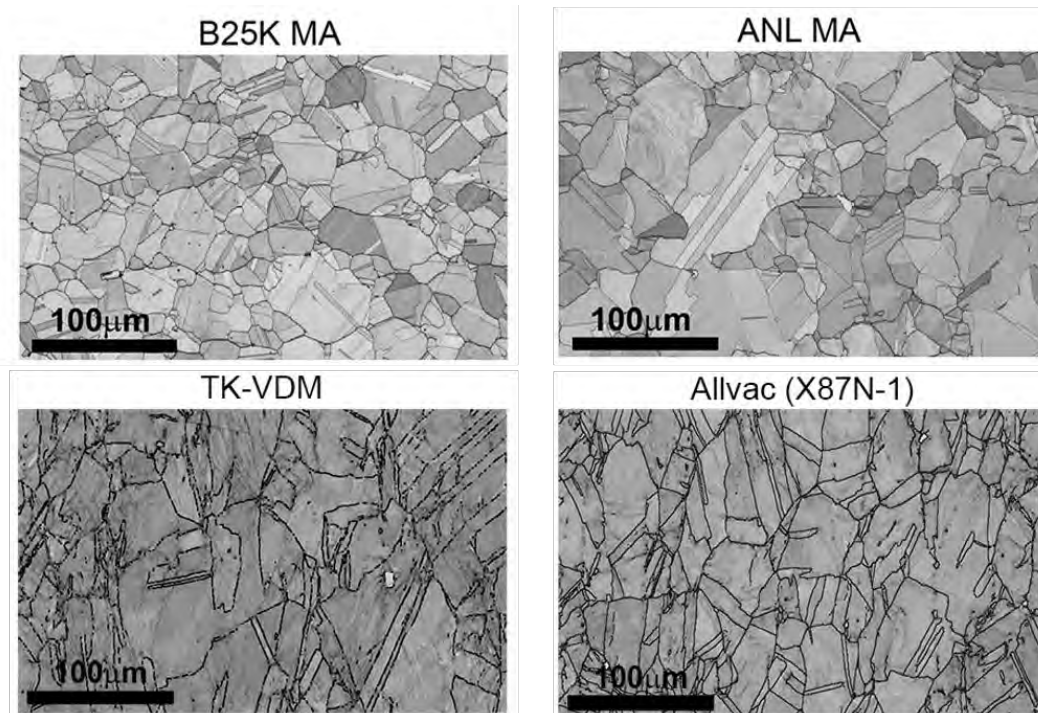


Figure 60. EBSD pattern quality maps showing the general microstructure and grain size for the seven Alloy 690TT/MA materials in the as-received condition.

Table 10. Summary of grain size and carbide distributions for materials selected for SCC initiation testing.

Material	Grain Size (μm)	Carbide Location, Size	GB Carbide Density
CRDM Materials			
Valinox RE243 TT	~90	IG, 50–200 nm	Semi-continuous, spacing ~100 nm
Doosan 133454 TT	~90	IG, 1–5 μm	Semi-continuous, spacing ~0.5–2 μm
Sumitomo E67074C TT	~35-40	IG, 50–300 nm	Semi-continuous, spacing ~100 nm
Plate/Bar Materials			
GEG B25K MA	~10-15	TG and isolated IG, 1–3 μm	Low
ANL HK3297HK12 MA	~20-25	IG, 0.5–3 μm	Semi-continuous, spacing ~0.2–2 μm
TK-VDM 114092 TT	~35-40	IG, 50-200 nm	Semi-continuous, spacing ~0.1–0.5 μm
Allvac X87N-1	~20-25	IG, 50-200 nm	Semi-continuous, spacing ~200 μm

3.2.1.2 Permanent Damage in CW Alloy 690 Materials

It is important to note that the pre-test cold work introduced permanent damage in all CW materials. This damage was present at GBs in the form of cavities and cracked precipitates, of which the size and density strongly depend on the GB microstructure. An example is shown in Figure 61, where the permanent damage induced by cold work in four 31%CF Alloy 690TT materials is highlighted. The images are shown at the same scale, directly comparing the size and distribution of cavities and cracks between these heats. The materials exhibiting fine carbides at GBs often feature small voids at a higher density on certain boundaries. In comparison, the damage in the materials having larger and more widely spaced carbides is also larger and more spaced out. In addition, an obvious increase was noted in the density of these pre-existing defects as the cold work level increased. In Figure 62, representative pre-existing defect distribution produced by cold forging the Valinox CRDM Alloy 690TT material to different cold work levels are presented at the same scale to facilitate comparison. The images are shown at locations in each specimen where multiple IG voids and cracked carbides were identified. Such locations became increasingly harder to find as the cold work level decreased, where the number and size of the IG defects also dopped with decreasing cold work. All the other Alloy 690 TT/MA materials had a similar trend. The degree of cold work-induced damage is qualitatively summarized for the CRDM materials in Table 11 and for plate/bar materials in Table 12, respectively.

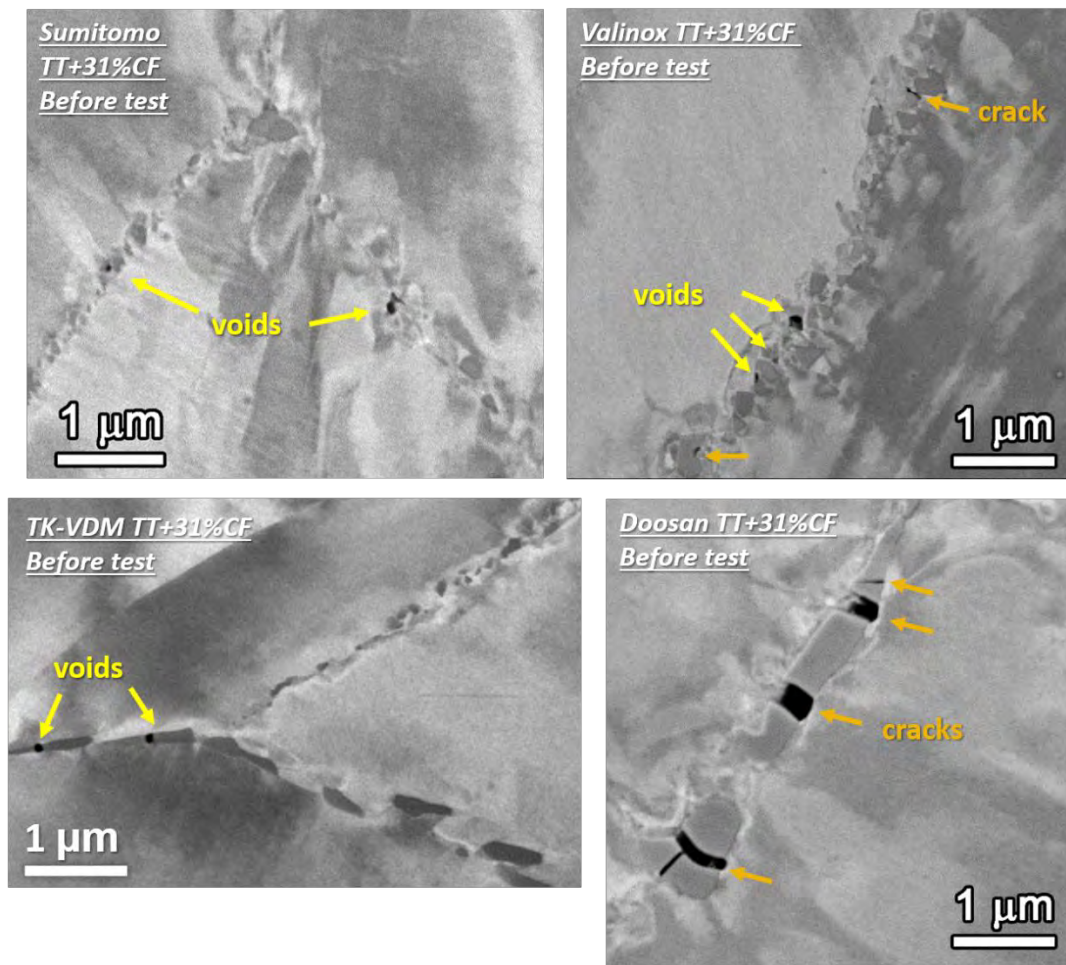


Figure 61. SEM-BSE images illustrating the permanent damage (highlighted by arrows) induced by cold work in four 31%CF Alloy 690TT materials. All images are shown at the same scale.

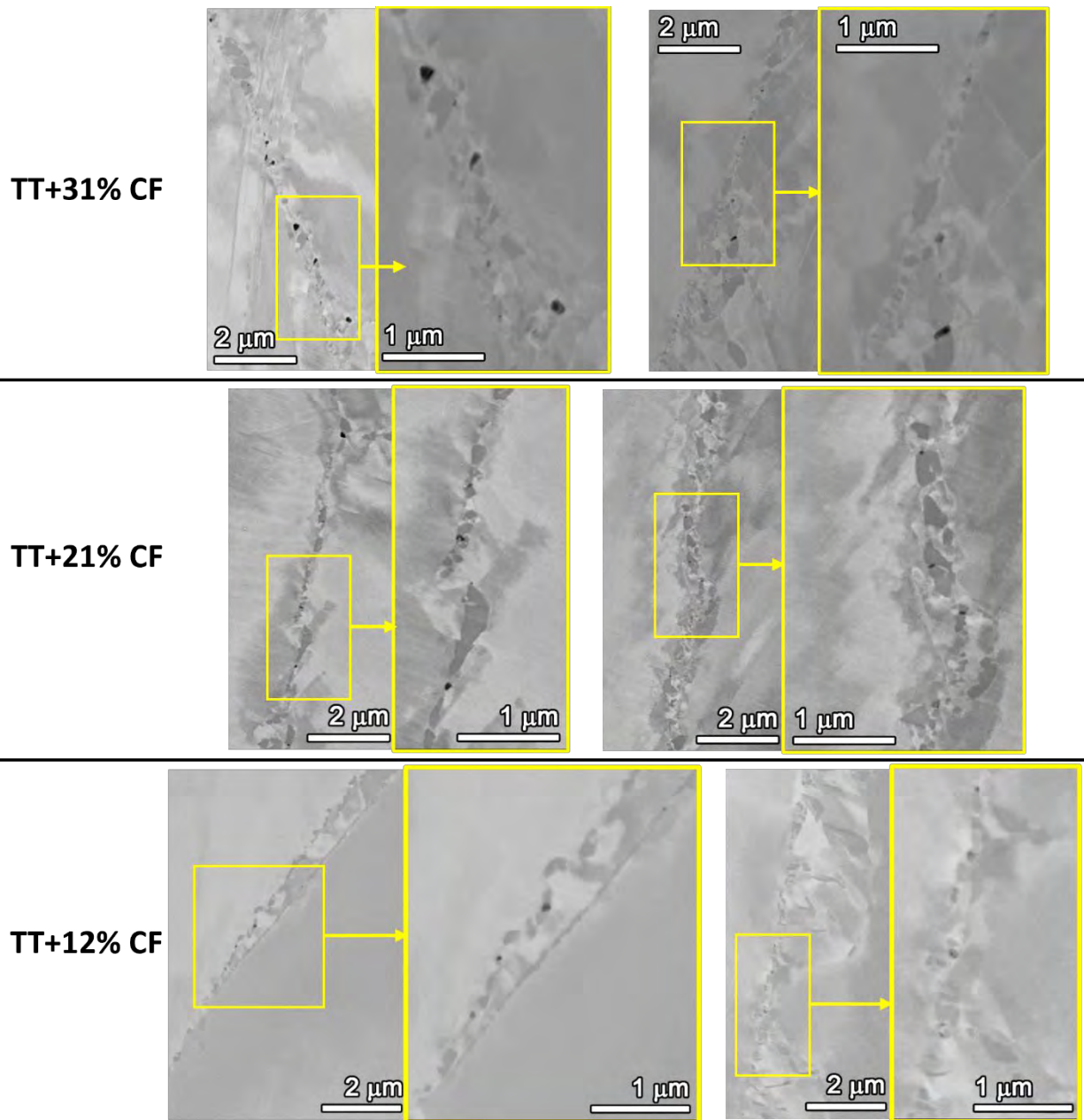


Figure 62. Representative pre-existing defect distribution in the thermally treated Valinox CRDM material cold forged to 12, 21, and 31% reduction in thickness.

Table 11. Summary of carbide microstructure and damage morphology in Alloy 690TT CRDM materials in different cold work levels evaluated in the SCC initiation test.

Material	AR GB Carbide Microstructure		Cold Work Induced GB Damage	
	Location, Size	Density, Spacing	Density of Cracked GB Precipitates	IG Void Density
Valinox RE243 12% CF*	IG, 50–200 nm	Semi-continuous, spacing ~100 nm	None–Low	Low
Valinox RE243 21% CF*			Low	Low–Moderate
Valinox RE243 31% CF*			Low	Moderate
Sumitomo E67074C 21% CF	IG, 50–200 nm	Semi-continuous, spacing ~100 nm	Low	Low–Moderate
Sumitomo E67074C 31% CF			Low	Moderate
Doosan 133454 21% CF	IG, 1–5 μm	Semi-continuous, spacing ~0.5–2 μm	Low	Low–Moderate
Doosan 133454 31% CF			Low	Moderate

Table 12. Summary of carbide microstructure and damage morphology in Alloy 690 plate and bar materials in different cold work levels evaluated in the SCC initiation test.

Material	AR GB Carbide Microstructure		Cold Work Induced GB Damage	
	Location, Size	Density, Spacing	Density of Cracked GB Precipitates	IG Void Density
ANL MA 26% CR	IG, 0.5–3 μm	Semi-continuous, spacing ~0.2–2 μm	Moderate	Moderate–High
GEG MA 18% CR	Primarily TG, 1–3 μm	Low density, unevenly distributed	None–Low	None–Low
TK-VDM 114092 22% CF	IG, 50–200 nm	Semi-continuous, spacing ~0.2–0.5 μm	Low	Low–Moderate
TK-VDM 114092 31.9% CF			Low	Moderate
Allvac X87N-1 21% CF	IG, 50-200 nm	Semi-continuous, spacing ~0.2–0.5 μm	Low-Moderate	Moderate

3.3 Test Update

3.3.1 Test Overview

Figure 63 provides an overview of the test progress specifying the heat and material conditions evaluated in each phase with their up-to-date exposure times. A more detailed status summary of all the tested and in-test specimens is provided in Table 13.

To date, the test consists of five phases. The exposure during the first three phases each lasted ~1.1 years. The original test materials were selected based on their SCCGR response obtained in the NRC SCC crack growth program [7, 22] as summarized in Figure 57. The research started with three Alloy 690TT CRDM heats and three TT/MA plate/bar heats exhibiting high SCC crack growth rates at CW levels from 20–30%. These materials are being tested for SCC initiation in 12–31% CW conditions. Since surface-breaking short IG cracks were observed in several highly CW Alloy 690TT specimens after Phase I exposure and were all found to be associated with GB cavity formation at crack tips, thirteen specimens were removed after Phase I exposure for destructive examination to document cavity distribution in bulk. Another thirteen new replacement specimens were added to the test at the start of Phase II exposure, expanding the test matrix to include more variations in GB carbide distribution (TT vs. SA), applied stress (100% vs. 90% YS), and heat IGSCC susceptibility (moderate-high CGR vs. low CGR in

moderately-highly CW condition). Phase I and II exposures were conducted on thirty-six specimens in the large 36-specimen LWRS SCC initiation test system (denoted as LWRS1 hereafter). Seven specimens were removed after Phase II exposure, with another ten new specimens added at Phase III exposure. Beginning at Phase III, the specimens that had been exposed for a longer time and were considered more susceptible to GB cavity formation were moved to a medium-size LWRS SCC test system (denoted as LWRS2 hereafter), increasing the total specimens in test to 39 for Phase III and later to 42 for Phase IV. This gave more flexibility in stopping the test to remove specimens once crack initiation is detected, while exposure can continue in LWRS1 without disturbance. It also allows referenced DCPD response to be monitored on these specimens, thus providing a more accurate determination of crack initiation. Because most specimens tested in Phase IV were in conditions less susceptible to GB cavity formation and growth than the specimens that were already removed from the test, the Phase IV exposure lasted for two years in LWRS1. However, Phase IV exposure was stopped for the six specimens tested in LWRS2 after reaching one year of exposure. This is because to complete another task under this project, LWS2 was used in FY21 and FY22 to evaluate the effect of LiOH vs. KOH-containing PWR primary water on the SCC initiation response of Ni-base alloys [1, 2]. In the late summer of 2022, LWRS1 was stopped after Phase IV testing reached a total exposure of two years, not long after DCPD detected crack initiation in a Sumitomo CRDM TT+31%CF specimen IN179 tested at 0.9 YS (Figure 64). All the specimens were removed from the test for detailed surface examinations to document precursor damage evolution. Upon completion of the examinations, all specimens from LWRS1 and LWRS2 were returned to test for Phase V exposure except the initiated specimen. In August 2023, Phase V testing has accumulated ~5,180 hours of exposure in LWRS2 and ~3,850 hours in LWRS1, with the original specimens now reaching a total exposure time of ~46,580–48,690 hours (5.2–5.6 years).

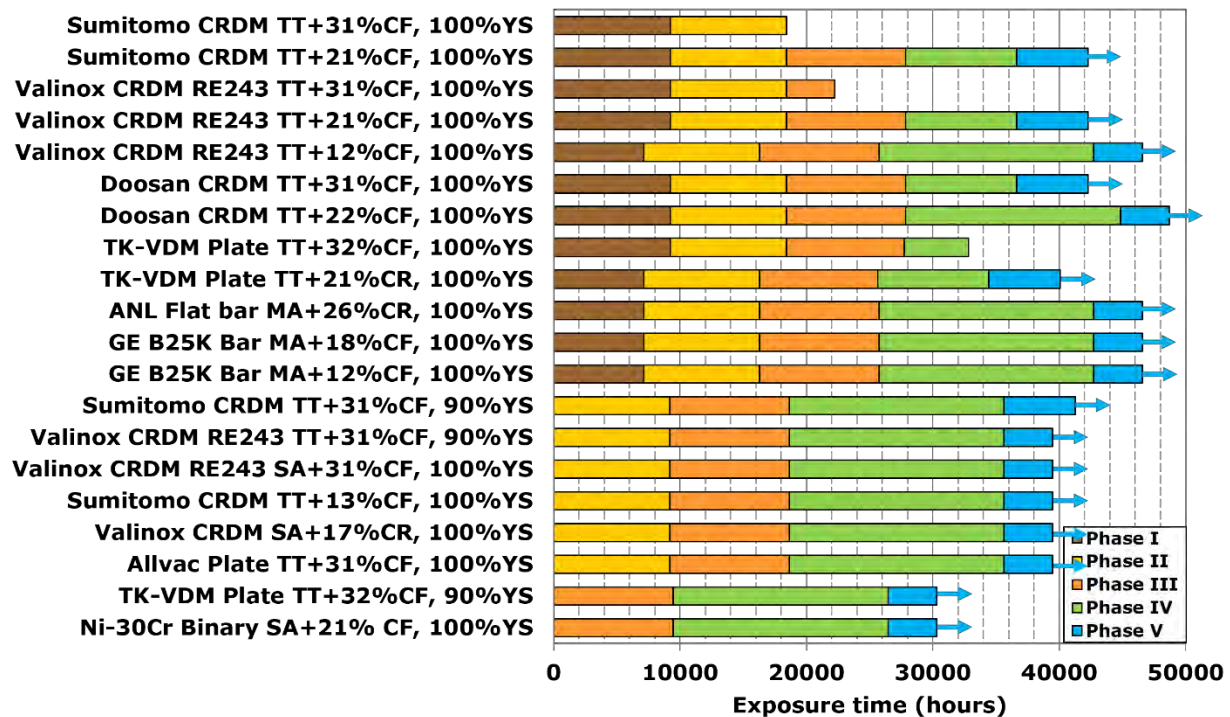


Figure 63. Up-to-date exposure time of the CW Alloy 690 materials evaluated in the long-term SCC initiation testing under LWRS. The arrows suggest that the test is ongoing as of August 2023 for the specified material and cold work conditions.

Table 13. Summary of material condition and SCC initiation testing status of all the tested Alloy 690 specimens as of August 2023.

Specimen	Material	Material Condition	Surface Condition	Applied Stress† (MPa)	Exposure time per phase (h)				
					I	II	III	IV	V*
IN024	Sumitomo CRDM	TT + 21% CF	1 µm	584	9220	9180	9440	8780	5680
IN025■	Sumitomo CRDM	TT + 21% CF	Ground	590	9220	9180	/	/	/
IN026■	Sumitomo CRDM	TT + 21% CF	Ground	590	9220	/	/	/	/
IN027	Valinox CRDM	TT + 21% CF	1 µm	523	9220	9180	9440	8780	5680
IN028■	Valinox CRDM	TT + 21% CF	Ground	525	9220	9180	/	/	/
IN029■	Valinox CRDM	TT + 21% CF	Ground	525	9220	/	/	/	/
IN030	Doosan CRDM	TT + 21.6% CF	1 µm	536	9220	9180	9440	17000	3850
IN031■	Doosan CRDM	TT + 21.6% CF	Ground	555	9220	9180	/	/	/
IN032■	Doosan CRDM	TT + 21.6% CF	Ground	555	9220	/	/	/	/
IN033■	Sumitomo CRDM	TT + 31% CF	1 µm	710	9220	/	/	/	/
IN034■	Sumitomo CRDM	TT + 31 % CF	Ground	710	9220	/	/	/	/
IN035■	Sumitomo CRDM	TT + 31% CF	Ground	710	9220	9180	/	/	/
IN036■	Valinox CRDM	TT + 31% CF	1 µm	720	9220	9180	3845	/	/
IN037■	Valinox CRDM	TT + 31% CF	Ground	720	9220	9180	/	/	/
IN038■	Valinox CRDM	TT + 31% CF	Ground	720	9220	/	/	/	/
IN039	Doosan CRDM	TT + 31% CF	1 µm	662	9220	9180	9440	8780	5680
IN040■	Doosan CRDM	TT + 31% CF	Ground	685	9220	9180	/	/	/
IN041■	Doosan CRDM	TT + 31% CF	Ground	685	9220	/	/	/	/
IN042■	TK-VDM Plate	TT + 31.9% CF	1 µm	676	9220	9180	9332	5066	/
IN043■	TK-VDM Plate	TT + 31.9% CF	Ground	676	9220	9180	/	/	/
IN044■	TK-VDM Plate	TT + 31.9% CF	Ground	676	9220	/	/	/	/
IN053	ANL Flat Bar	MA + 26% CR	1 µm	775	7110	9180	9440	17000	3850
IN054	ANL Flat Bar	MA + 26% CR	1 µm	769	7110	9180	9440	17000	3850
IN055■	ANL Flat Bar	MA + 26% CR	Ground	775	7110	/	/	/	/
IN056	GE B25K Bar	MA + 18.3% CF	1 µm	550	7110	9180	9440	17000	3850
IN057	GE B25K Bar	MA + 18.3% CF	1 µm	550	7110	9180	9440	17000	3850
IN058■	GE B25K Bar	MA + 18.3% CF	Ground	550	7110	/	/	/	/
IN059	TK-VDM Plate	TT + 21% CR	1 µm	653	7110	9180	9332	17000	5680
IN060	TK-VDM Plate	TT + 21% CR	1 µm	639	7110	9180	9440	17000	5680
IN061■	TK-VDM Plate	TT + 21% CR	Ground	675	7110	/	/	/	/
IN062	GE B25K Bar	MA + 12.4% CF	1 µm	510	7110	9180	9440	17000	3850
IN063	GE B25K Bar	MA + 12.4% CF	1 µm	510	7110	9180	9440	17000	3850

IN064■	GE B25K Bar	MA + 12.4% CF	Ground	510	7110	/	/	/	/
IN065	Valinox CRDM	TT + 11.7% CF	1 μm	365	7110	/	/	/	/
IN066	Valinox CRDM	TT + 11.7% CF	1 μm	379	7110	9180	9440	17000	3850
IN067■	Valinox CRDM	TT + 11.7% CF	Ground	365	7110	/	/	/	/
IN172	Allvac Plate	MA + 31%CF	1 μm	623	/	9180	9440	17000	3850
IN173	Allvac Plate	MA + 31%CF	1 μm	623	/	9180	9440	17000	3850
IN174	Valinox CRDM	SA + 31%CR	1 μm	632	/	9180	9440	17000	3850
IN175	Valinox CRDM	SA + 31%CR	1 μm	632	/	9180	9440	17000	3850
IN176	Sumitomo CRDM	TT + 21%CF	1 μm	575	/	9180	9440	17000	3850
IN177	Valinox CRDM	TT + 21.9%CF	1 μm	510	/	9180	9440	17000	3850
IN178	Valinox CRDM	TT + 21.9%CF	1 μm	465	/	9180	9440	17000	3850
IN179■	Sumitomo CRDM	TT + 30.6%CF	1 μm	588 (90%YS)	/	9180	9440	17000	/
IN180	Sumitomo CRDM	TT + 30.6%CF	1 μm	575 (90%YS)	/	9180	9440	17000	3850
IN181	Valinox CRDM	TT + 31%CF	1 μm	580 (90%YS)	/	9180	9440	17000	3850
IN182	Valinox CRDM	TT + 31%CF	1 μm	575 (90%YS)	/	9180	9440	17000	3850
IN183	Sumitomo CRDM	TT + 12.7%CF	1 μm	405	/	9180	9440	17000	3850
IN184	Valinox CRDM	SA + 17%CR	1 μm	335	/	9180	9440	17000	3850
IN263	Ni-30Cr	SA + 21%CF	1 μm	488	/	/	9440	17000	3850
IN264	Ni-30Cr	SA + 21%CF	1 μm	502	/	/	9440	17000	3850
IN265	Ni-30Cr	SA + 21%CF	1 μm	488	/	/	9440	17000	3850
IN266	TK-VDM CRDM	TT + 32%CF	1 μm	603 (90%YS)	/	/	9440	17000	3850
IN267■	TK-VDM CRDM	TT + 32%CF	1 μm	668	/	/	9440	17000	3850
IN268	TK-VDM CRDM	TT + 32%CF	1 μm	603 (90%YS)	/	/	9440	17000	3850
IN269	Valinox RE243	SA + 31%CR	1 μm	655	/	/	9440	17000	3850
IN270	Valinox RE243	SA + 31%CR	1 μm	655	/	/	9440	17000	3850
IN271	Doosan CRDM	TT + 21%CF	1 μm	530	/	/	9440	17000	3850
IN272	Sumitomo CRDM	TT + 21%CF	1 μm	546	/	/	9440	17000	3850
IN294	Valinox CRDM	TT + 21.9%CF	1 μm	510	/	/	/	17000	3850
IN295	Valinox CRDM	TT + 21.9%CF	1 μm	505	/	/	/	17000	3850
IN296	Valinox CRDM	TT + 11.7%CF	1 μm	364	/	/	/	17000	3850
IN297	Sumitomo CRDM	TT + 12.7%CF	1 μm	380	/	/	/	17000	3850

† The applied stress is the yield stress of the specimens at the tested temperature (360°C) unless otherwise specified.

■ Specimens removed for cross-section examination. *Ongoing test as of August 2023.

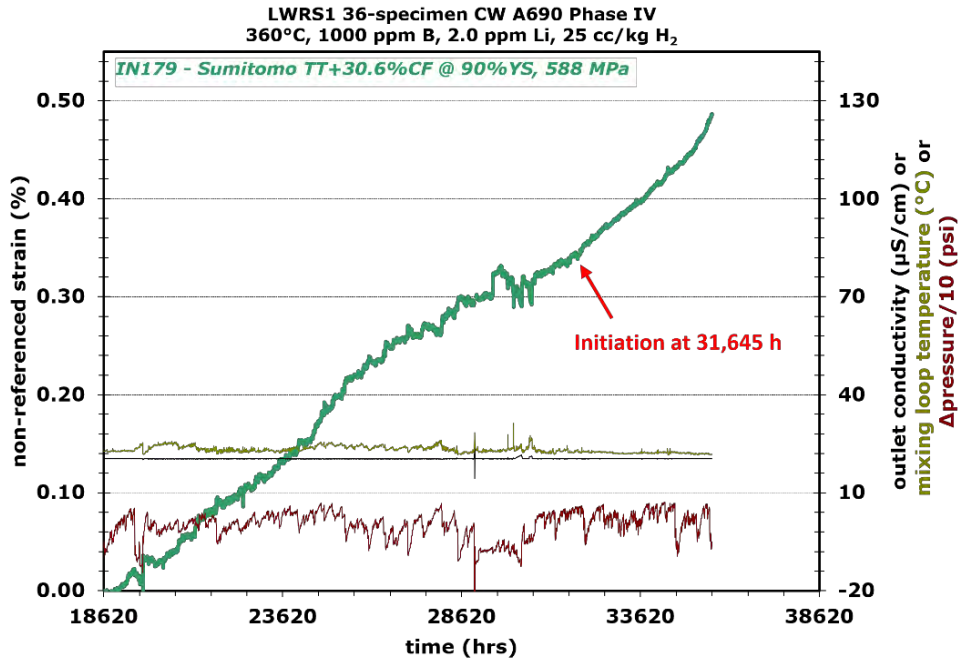


Figure 64. Non-referenced DCPD strain response during the Phase IV exposure, indicating macroscopic crack initiation in the Sumitomo CRDM TT+31%CF specimen IN179 tested at 0.9 YS initiated after 31,645 hours of exposure in 360 °C PWR primary water.

Figure 65 provides an overview of the non-referenced DCPD strain response during the Phase V exposure on all twelve specimens monitored in LWRS1. Only non-referenced DCPD strain rates were monitored for selected specimens in the LWRS1 test system due to restrictions on the number of wires that can be used in the autoclave. For each monitored specimen, there is usually at least one more replicate specimen tested in the same test system except IN030, for which the other two companion specimens were already removed at previous test interruptions. More detailed non-referenced DCPD strain response for each monitored specimen during this testing period can be viewed in Figures 66–69 following a decreasing order of their total exposure time in test. The non-referenced DCPD strain appears relatively steady for all specimens except for the TK-VDM plate TT+32%CF specimen IN267. It showed a gradual increase in strain rate after a total exposure time of 28,135 hours, suggesting macroscopic crack initiation had taken place in this specimen (Figures 65 and 68). This is not surprising, as many short surface-breaking IG cracks were already identified after Phase III exposure in this specimen and were associated with GB cavities at crack tips by focused ion beam (FIB) serial trenching [23]. In addition, Crack initiation was detected previously by DCPD in another TK-VDM specimen IN042 tested in the same condition after 31,988 hours of exposure [23], which is relatively close to the time that initiation was detected in IN267. The test in LWRS1 was stopped in July 2023 to remove this initiated specimen and has just been restarted on the remaining specimens.

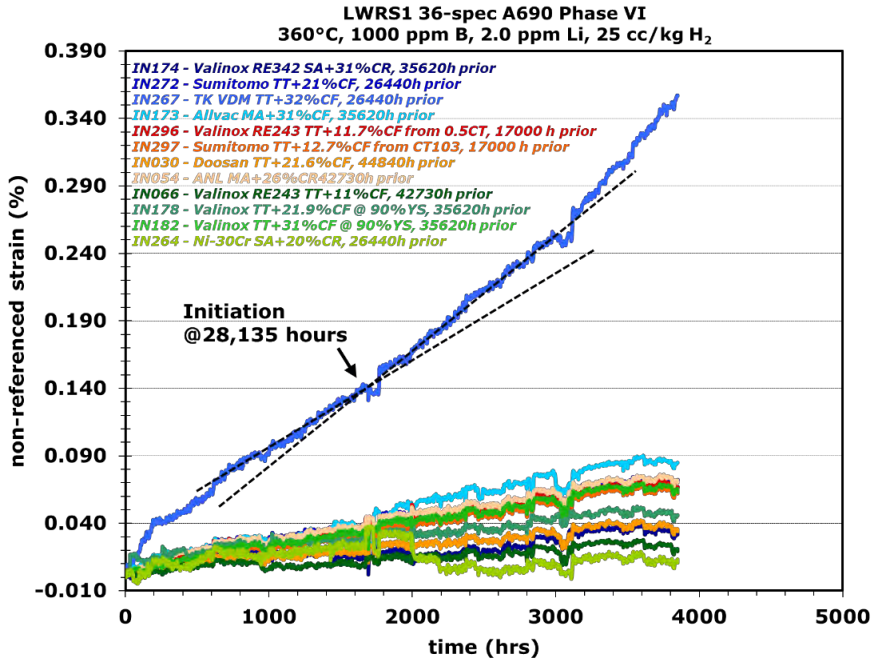


Figure 65. Overall non-referenced DCPD strain response during the Phase V exposure for all the specimens monitored in the LWRS1 (36-specimen) SCC initiation test system in 360 °C PWR primary water. The test is ongoing as of August 2023. Specimens are all being tested at materials yield stress unless otherwise specified.

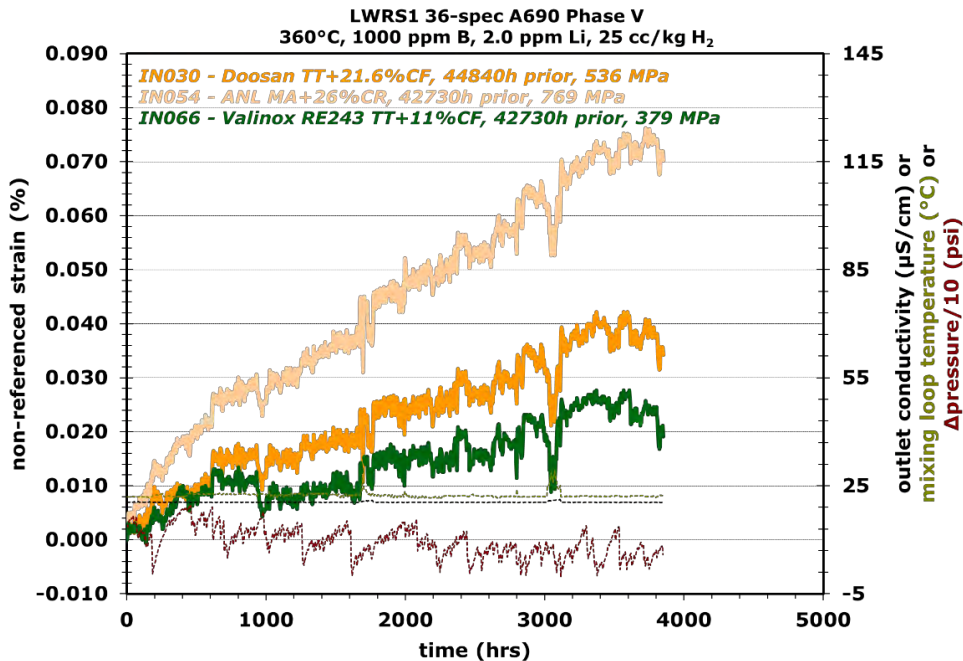


Figure 66. Non-referenced DCPD strain response during the Phase V exposure for the specimens introduced in Phase I and monitored in the LWRS1 (36-specimen) test system in 360 °C PWR primary water. The test is ongoing as of August 2023.

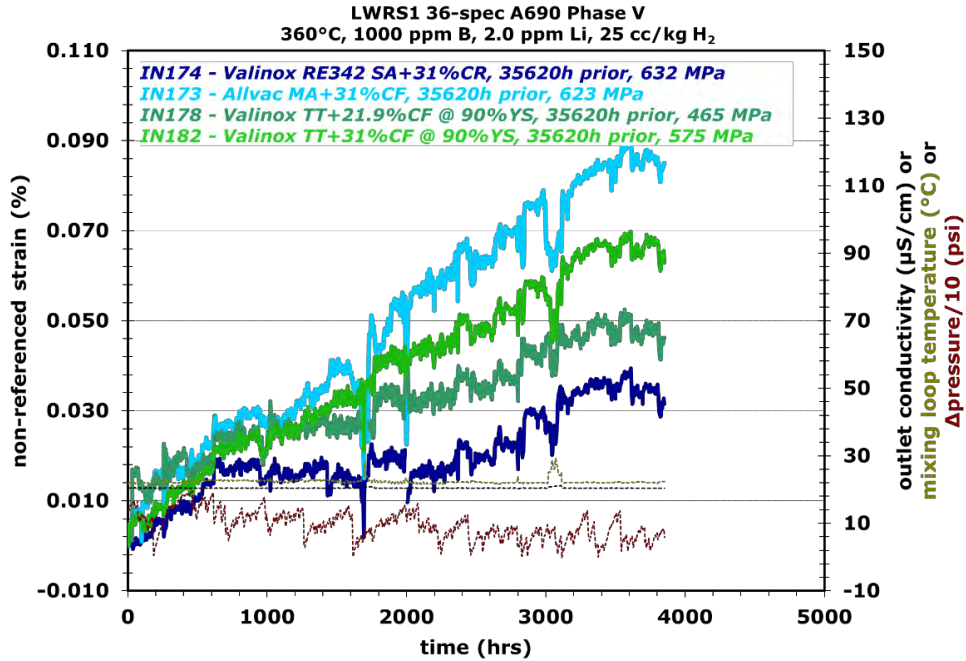


Figure 67. Non-referenced DCPD strain response during the Phase V exposure for the specimens introduced in Phase II and monitored in the LWRS1 (36-specimen) test system in 360 °C PWR primary water. The test is ongoing as of August 2023.

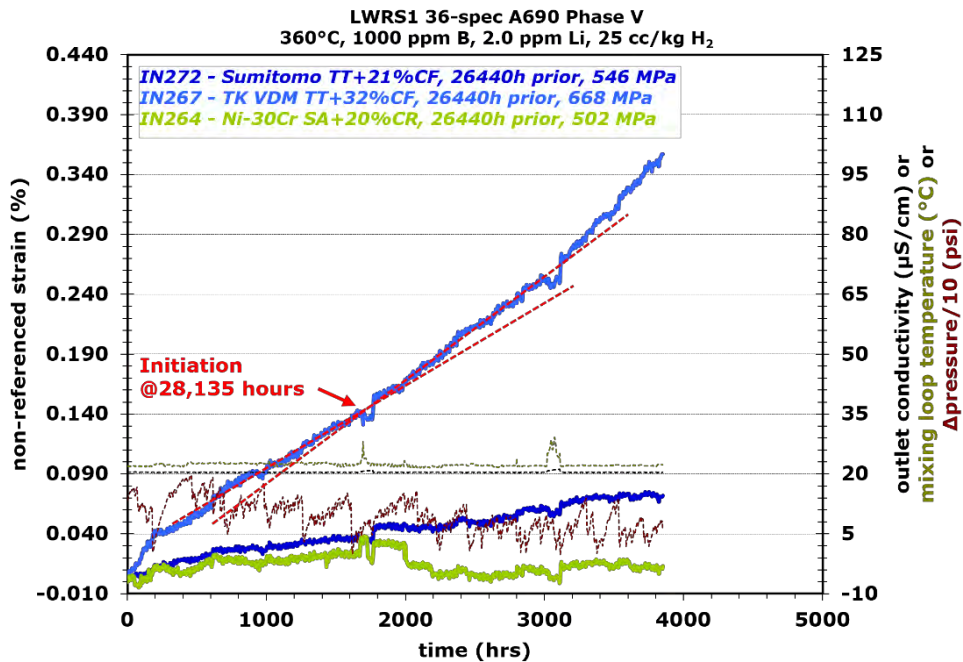


Figure 68. Non-referenced DCPD strain response during the Phase V exposure for the specimens introduced in Phase III and monitored in the LWRS1 (36-specimen) test system in 360 °C PWR primary water. The test is ongoing as of August 2023.

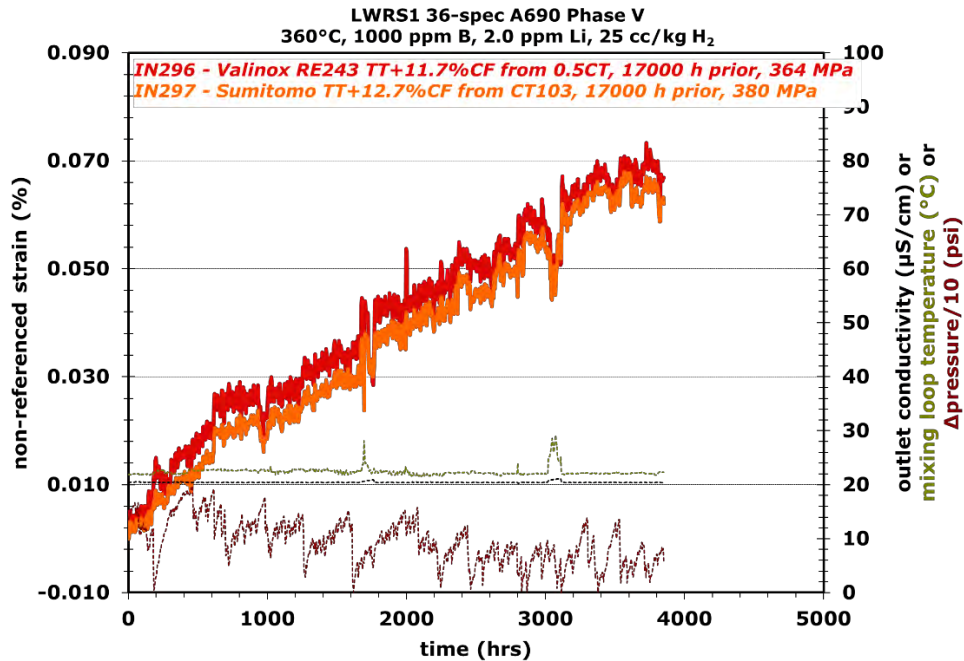


Figure 69. Non-referenced DCPD strain response during the Phase V exposure for the specimens introduced in Phase IV and monitored in the LWRS1 (36-specimen) test system in 360 °C PWR primary water. The test is ongoing as of August 2023.

In addition, six specimens were tested in LWRS2, and their non-reference and referenced DCPD strain responses during Phase V exposure are shown in Figures 70 and 71, respectively. The estimated strain rates for each specimen are also marked in the figures. As discussed previously, the non-referenced strain rate reflects the combined response of cracking, creep, and resistivity evolution over time for each specimen. In comparison, the referenced strain response is believed to only represent the contribution of cracking and creep, while the impact of resistivity evolution is removed via the concurrent voltage monitoring of a reference shoulder section on each specimen (Section 2.2.1) [6]. Since rapid cracking is unlikely to occur at the current stage in the materials condition being evaluated, the referenced strain rates are considered a reasonable approximation of the actual creep strain rates for these six specimens. Plotting these values as a function of their applied stress revealed that creep strain rates in these specimens increased linearly with applied stress, regardless of the heat or cold work condition (Figure 72(a)). The contribution of resistivity evolution to specimen strain rate was also calculated by subtracting the referenced strain rate from the non-referenced strain rate for each specimen, and the results are presented in Figure 72(b). It is interesting to note that resistivity evolution has a larger contribution than creep to specimens' non-referenced strain response but no clear dependence on applied stress. Nevertheless, the absolute values remain low and similar to those previously estimated during Phase IV exposure [23]. These data suggest resistivity evolution had become steady in these long-term tested specimens.

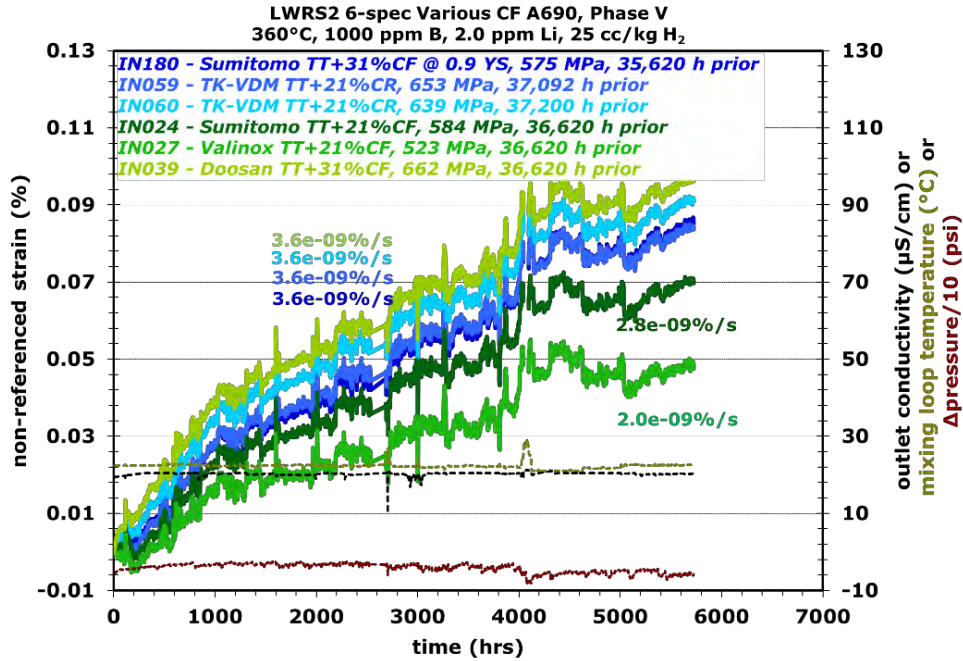


Figure 70. Overall non-referenced DCPD strain response during the Phase V exposure for all the specimens monitored in the LWR2 (6-specimen) SCC initiation test system in 360 °C PWR primary water. The test is ongoing as of August 2023.

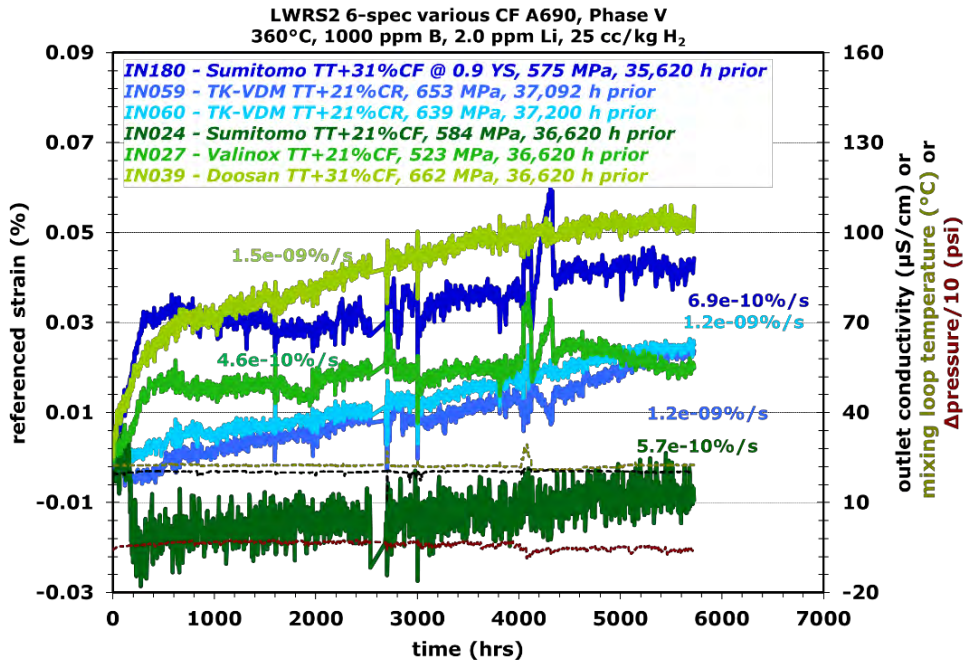


Figure 71. Overall referenced DCPD strain response during the Phase V exposure for all the specimens monitored in the LWR2 (6-specimen) SCC initiation test system in 360 °C PWR primary water. The test is ongoing as of August 2023.

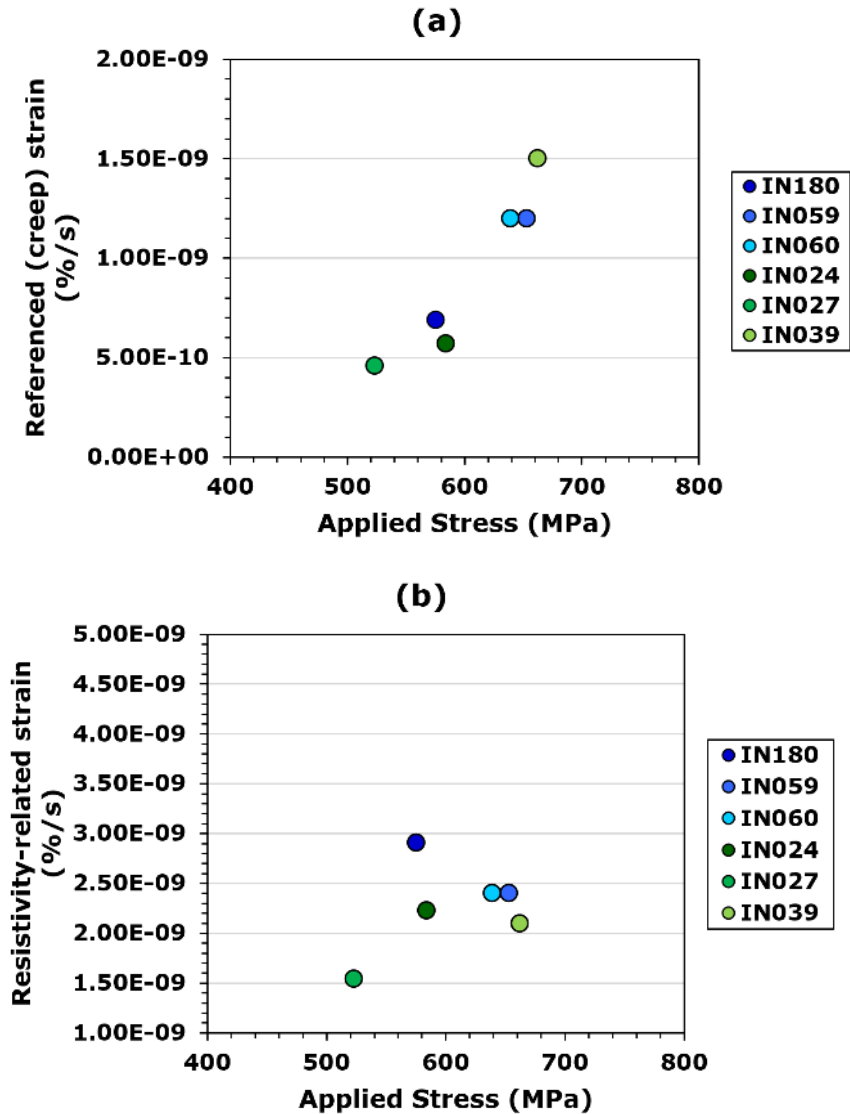


Figure 72. (a) Creep strain rates and (b) resistivity evolution as a function of applied stress of the six specimens tested in LWRS2. The strain rates were calculated based on their DCPD response up to ~5830 hours of exposure during Phase V. The test is ongoing as of August 2023.

3.3.2 Characterization of Precursor Damage and Crack Evolution in Cold Worked Alloy 690

As mentioned above, all specimens were removed after Phase IV testing for detailed characterizations. These characterizations focused on non-destructive examinations of the gauge surface of the specimens, starting with documenting the entire gauge surface of each sample using a JEOL 7600 scanning electron microscope. Four fiducial scribe marks (90° to one another) were made at the button ends of each specimen to keep track of the specimen orientation. Each of the four orientations was then mapped using high-kV BSE montage imaging so that features covered by thin surface oxides could be revealed. However, after Phase II exposure, a layer of densely packed spinel oxides was found on the surface of all highly polished specimens due to extended exposure in high-temperature water, making it challenging to resolve GB damage features even under high-kV conditions. As a solution, a non-

aggressive chemical method was developed to remove the excessive oxide layer with little impact to the surface below [19]. It turned out that this method was effective, and specimens that received oxide stripping at the Phase II test interruption did not need to be treated after Phase IV for detailed surface examination.

After the BSE montage was acquired, the images of the four rotations on each specimen were stitched together in Photoshop and carefully reviewed for IG damage features. Such damage usually manifests as a continuous dark delineation on GB segments, and the shade of darkness varies depending on the degree of IG oxidation or cracking. To get an idea of how these features look below the surface and how deep they are, some specimens were examined again in an FEI Quanta field-emission-gun, dual-beam FIB/SEM system at a specific rotation containing the feature of interest. Shallow trenches (usually less than 5 μm deep, with a maximum depth of 10 μm) intersecting the identified features were created, and the cross-section morphology right beneath the surface was documented. When there was an interest in examining the sub-surface damage evolution or the frequency of GB cavities, serial milling was often employed, creating trenches along selected features for a few micrometers, either at the center or from one end. Depending on the length of the trench, sub-surface morphology on 20 to 100 slices was commonly recorded to assess precursor damage distribution.

While most specimens did not exhibit identifiable IG damage on the gauge surface, the evolution of precursor damage was observed in several specimens, and notably, surface-breaking IG cracks were found in lower CW Alloy 690TT specimens for the first time. In the following sections, key characterization results will be presented in decreasing order of cold work.

3.3.2.1 Precursor Damage Evolution in Highly CW Alloy 690 Materials

Table 14 summarizes the first time short IG precursor cracks were observed in the highly CW Alloy 690 materials, along with their loading condition, starting GB microstructure, and distribution of pre-existing defects produced during cold working. As mentioned earlier, examinations at previous test interruptions have demonstrated GB cavities induced by creep being the dominating mechanism driving macroscopic crack initiation in these specimens, and their effect heavily depends on the starting GB microstructure, cold work level, and applied stress. The TT+31%CF Sumitomo and Valinox CRDM materials featuring a semi-continuous distribution of GB carbides and tested at 100% YS have proven to be the most susceptible to this cracking mechanism, with short IG cracks observed on the gauge surface within one year of exposure, followed by DCPD-detected crack initiation within 1.5–2.5 years [19, 20]. To provide context, an example from earlier observations performed on a TT+31%CF Valinox CRDM specimen IN037 is summarized in Figure 73. DCPD detected SCC initiation in this specimen after 1.5 years of exposure. Figure 73 presents the post-test gauge cross-section of IN037 after removing it from the test upon DCPD detection of crack initiation. A high density of GB cavities was observed throughout the entire thickness of the gauge, many aggregated at close distances, as highlighted in yellow in Figure 73a. A closer look in the gauge region revealed that at certain sites, neighboring GB cavities had become connected through cracked GB ligaments, forming internal IG cracks up to a few hundred micrometers in length (Figure 73b). The size of the cracks is consistent with the DCPD detectability of macroscopic cracks reported previously [5]. In addition, careful examination performed along the entire near-surface region of the gauge cross-section did not reveal any GB cavity aggregations protruding into the grinding-induced surface nano-crystalline damage layer (Figure 73c). These observations suggest that the upturn in the DCPD strain rate observed in the TT+31% CF Valinox CRDM specimen IN037 was not due to the growth of SCC crack from the gauge surface but the reduction in cross-sectional area induced by the rapid growth of internal IG cracks formed by coalescence of creep induced GB cavities.

Table 14. Summary of the GB microstructure, pre-existing damage, and IG precursor damage status for all the Alloy 690 materials tested in highly cold worked conditions. Cells highlighted in orange in the last column are new observations made after Phase IV exposure.

Material	Applied Stress (MPa)	AR GB Carbide Microstructure		Density of Cold Work Induced GB Damage		Time of short IG crack nucleation
		Size	Spacing	IG Voids	Cracked GB Carbides	
Valinox TT+31%CF	678 (1.0 YS)	50–200 nm	~100 nm	Low-Moderate	Low	Yes (<1 yr)
Sumitomo TT+31%CF	670 (1.0 YS)	50–200 nm	~100 nm	Low-Moderate	Low	Yes (<1 yr)
TK-VDM TT+32%CF	670 (1.0 YS)	50–500 nm	~0.2–0.5 μm	Low-Moderate	Low	Yes (btw 1–2 yrs)
Allvac TT+31%CF	623 (1.0 YS)	50–500 nm	~0.1–1 μm	Low-Moderate	Low-Moderate	Yes (btw 2.1–3.4 yrs)
Valinox TT+31%CF	588 (0.9 YS)	50–200 nm	~100 nm	Low-Moderate	Low	Yes (btw 3.4–4.2 yr), Cavities ahead of crack tip
Sumitomo TT+31%CF	580 (0.9 YS)	50–200 nm	~100 nm	Low-Moderate	Low	Yes (btw 2.1–3.4 yr), Cavities ahead of crack tip, DCPD detected initiation after 3.6 yrs
Doosan TT+32%CF	662 (1.0 YS)	1–5 μm	~0.5–2 μm	Low-Moderate	Moderate	Yes (btw 3.2–4.2 yrs), no/minor cavity increase
ANL MA+26%CR	(1.0 YS)					No (by 5.3 yrs)
Valinox SA+31%CF	(1.0 YS)					No (by 4.5 yrs)

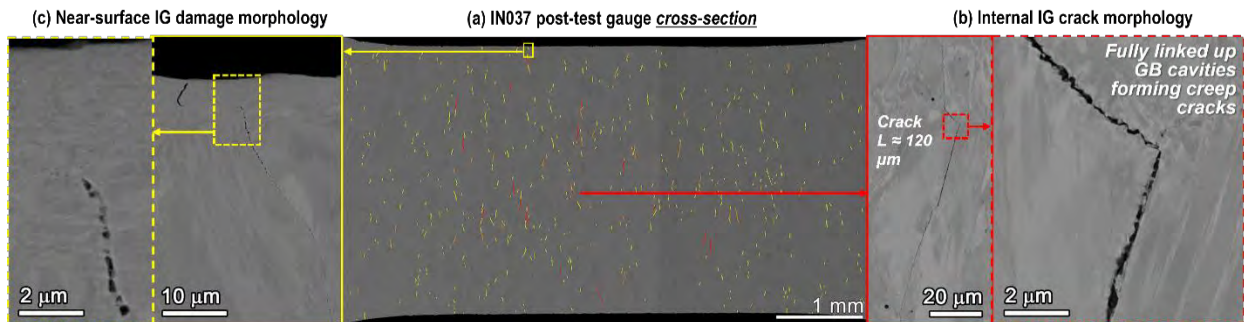


Figure 73. SEM-BSE images of (a) the gauge cross-section of the TT+31% CF Valinox CRDM specimen IN037 removed after DCPD detected crack initiation. Aggregations of GB cavities are highlighted in yellow and continuous IG cracks in red, with higher magnification IG damage examples (b) inside the specimen and (c) near the surface.

As shown in Figure 64, Phase IV exposure witnessed the first DCPD detection of crack initiation in a TT+31%CF Sumitomo CRDM specimen IN179 tested at 90% YS after ~3.6 years of exposure. The highly polished surface enabled IG damage documentation on this specimen at test interruptions (Figure 74). Only discontinuous IG damage was seen after 2.1 years of exposure (Figure 74a), while short surface-breaking IG cracks started to show up after 3.4 years (Figure 74b), but still very few in density. By the time the specimen was removed from the test after an additional 0.5-year exposure in high-temperature water following the DCPD-detected crack initiation, a significant increase in IG crack density was observed, along with obvious growth in length for the cracks that were already observed during the

previous test interruption (Figure 75). While this specimen has not been cross-sectioned for further examinations after being removed from the test yet, non-destructive FIB trenching performed after 3.4 years at multiple sites containing IG cracks consistently showed an increase in GB cavity density ahead of the crack tips, with an example shown in Figure 74b. As a result, it is reasonable to attribute the cause of initiation in this specimen to creep-induced GB cavity formation and growth.

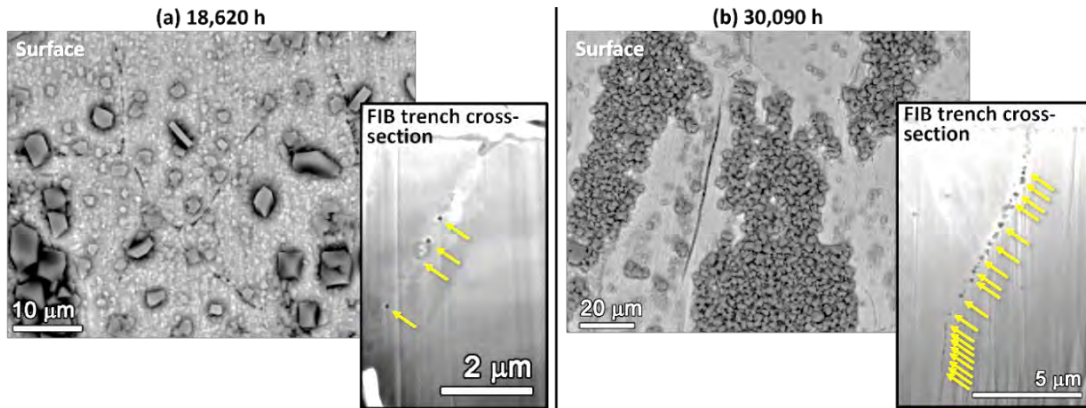


Figure 74. SEM-BSE images of the representative surface and cross-section morphology of IG damage found in the TT+31% CF Sumitomo CRDM specimen IN179 after 2.1 (left) and 3.4 (right) years of exposure in 360°C simulated PWR primary water. GB cavities are highlighted in yellow in the FIB trench cross-sections.

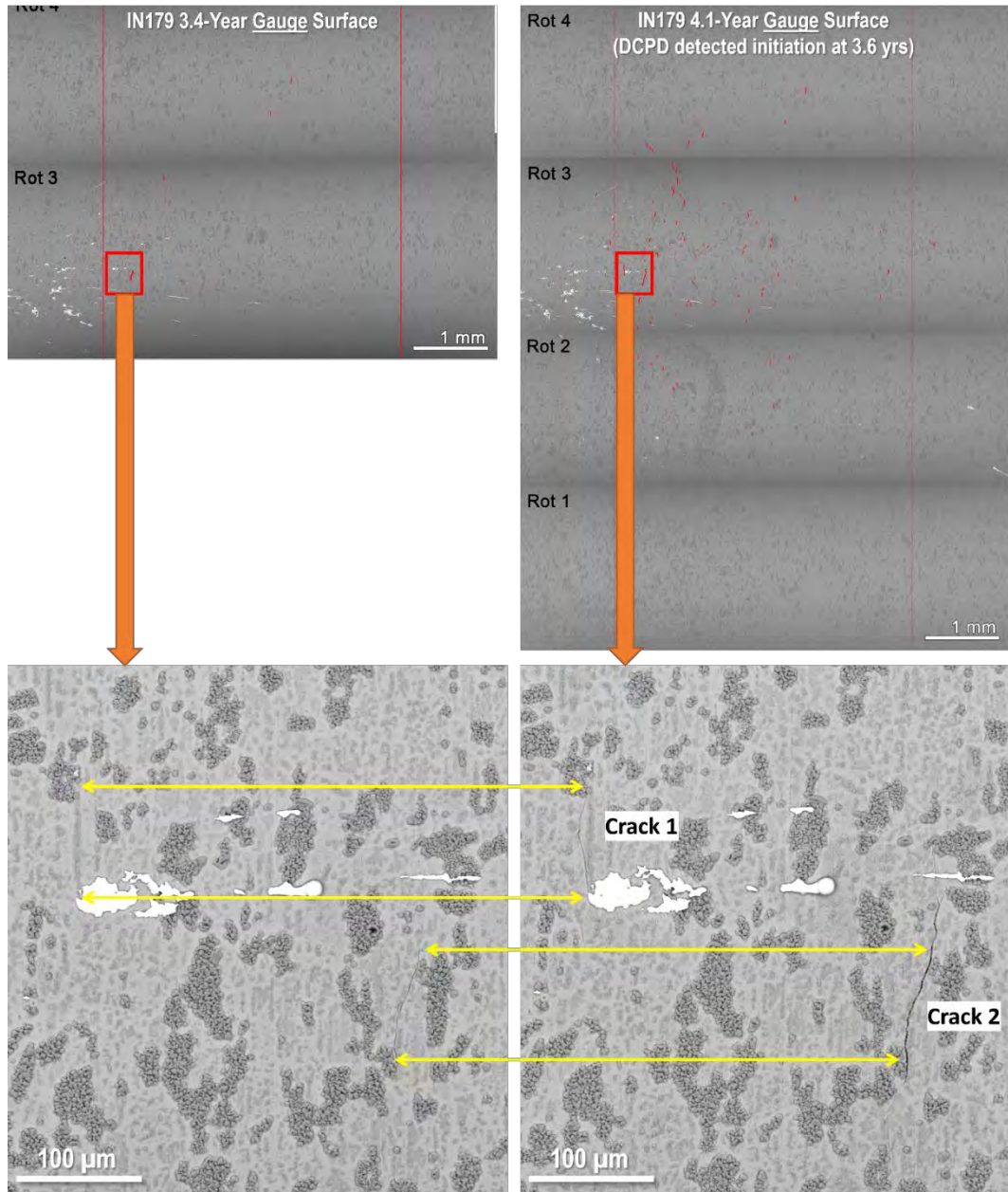


Figure 75. SEM-BSE montage images of the evolution of surface-breaking IG cracks (highlighted in red) found on the gauge surface of the TT+31% CF Sumitomo CRDM specimen IN179 before (left) and after (right) DCPD detection of crack initiation.

Interestingly, the TT+31% CF Doosan specimen loaded at a similar YS as the TT+31%CF Sumitomo and Valinox CRDM materials did not see DCPD detection of crack initiation after >2X longer exposure time. The SEM-BSE gauge surface montage taken at the most recent test interruption after 4.2 years of exposure revealed some short IG cracks, as highlighted in red in the gauge surface montage image in Figure 76. These cracks generally extend no more than 100 μm in surface length, and an example is also shown in Figure 76 with its morphology evolution over time since Phase II. No obvious surface damage was seen after 2.1 years. After 3.2 years, a slightly darker contrast appeared along a certain portion of a GB, indicative of minor IG oxidation damage. The contrast became sharper after 4.2 years without any change in length, suggesting a slow enhancement of the IG damage. Serial FIB milling was performed at

one end of this feature in the region marked in Figure 76 after 4.2 years of exposure, and the result is shown in Figure 77. The images taken at FIB trench cross-sections during serial milling suggest that the IG damage feature observed on the surface is associated with a crack below the surface. However, the crack remained shallow ($\leq 4 \mu\text{m}$) after trenching up to a quarter of its surface length, with thick penetrative oxidation along the crack walls throughout the entire serial milling process in the cross-sections. In addition, IG voids were only observed sporadically ahead of this crack with size and morphology similar to those cold work-induced defects documented before the test (Figure 61). No series of GB cavity aggregation like those observed in the TT+31%CF Sumitomo and Valinox CRDM specimens were found in this material. All these observations indicate that the IG damage was growing very slowly in this Doosan CRDM specimen, following mechanisms pertinent to the classical "SCC" notion instead of through creep-induced GB cavity evolution.

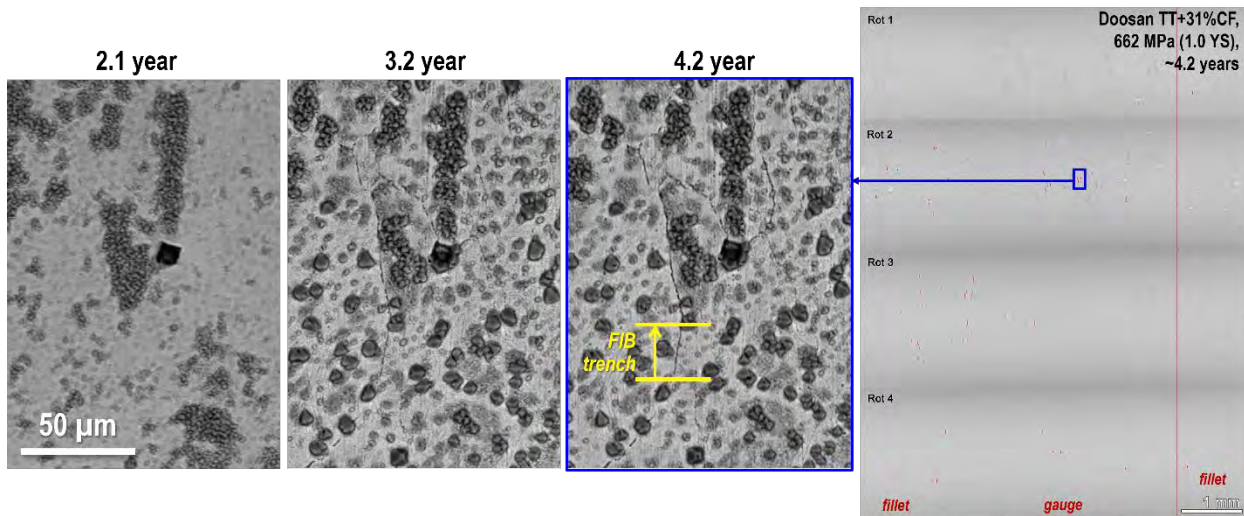


Figure 76. SEM-BSE montage images of the IG cracks (marked in red) observed on the TT+31% CF Doosan CRDM specimen IN039 after 4.2 years of exposure in 360°C simulated PWR primary water (right). The surface morphology evolution of the IG crack found after 4.2 years at the marked site is also presented (left).

FIB serial trenching sequence (selected slices)

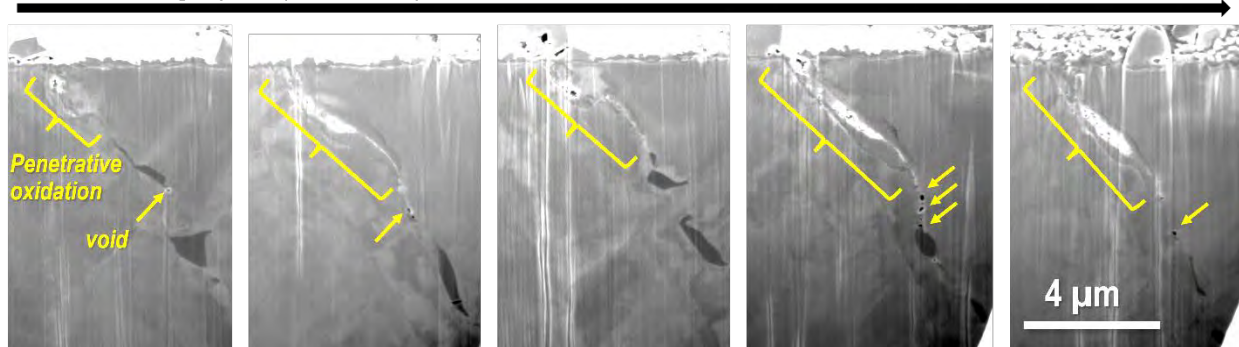


Figure 77. Low-kV FIB-SE images taken during FIB serial milling on the IG crack highlighted in Figure 76 in the TT+31% CF Doosan CRDM specimen IN039 after 4.2 years of exposure at 100% yield stress in 360°C simulated PWR primary water.

To better evaluate the role of GB carbide on GB cavity evolution in Alloy 690, an SA+31%CF variant from the Valinox CRDM heat was added to test since Phase II. This material condition was produced by solution annealing the as-received TT material at 1100 °C for 1 hour followed by water

quench, resulting in a complete removal of carbides from GBs. No obvious cold work-induced IG damage was identified before the test in this material. Upon completion of the Phase IV exposure, the two SA+31%CF specimens reached a total of 4.1 years of testing at 100% yield stress. SEM examination did not find any surface-breaking IG cracks in these two samples, but a faint dark delineation was observed along many HAGBs, with an example shown in Figure 78(a). FIB serial milling was performed on a few sections of such HAGBs. Figure 79(b) shows that only very limited IG oxidation, no more than 500 nm, was revealed in all slices, often followed by a bright bulge at the oxide tip. Previous studies have shown that this is a Cr-depleted zone formed by diffusion-induced grain boundary migration (DIGM), a common phenomenon associated with high-Cr Ni-base alloys exposed to high-temperature water [24].

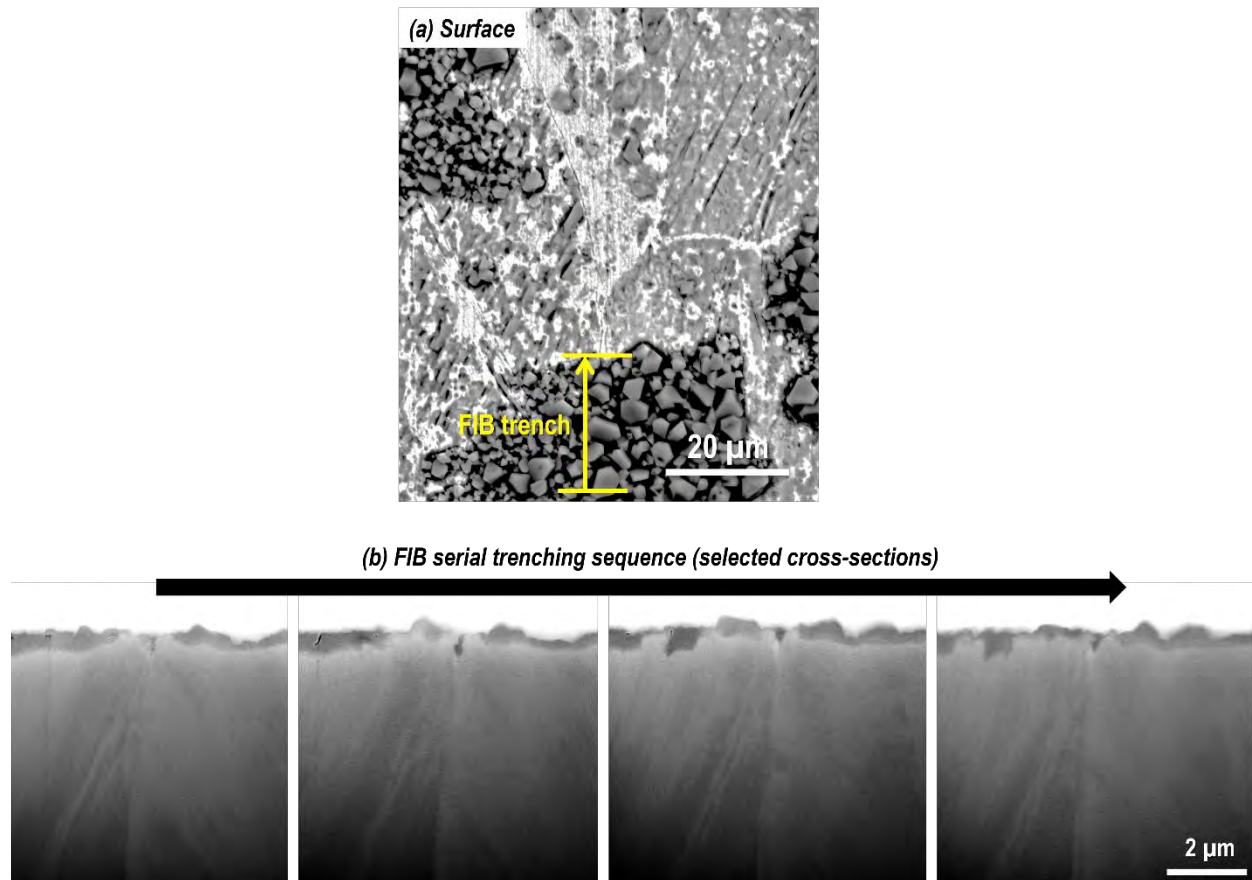


Figure 78. (a) SEM-BSE image of representative surface morphology of the HAGBs in the SA+31%CF Valinox CRDM specimen IN175 after 4.1 years of exposure at 100% yield stress in 360°C simulated PWR primary water. (b) Low-kV FIB-SE images taken during FIB serial milling on a segment of HAGB highlighted in (a).

3.3.2.2 Precursor Damage Evolution in Moderately CW Alloy 690 Materials

Table 15 summarizes the first time short IG precursor cracks were observed in the moderately CW Alloy 690 materials, along with their loading condition, starting GB microstructure, and distribution of pre-existing defects produced during cold working. The most important observation after Phase IV exposure is that surface-breaking IG cracks were identified for the first time in all three TT+21%CF Alloy 690 CRDM materials (Sumitomo, Valinox, and Doosan) tested at 100% YS. The crack morphology and its evolution in these three materials will be presented in detail below.

Table 15. Summary of the GB microstructure, pre-existing damage, and IG precursor damage status for all the Alloy 690 materials tested in moderately CW conditions. Cells highlighted in orange in the last column are new observations gained after Phase IV exposure.

Material	Yield/applied Stress (MPa)	AR GB Carbide Microstructure		Density of Cold Work Induced GB Damage		Time of short IG crack nucleation
		Size	Spacing	IG Voids	Cracked GB Carbides	
Valinox TT+21%CF	525 (1.0 YS)	50–200 nm	~100 nm	Very low	Very low	Yes (btw 3.2–4.2 yr)
Sumitomo TT+21%CF	590 (1.0 YS)	50–200 nm	~100 nm	Very low	Very low	Yes (btw 3.2–4.2 yr)
TK-VDM TT+21%CR	675 (1.0 YS)	50–500 nm	~0.2–0.5 μm	Very low	Very low	Yes (btw 2.1–2.9 yr)
Doosan TT+21.6%CF	555 (1.0 YS)	50–500 nm	~0.1–1 μm	Very low	Very low	Yes (btw 4–5.1 yrs)
GE B25K MA+18.3%CF	550 (1.0 YS)	1–5 μm	~0.5–2 μm	None	None	No (by 4.9 yrs)

The SEM-BSE montage image of the gauge section of the TT+21%CF Sumitomo CRDM specimen IN027 after 4.2 years of exposure is presented on the right side of Figure 79. A few surface-breaking short IG cracks were spotted (highlighted in red), plus a few more possible cracks indicated by a darker contrast on several GBs (highlighted in green). A zoom-in image of the largest IG crack found in this specimen is also shown, along with the morphology of the same site documented at previous test interruptions after 2.1 and 3.2 years of exposure. The 2.1-year image was taken after excessive surface oxides were stripped using the chemical immersion method mentioned earlier in this section, showing little indication of IG damage. At 3.2 years of exposure, a darker delineation showed up along a segment of an HAGB section highlighted by arrows, which turned much darker and deeper after 4.2 years, suggesting the formation of an IG crack.

Nevertheless, the crack still appeared tight, with a short surface length of ~80 μm . To better evaluate its sub-surface morphology, FIB serial milling started from slightly outside one end of the crack and trenched in for ~15 μm along the crack length. As shown in the video embedded in Figure 80(a), a ~2 μm deep aggregation of cavities showed up below the surface immediately after the serial milling began along the same GB where the crack formed. As the FIB milling approached one end of the open crack, the IG oxide gradually grew deeper from the surface, and aggregates of GB cavities were always present immediately ahead of the oxide tip and became longer and denser as the milling moved forward. By the time the FIB serial milling stopped shortly after passing one end of the crack, the oxidized portion of the crack reached ~3 μm , followed by a series of densely packed GB cavities that started to link up, extending for another ~5 μm along the same HAGB.

Meanwhile, FIB serial milling was also performed on a few randomly selected HAGBs that exhibited no obvious or possible IG cracks. One example is shown in the video in Figure 80(b). The IG oxidation remained very short, no more than 500 nm deep, throughout the entire serial milling sequence. The IG damage features below the surface closely resemble the pre-existing cold work damage without an obvious increase in size or density (Figure 62), suggesting limited evolution of GB cavities on this HAGB.

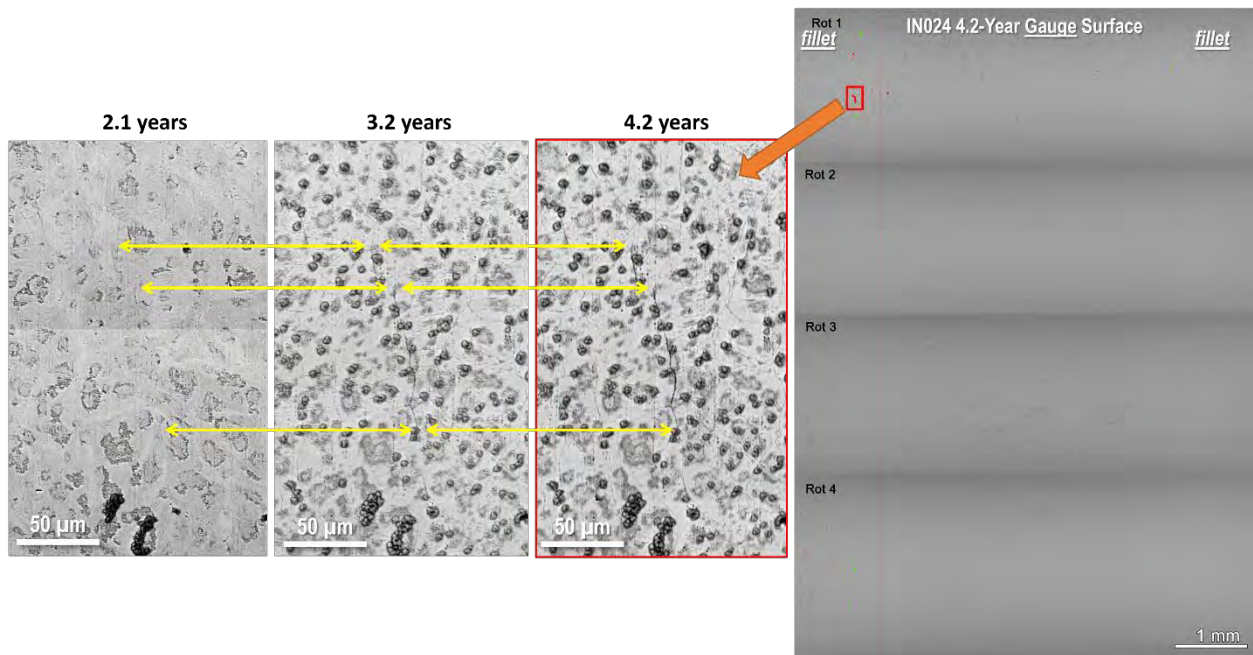


Figure 79. Distribution of surface-breaking IG cracks (marked in red) and possible cracks (marked in green) observed on the gauge surface of the TT+21% CF Sumitomo CRDM specimen IN024 tested at 100% YS after 4.2 years of exposure in 360°C simulated PWR primary water (upper right). Higher-magnification SEM-BSE images are also shown for the evolution of IG damage on a selected site from 2.1–4.2 years of exposure.

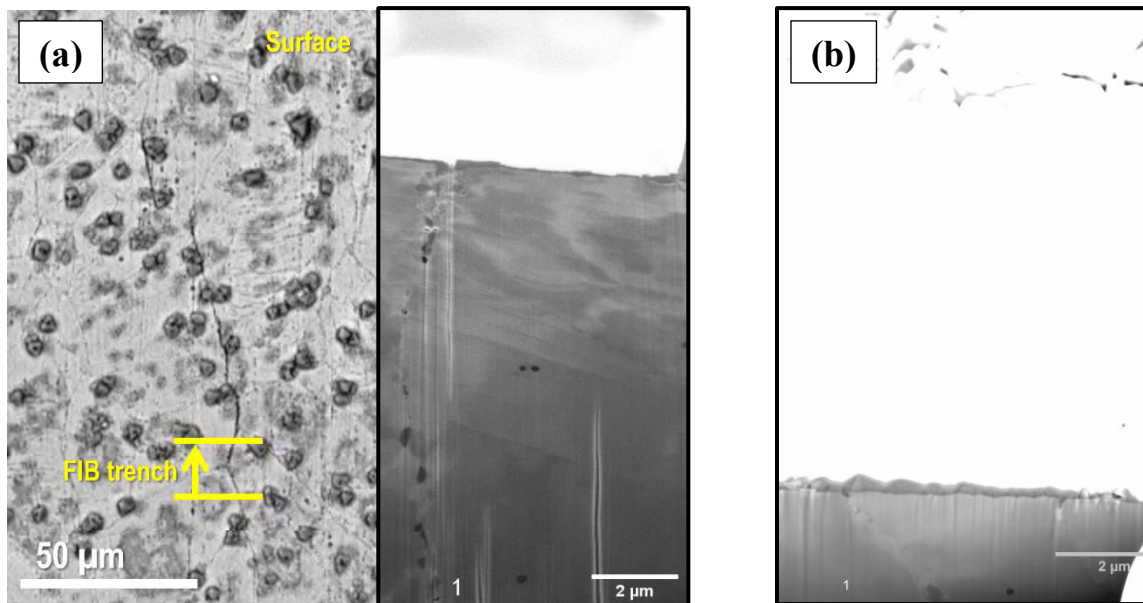


Figure 80. Low-kV FIB-SE images taken during FIB serial milling on (a) the IG crack identified in Site 1 in Figure 81 and (b) a random HAGB without surface-breaking crack in the gauge section of the 1 μm finish, TT+21%CF Sumitomo CRDM specimen IN024 tested at 100% YS after Phase IV (4.2 years) exposure in 360°C simulated PWR primary water.

A few surface-breaking IG cracks were also found for the first time in the TT+21%CF Valinox CRDM specimen IN027 after 4.2 years of exposure (Figure 81). The evolution of three such cracks from

2.1 to 4.2 years is also provided in this figure. Darker and wider contrast along segments of HAGB only became apparent after the most recent test interruption at 4.2 years, suggesting crack nucleation had occurred on the surface. The crack observed at Site 3 is particularly interesting, which represents the first IG crack that extended to two grains. It is also the longest IG crack in this specimen, showing a surface length of $\sim 130 \mu\text{m}$.

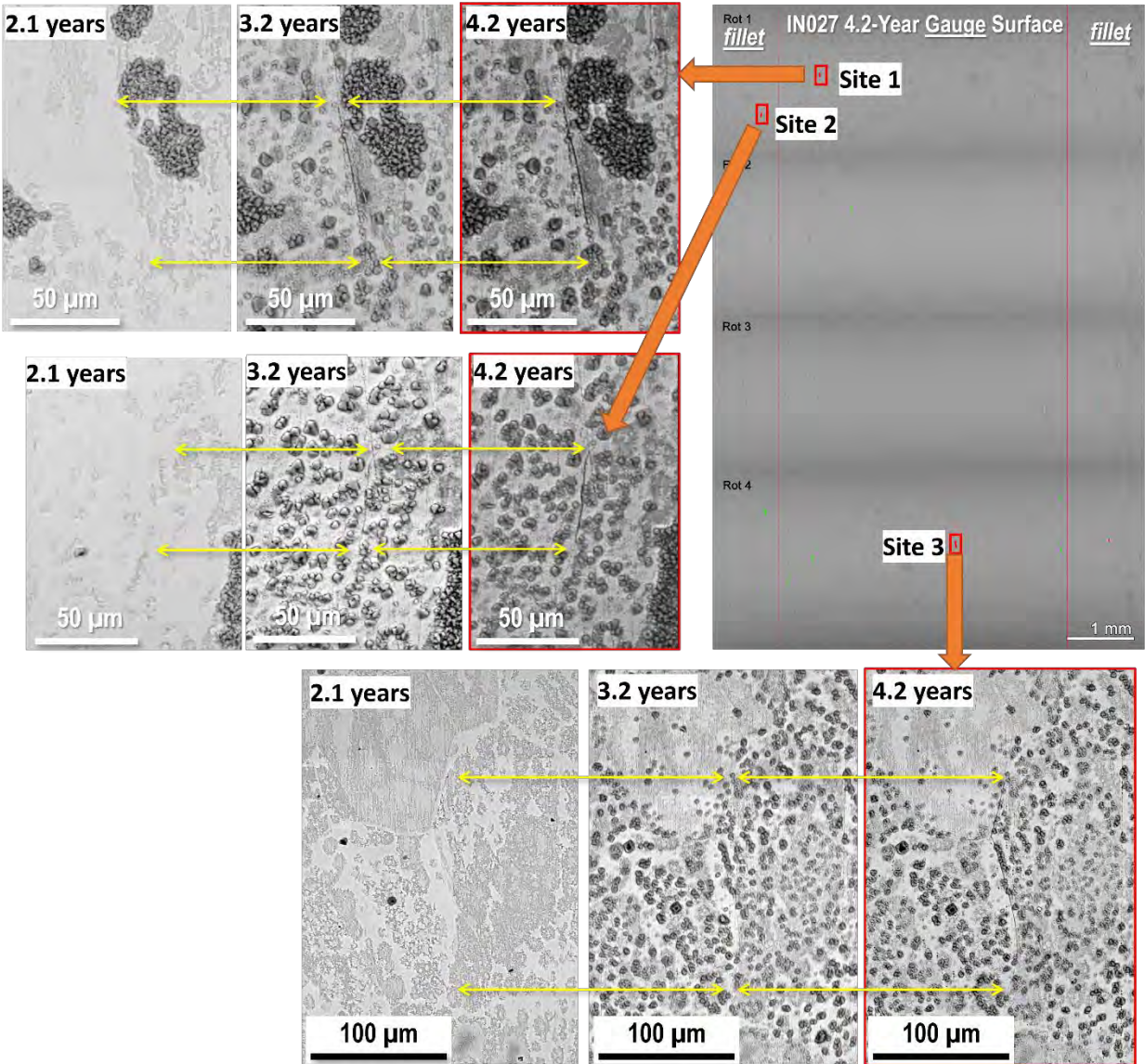


Figure 81. Distribution of surface-breaking IG cracks (marked in red) and possible cracks (marked in green) observed on the gauge surface of the TT+21% CF Valinox CRDM specimen IN027 tested at 100% YS after 4.2 years of exposure in 360°C simulated PWR primary water (upper right). Higher-magnification SEM-BSE images are also shown for the evolution of IG damage on three selected sites from 2.1–4.2 years of exposure.

Serial FIB milling was performed in this specimen after Phase III and IV exposure, with examples shown in Figures 82 and

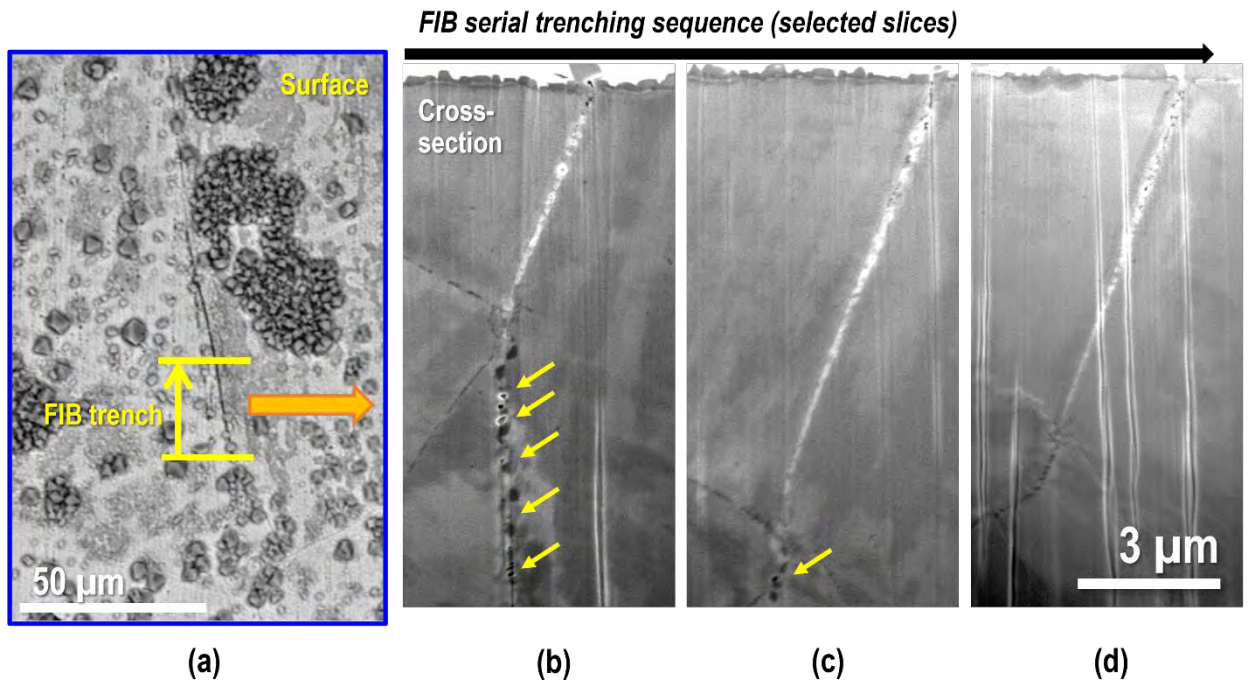


Figure 83, respectively. Since no obvious IG cracks were observed on the surface of this specimen after Phase III exposure, serial FIB milling was performed on a random HAGB. The IG oxidation remained within 500 nm from the surface, and no obvious growth in GB cavity density or size was observed. After Phase IV exposure, serial FIB milling was performed on the crack found at Site 1 in Figure 81, as the longest IG crack at Site 3 was preserved for future examinations. As shown in

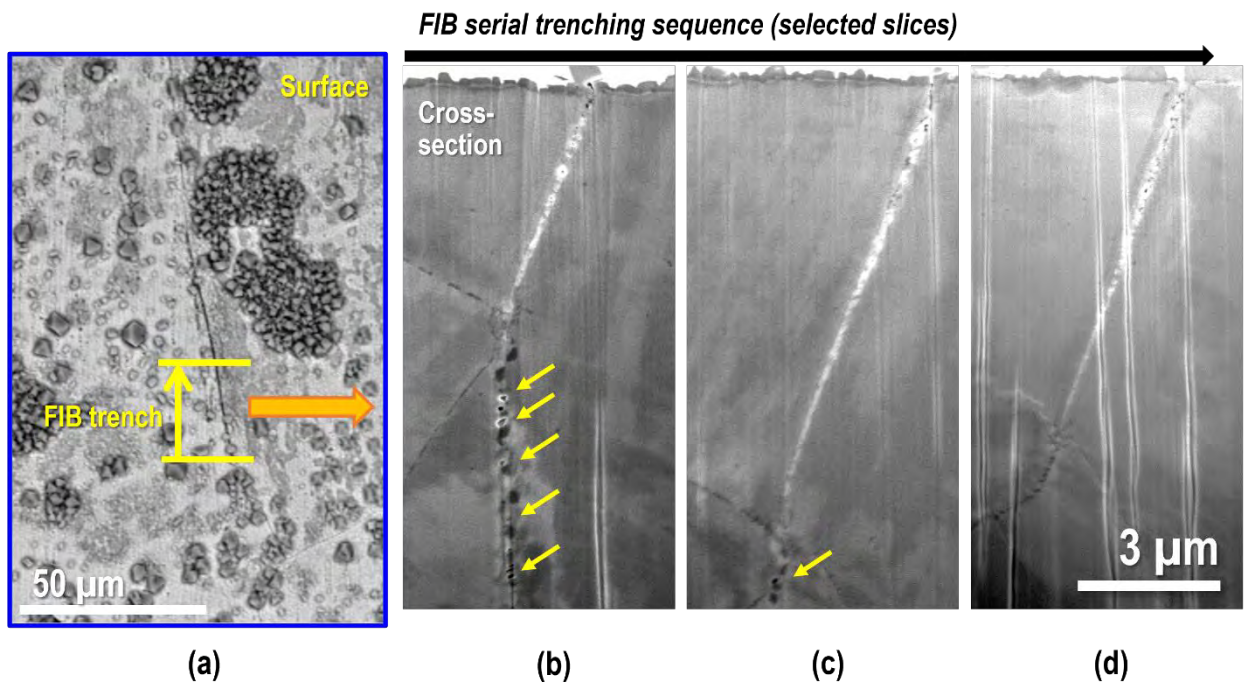


Figure 83, this IG crack was serially milled from one end up to its middle point, revealing an undulating crack depth and change in GB characteristics. IG cracking was present throughout the entire FIB milling process, initially followed by a high density of closely spaced GB cavities (

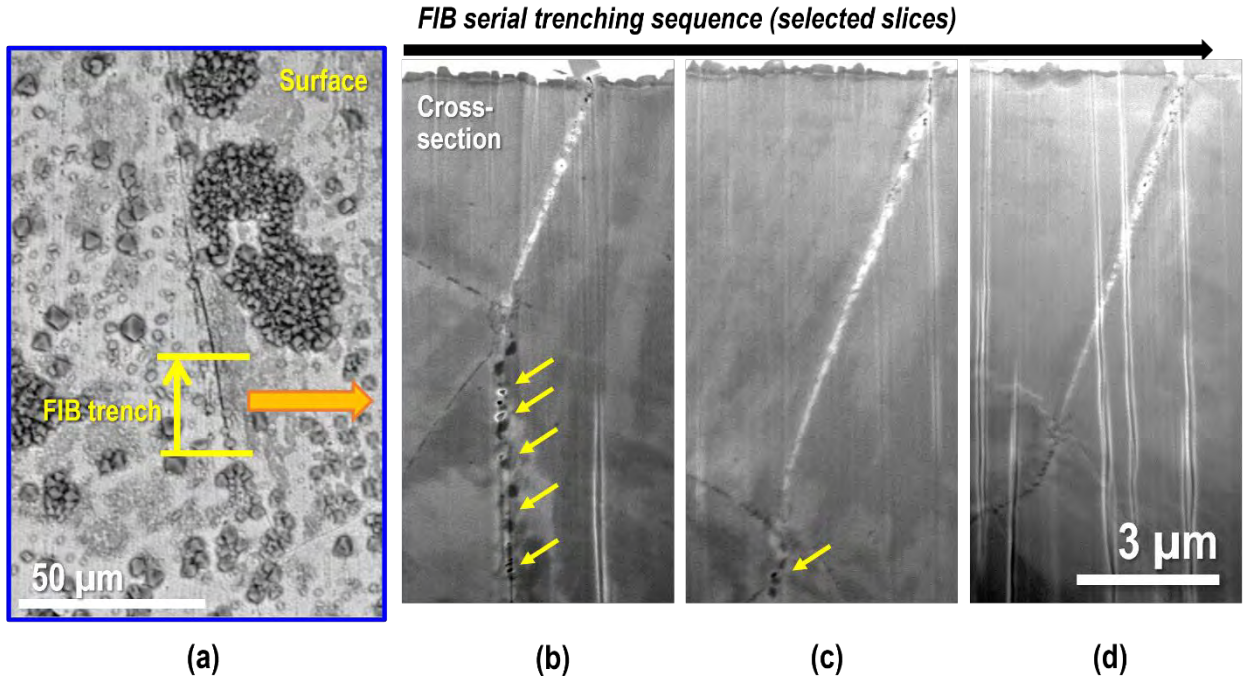


Figure 83b) that gradually diminished after the crack reached a maximum depth of $\sim 10 \mu\text{m}$ (

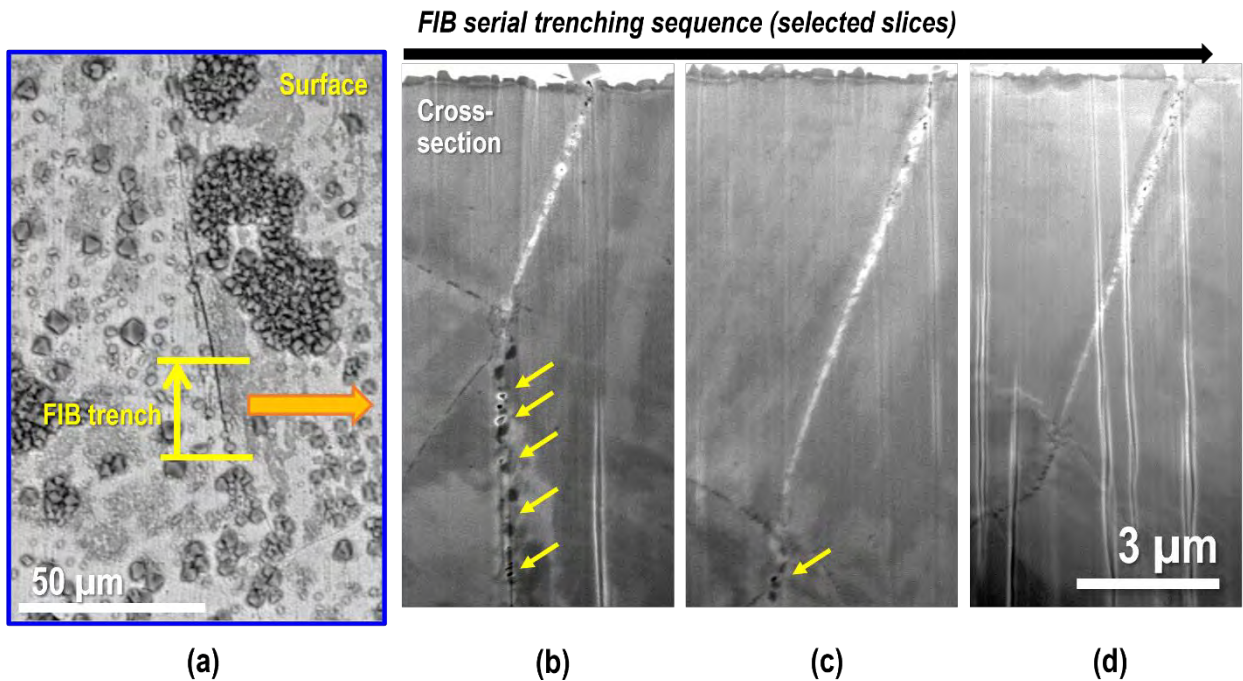


Figure 83c). Interestingly, the IG crack always ended at a triple point without extending into the next grain. There appeared to be a new GB joining the triple point from the lower right when the IG crack reached its maximum depth, after which the GB ahead of the crack changed its position abruptly (

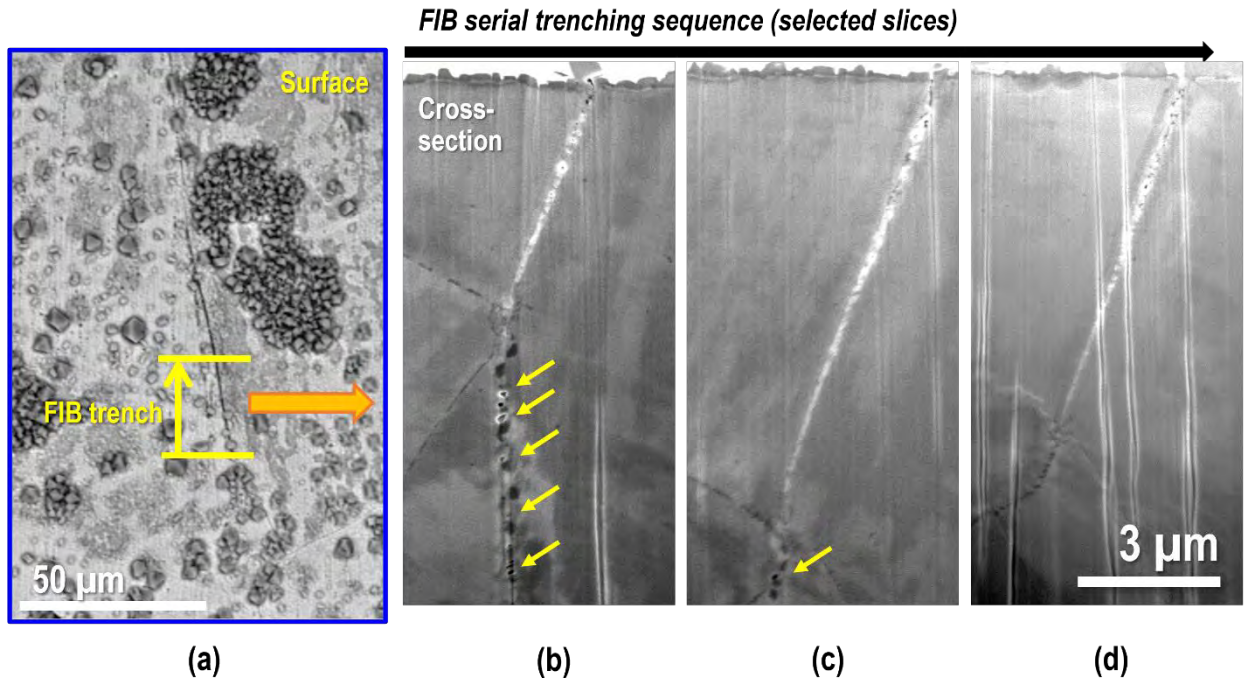


Figure 83d). These observations indicate that the GB below the crack embarked on a different grain at this moment, and the fact that it coincided with the disappearance of GB cavities suggests that grain orientation has a strong impact on the local susceptibility to cavity and IG crack formation. Similar to IN024, serial FIB milling was also performed on a random HAGB in IN027 after 4.2 years of exposure, and the sub-surface morphology was very similar to what was observed after 3.2 years (Figure 82).

SEM surface examination was also performed on the TT+21%CF Doosan CRDM specimen IN030 after Phase IV exposure. This specimen reached a one-year longer exposure time (i.e., 5.1 years) than IN024 and IN027 because it was tested in LWRS1 for Phase IV exposure while IN024 and IN027 were tested in LWRS2. As shown in Figure 84a, no surface-breaking IG cracks were observed in this specimen, but many HAGBs exhibit indications of possible IG cracks. Two such features were serially trenched in FIB, one with a darker and more continuous delineation along GBs (Figure 84b) and one with a lighter and semi-continuous delineation along GBs (Figure 84c). The serial milling revealed IG penetrative oxidation up to $\sim 4 \mu\text{m}$ deep in the first feature and $\sim 6 \mu\text{m}$ deep in the second feature. The IG penetrative oxidation was very thick in both cases, indicating that the oxidation process was slow. In addition, both features exhibited porosity below the surface, often with a size and shape comparable to the pre-existing voids or cracks produced by cold forging in these materials around or inside GB carbides. While these pre-existing defects may have served to open up IG penetrative oxide, no increase was observed in their size or density, and no GB cavity aggregation ahead of IG oxidation was observed in either case. These observations suggest that the IG cracks formed in this material are primarily SCC cracks.

Serial FIB milling

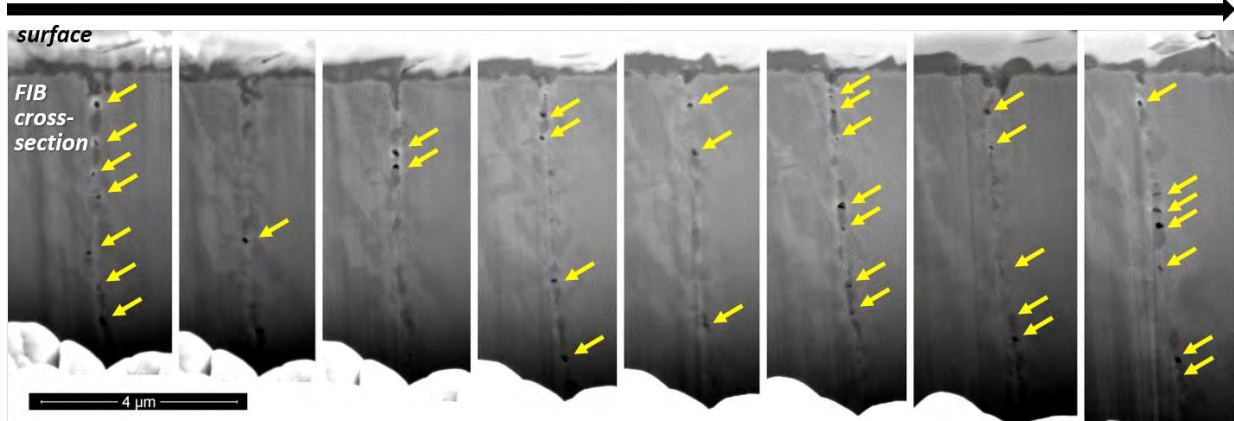


Figure 82. Low-kV FIB-SE images taken during FIB serial milling on a selected GB in the gauge section of the 1 μm finish, TT+21%CF Valinox CRDM specimen IN027 tested at 100% YS after Phase III (3.2 years) exposure in 360°C simulated PWR primary water. GB cavities revealed at the cross-sections are highlighted with arrows.

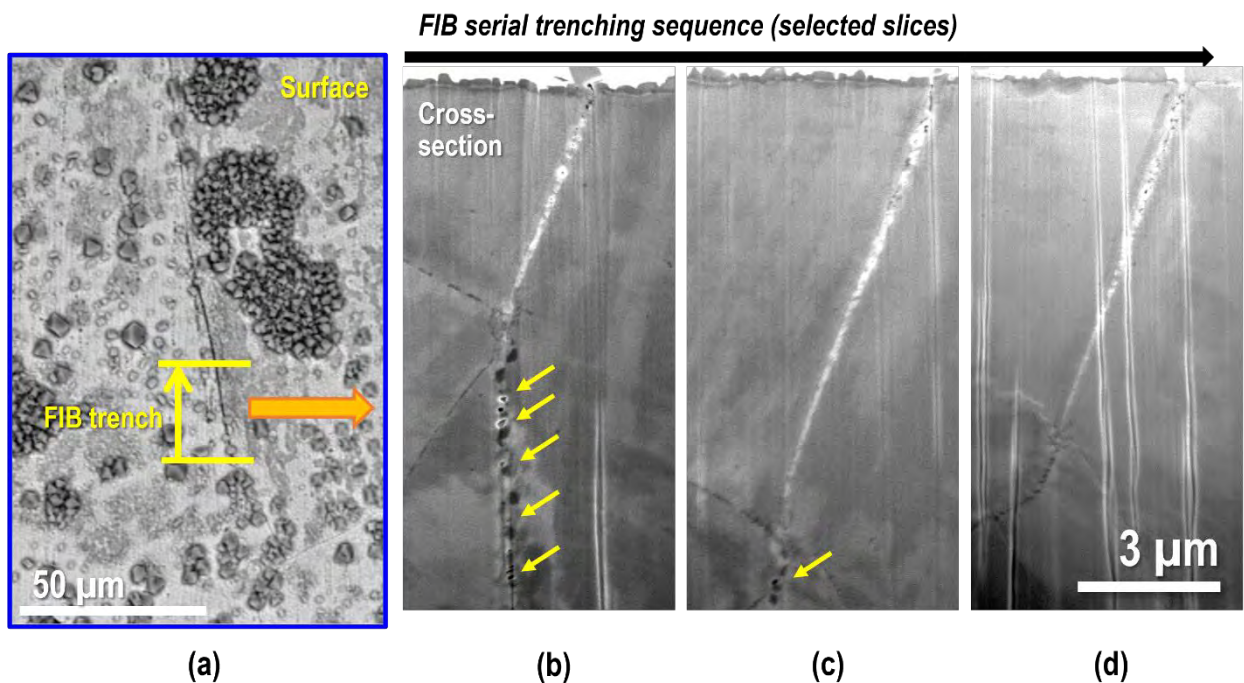


Figure 83. Selected low-kV FIB-SE images taken during FIB serial milling on the IG crack identified in Site 1 in Figure 81 in the gauge section of the TT+21%CF Valinox CRDM specimen IN027 tested at 100% YS after 4.2 years exposure in 360°C simulated PWR primary water. GB cavities revealed at the cross-sections are highlighted with arrows.

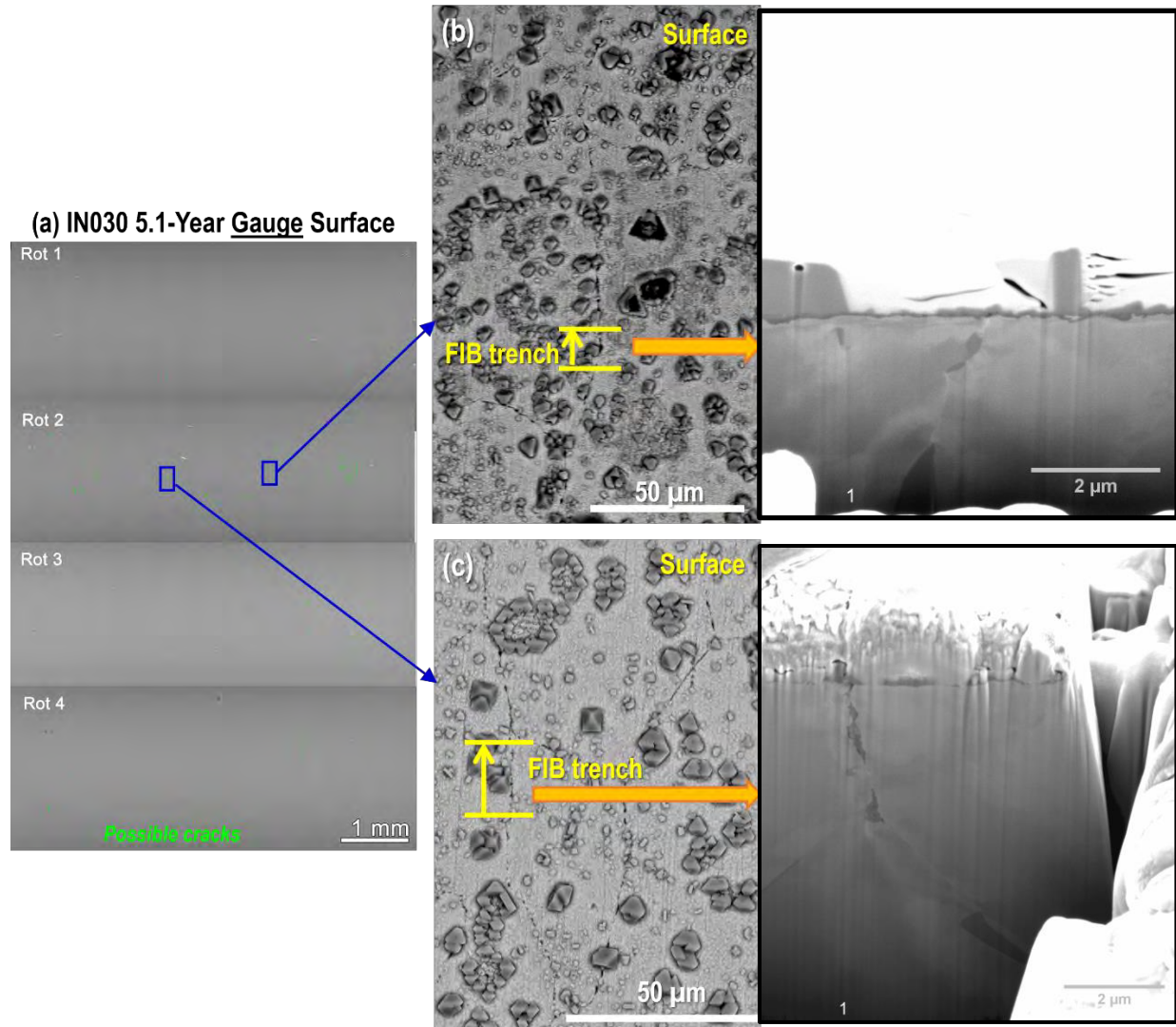


Figure 84. Distribution of possible IG cracks (marked in green) observed on the gauge surface of the TT+21.6% CF Doosan CRDM specimen IN030 tested at 100% YS after 5.1 years of exposure in 360°C simulated PWR primary water in (a). (b, c) Video of cross-sections revealed during serial FIB trenching on two possible IG cracks.

3.3.2.3 Precursor Damage Evolution in Low CW Alloy 690 Materials

Table 16 summarizes the first time short IG precursor cracks were observed in the low CW Alloy 690 materials, along with their loading condition, starting GB microstructure, and distribution of pre-existing defects produced during cold working. Upon completion of the Phase IV testing, the TT+11.7%CF Valinox CRDM specimens and GE B25K MA+12.4%CF specimens both reached 4.9 years of exposure, while the TT+12.7%CF Sumitomo CRDM specimen reached 4.1 years of exposure. Among these three materials, only one TT+11.7%CF Valinox CRDM specimen showed a surface-breaking crack of ~80 μm long on the surface. As shown in Figure 85, FIB serial milling was performed on this one and only IG crack. This time, a narrow trench was made in the middle of the crack to preserve both ends of the crack for potential growth on the surface during subsequent exposure. Cross-section morphology of the crack at the start and the end of the serial milling were shown on the upper right of Figure 85, revealing an IG crack up to 10 μm deep decorated by thick penetrative oxide along the flank but no GB cavities immediately ahead of its tip. This indicates that this crack was not formed due to GB cavity formation and

growth. The very straight appearance of this crack may suggest that it formed along an incoherent twin boundary, therefore, is an isolated SCC crack. However, further characterization is needed to confirm this hypothesis. In addition, a non-cracked GB randomly selected was also serially trenched to document sub-surface morphology. As shown in the lower right of Figure 85, this GB exhibits a series of cavities that are apparently larger and denser than the typical pre-existing damage found in this material (Figure 62), but no obvious IG damage was observed on the surface. These findings suggest that GB cavities had formed and grown in these lower CW conditions after long-term exposure to high-temperature water, albeit the kinetics appeared very slow.

Table 16. Summary of the GB microstructure, pre-existing damage, and IG precursor damage status for all the Alloy 690 materials tested in low CW conditions. Cells highlighted in orange in the last column are new observations made after Phase IV exposure.

Material	Yield/applied Stress (MPa)	AR GB Carbide Microstructure		Density of Cold Work Induced GB Damage		Time of short IG crack nucleation
		Size	Spacing	IG Voids	Cracked GB Carbides	
Valinox TT+11.7%CF	365 (1.0 YS)	50–200 nm	~100 nm	Very low	Very low	Yes (btw 4.2–4.9 yr)
Sumitomo TT+12.7%CF	405 (1.0 YS)	50–200 nm	~100 nm	Very low	Very low	No (by 4.1 yrs)
GE B25K MA+12.4%CF	510 (1.0 YS)	1–5 μm	~0.5–2 μm	None	None	No (by 4.9 yrs)

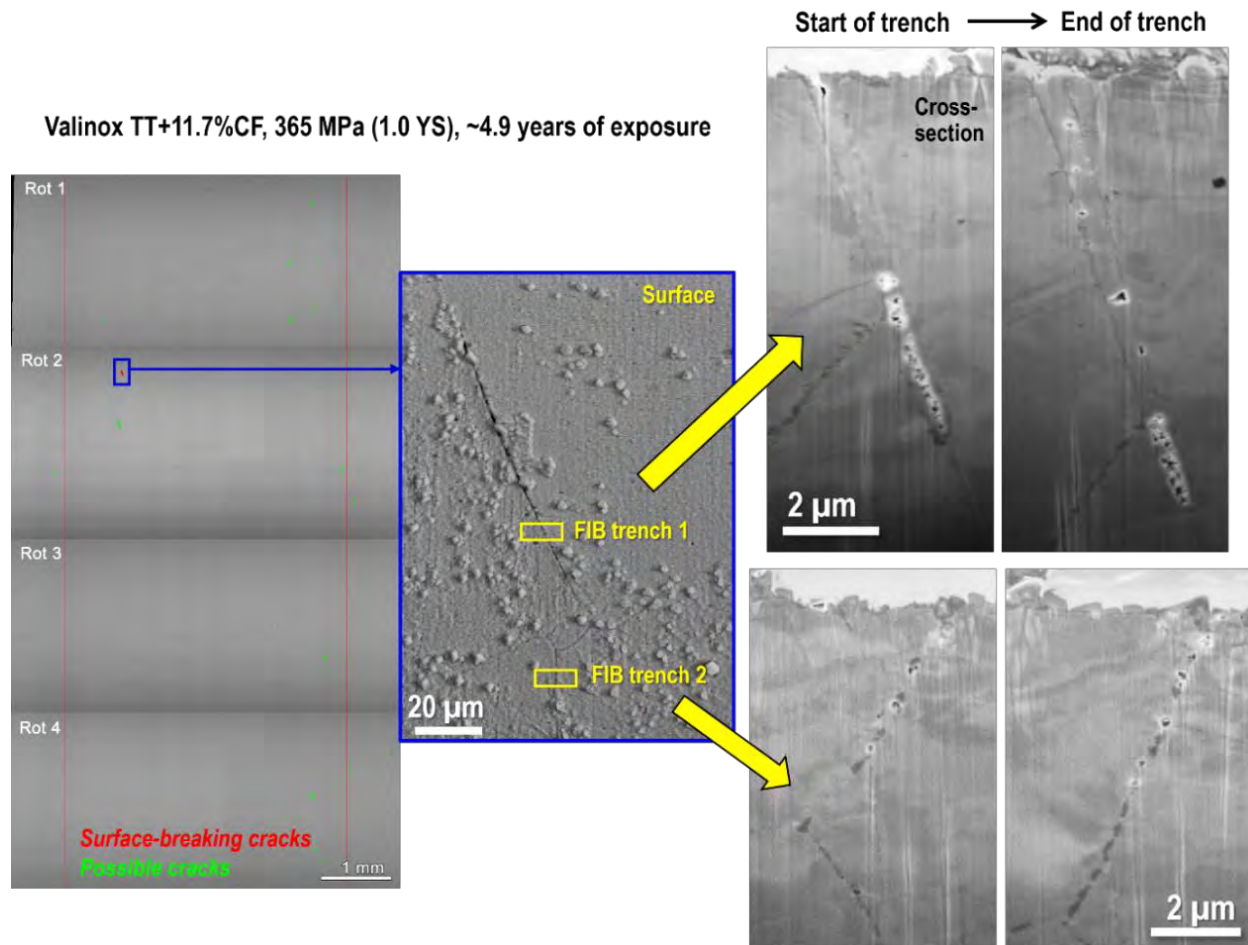


Figure 85. SEM-BSE montage images of surface-breaking IG cracks (marked in red) and possible cracks (marked in green) observed on the TT+11.7% CF Valinox CRDM specimen IN065 tested at 100% YS after 4.9 years of exposure in 360°C simulated PWR primary water (left). Selected cross-sections revealed during serial FIB trenching are also shown for one obvious crack (upper right) and one uncracked GB (lower right).

3.4 Discussion

3.4.1 Current Knowledge

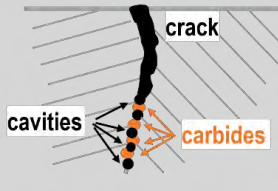
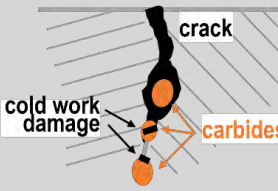
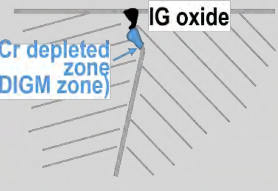
Based on the testing and characterization results accumulated over the past four phases on the long-term tested Alloy 690 SCC initiation specimens, the morphology of IG precursor damage in CW Alloy 690 can be classified into three categories and correlated to their starting GB microstructure. A schematic summary is provided in Figure 86, with key information detailed below:

- In the Alloy 690TT materials featuring a semi-continuous distribution of nanometer-sized IG carbides, IG crack initiation appears to be dominated by creep-induced GB cavity formation and growth. Nanometer-sized GB cavities could form and grow at carbide/matrix interfaces, acting as local stress concentrators and weakening GB strength, thereby accelerating the formation of IG cracks. As the test proceeds, these GB cavities would eventually link up to form multi-grain long creep cracks either intersecting the surface or deep inside the material, leading to DCPD detection of crack initiation. The kinetics of GB cavity evolution showed a strong dependence on cold work and applied stress. As shown in Figure 87, TT+31%CF Alloy 690 materials with this starting GB microstructure began to exhibit IG cracks within one year of exposure, which led to macroscopic

crack initiation detected by DCPD between 1.5–3 years of exposure. In comparison, the TT+21%CF materials just started to show small IG crack formation due to GB cavity evolution after ~4 years of exposure, but these cracks are still relatively short and confined within one-grain length and were very few in density. Meanwhile, increased GB cavities were also observed in TT+12%CF material after ~5 years of exposure, but to a much lesser extent, and no direct evidence was found to link GB cavities to crack initiation.

- In the Alloy 690TT materials featuring a semi-continuous distribution of micrometer-sized IG carbides, IG crack primarily nucleated by SCC mechanism with water ingress into the material along GBs. Cold work and applied stress appeared to have played a role, where the first short IG crack in TT+31%CF material was observed after three years of exposure and in TT+21%CF materials after five years. These cracks all exhibited thick penetrative oxides along crack flanks with no more than one grain deep (<10 μm based on limited FIB observations), indicating a much slower kinetics than those creep-induced cracks found in the first category. No macroscopic crack initiation has yet been detected by DCPD in materials in this category.
- In the Alloy 690MA or SA materials featuring little or no coverage of carbides at GBs, no IG cracks were found after up to five years of exposure, even in the highest CW condition. FIB examination on selected GBs only revealed very limited IG oxides no more than 500 nm deep, followed by a Cr-depleted zone indicative of diffusion-induced GB migration. To date, materials in this category appeared to be the most resistant to IG crack initiation.

In addition, DCPD detected macroscopic crack initiation for the first time in a TT+31%CF Sumitomo CRDM specimen tested at 90% YS during Phase IV testing after ~3.6 years of exposure (Figure 64), establishing a ~1.5–2X factor of improvement than the same material condition tested at 100% YS. Interestingly, the same heat tested in moderate CW condition at similar applied stress showed significantly slower formation of IG cracks and GB cavity aggregation (Table 15). This suggests cold work promoted cavity formation and IG cracking, likely due to a higher amount of excessive athermal vacancies produced in higher CW materials [14]. Nevertheless, an attempt was made to establish a quantitative relationship between macroscopic crack initiation time and applied stress, and the result is presented in Figure 88. A power law relationship was obtained with a stress exponent of ~2.7 between crack initiation time and applied stress. It should be noted that this extrapolation only used data from already initiated specimens, which were all in highly CW conditions. The stress exponent is expected to increase as the test continues to collect new data, and we will revisit this extrapolation in the future.

	TT with nm-sized carbides	TT with μm -sized carbides	MA & SA
			
High CW (25 – 31% CW)	<ul style="list-style-type: none"> • Many IG cracks by 1 – 3.4 yr (10s of μm deep)* • Macro-crack initiation by 1.5 – 4+ yr (GB carbide size- & spacing-dependent) 	<ul style="list-style-type: none"> • Some IG cracks by 3 yr ($\leq 10 \mu\text{m}$ deep)* • No macro-crack initiation yet 	No IG cracks yet by 4 – 5 yr
Moderate CW (18 – 22% CW)	<ul style="list-style-type: none"> • A few IG cracks by 4 yr ($\leq 10 \mu\text{m}$ deep)* • No macro-crack initiation yet 	<ul style="list-style-type: none"> • Some IG cracks by 5 yr ($\leq 10 \mu\text{m}$ deep)* • No macro-crack initiation yet 	No IG cracks yet by 5 yr
Low CW (~12% CW)	<ul style="list-style-type: none"> • A few IG cracks by 5 yr ($\leq 10 \mu\text{m}$ deep)* • No macro-crack initiation yet 	Not tested	No IG cracks yet by 4 – 5 yr

*Based on limited FIB trenching on obvious cracks

Figure 86. Summary of precursor morphology and crack mechanism observed in the long-term tested CW Alloy 690 SCC initiation specimens as a function of starting microstructure and cold work level.

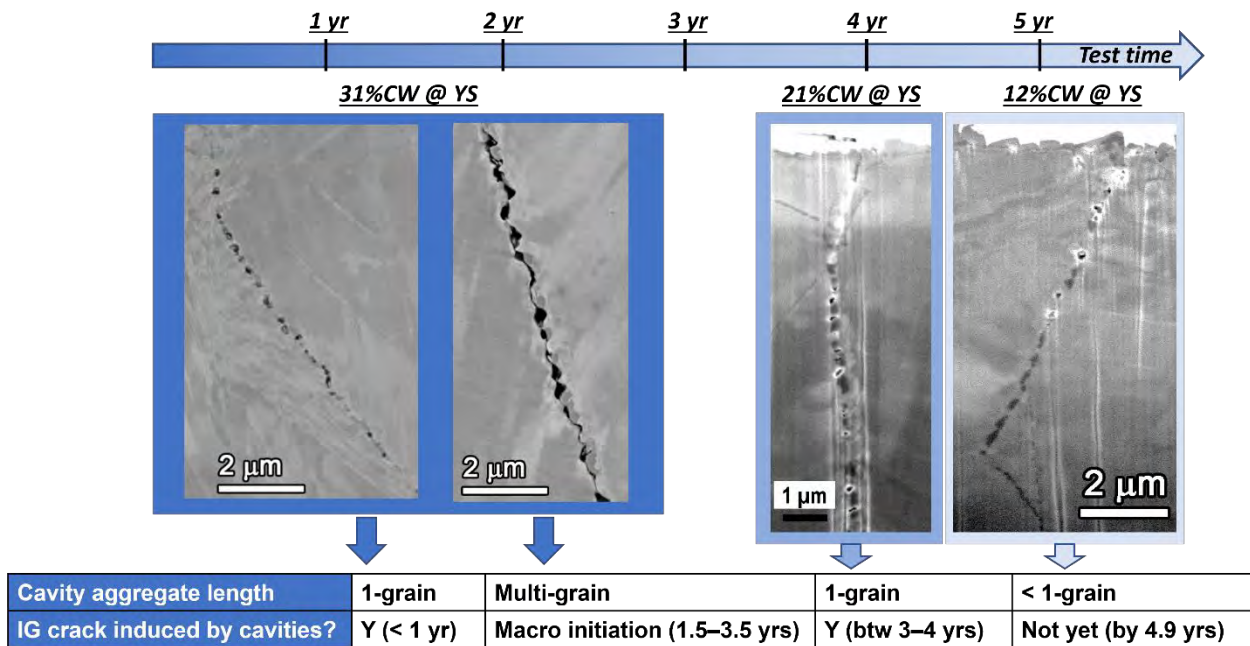


Figure 87. The first occurrence of surface-breaking IG cracks observed in the Alloy 690TT Valinox CRDM material as a function of exposure time. Key characteristics of the cracks were also summarized.

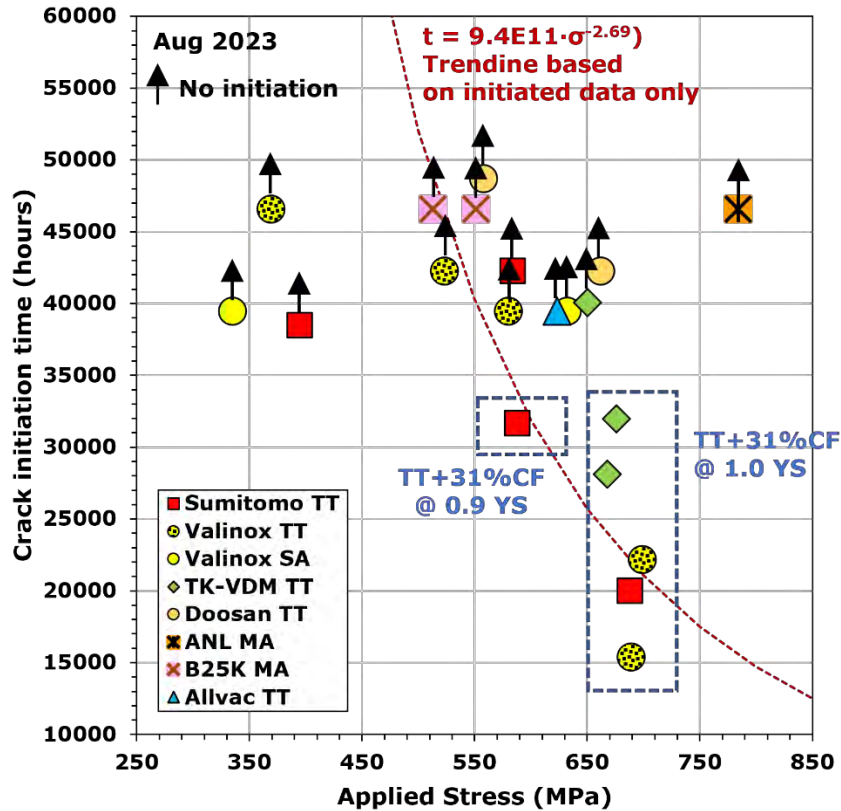


Figure 88. Crack initiation or total exposure time of all the tested Alloy 690 materials as a function of applied stress.

3.4.2 Future Plans

After Phase IV exposure, the characterization confirmed that an increase in GB cavity size and density had occurred in moderately and low CW Alloy 690TT materials featuring a semi-continuous distribution of nanometer-sized carbides. Alloy 690TT materials are commonly used in service and could experience a similar degree of cold work induced by installation and welding. While extensive laboratory testing has demonstrated high resistance to SCC propagation in these lower CW Alloy 690TT materials, the recent observations posed a concern on whether creep-induced GB cavity evolution can lead to macroscopic cracking in Alloy 690 after long-term service. Therefore, future investigation will focus on evaluating the kinetics of cavity evolution and determine whether they would lead to crack initiation in lower CW Alloy 690TT materials in service-relevant conditions. Three tasks will be conducted concurrently to achieve this goal. First, we will continue the long-term SCC initiation testing on CW Alloy 690 materials for at least two more years to collect crack initiation data and evaluate precursor damage evolution. Secondly, we have begun a series of air creep tests on one Alloy 690TT heat featuring the most susceptible starting microstructure to cavity formation at three different temperatures (330, 360, and 400°C). The outcome of this task will help us assess the influence of the water environment on material creep behavior and establish a thermal activation energy for creep-induced crack initiation in Alloy 690TT to better correlate the crack initiation time obtained in 360°C PWR primary water to more service-relevant operating temperatures (~320°C). Finally, GB cavity distribution will be quantified on samples removed at different test phases. The results will be used together with new data obtained from the first two tasks to develop a statistical model to predict crack initiation time in Alloy 690TT materials as a function of key material, environmental, and mechanical factors.

4. Summary and Conclusions

The first part of this report summarized the final year's progress of a three-year research effort on evaluating the SCC initiation and growth behavior of Ni-base alloys in LiOH vs. KOH-containing PWR primary water. In FY 2023, this study focused on a first-generation Ni-base weld metal Alloy 82. Six Alloy 82 initiation specimens were tested at yield stress in 360°C PWR primary water BOC chemistry containing 1500 ppm B and either 2.2 ppm Li or 12.4 ppm K (i.e., molar-equivalent concentrations of KOH or LiOH to achieve neutral pH at 310°C). A DCPD technique was used for in-situ detection of SCC initiation time in these specimens. All specimens exhibited relatively fast SCC initiation within ~700 hours of exposure, except one specimen that did not initiate after the test ended at 2152 hours. This was believed to be primarily due to intrinsic microstructural variability within the material. In addition, specimens loaded up to a similar degree of plastic strain often exhibited similar SCC initiation times, whether tested in KOH- or LiOH-containing PWR primary water. Meanwhile, SCC growth behavior was evaluated on two 30%CF Alloy 82 CT specimens in the T-S orientation using in-situ measurement of crack extension by a highly refined DCPD method. SCCGR on the two specimens were measured during on-the-fly changes between LiOH and KOH to the content specified by EPRI for the BOC, EOC, and mid-cycle PWR primary water chemistries. In the BOC and EOC water chemistries, the assessment usually began with LiOH, proceeded to KOH, and then returned to LiOH to confirm behavior. SCCGRs were collected right before and after each water chemistry change and after the crack had spent a sufficiently long time in each specified water chemistry so that an average SCCGR could be determined. Comparing these data revealed no obvious change in SCCGR in KOH vs. LiOH in each water chemistry, nor on shifting from BOC, EOC, to mid-cycle water chemistries. These observations marked the completion of the LiOH vs. KOH SCC study to facilitate the EPRI's KOH qualification program. Together with the results obtained previously on Alloy X-750 and Alloy 718, it is concluded that replacing LiOH with KOH would not adversely impact the SCC initiation or growth susceptibility of Ni-base alloys and weld metals in PWR primary water.

The second part of this report provides a status update of the ongoing Phase V long-term SCC initiation testing on CW Alloy 690 materials, where the effect of key material, mechanical, and environmental factors on the long-term GB degradation and crack initiation behavior of Alloy 690 are being evaluated in state-of-the-art SCC initiation testing systems equipped with in-situ detection of macroscopic crack initiation. A detailed summary was also provided on the microscopy analyses performed in FY 2023 to evaluate precursor damage and crack evolution in all tested Alloy 690 specimens after Phase IV exposure. Macroscopic crack initiation was detected for the first time in a TT+31%CF Alloy 690 Sumitomo specimen loaded at 90% YS after 3.6 years of exposure and was confirmed to be caused by creep-induced GB cavity evolution after long-term testing. This is consistent with what was found previously in the same material tested at 100% YS, establishing a factor of improvement of ~1.5–2X in crack initiation when applied stress was reduced from 100% to 90% YS. In addition, increases in GB cavity size and density were confirmed for the first time in lower CW Alloy 690TT materials and have been demonstrated to cause small IG crack nucleation in one specimen, raising concern on whether the creep-induced GB cavity evolution could lead to macroscopic cracking in Alloy 690 after long-term service. As of the writing of this report, the long-term SCC initiation testing has been resumed, and complementary air creep tests on selected Alloy 690TT materials have begun with the aim of better defining the mechanism and kinetics of GB cavity evolution and collecting quantitative data that will be used for predicting Alloy 690 degradation in realistic operating conditions.

REFERENCES

- [1] Z. Zhai, M. B. Toloczko, F. Cintron-Colon and R. A. Bouffieux, *Evaluation of Stress Corrosion Cracking Behavior of Ni-Base Alloys in PWR Primary Water Containing KOH vs. LiOH*. Pacific Northwest National Laboratory: Technical Milestone Report M2LW-21OR0402036, Light Water Reactor Sustainability Program, DOE Office of Nuclear Energy, September 2021.
- [2] Z. Zhai, M. Toloczko, F. Cintron-Colon and R. A. Bouffieux, *Stress Corrosion Cracking of Ni-Base Alloys in PWR Primary Water Containing KOH vs. LiOH*. Pacific Northwest National Laboratory: Technical Milestone Report M3LW-22OR0402033, Light Water Reactor Sustainability Program, DOE Office of Nuclear Energy, July 2022.
- [3] P. L. Andresen, I. P. Vasatis and F. P. Ford, "Behavior of short cracks in stainless steel at 288°C", in *CORROSION 1990*, Las Vegas, Nevada, USA.
- [4] E. Richey, D. S. Morton and M. K. Schurman, "SCC initiation testing of nickel-based alloys using in-situ monitored uniaxial tensile specimens", in *12th International Conference on Environmental Degradation of Materials in Nuclear Power Systems - Water Reactors*, 2005, Salt Lake City, UT, USA: The Minerals, Metals & Materials Society.
- [5] Z. Zhai, M. B. Toloczko, M. J. Olszta and S. M. Bruemmer, "Stress corrosion crack initiation of alloy 600 in PWR primary water", *Corrosion Science*, Vol.123, 2017, pp. 76-87.
- [6] S. M. Bruemmer, M. J. Olszta, D. K. Schreiber and M. B. Toloczko, *Stress Corrosion Crack Initiation of Cold-Worked Alloy 600 and Alloy 690 in PWR Primary Water*. Pacific Northwest National Laboratory: Technical Milestone Report M2LW-14OR0404023, Light Water Reactor Sustainability Program, DOE Office of Nuclear Energy, September 2014.
- [7] M. B. Toloczko, N. R. Overman, M. J. Olszta and S. M. Bruemmer, *Pacific Northwest National Laboratory Investigation of Stress Corrosion Cracking in Nickel-Base Alloys, Volume 3: Stress Corrosion Cracking of Cold-Worked Alloy 690*. Pacific Northwest National Laboratory: NUREG/CR-7103 Vol. 3, Nuclear Regulatory Commission, Office of Nuclear Regulatory Research, 2015.
- [8] P. Chou, J. Smith, A. Demma, M. Burke and K. Fruzzetti, "Potassium Hydroxide for PWR Primary Coolant pH Control: Materials Qualification Testing", in *21st NPC International Conference on Water Chemistry in Nuclear Reactor Systems*, San Francisco, CA, U.S.A., September 9–14, 2018.
- [9] M. B. Toloczko, Z. Zhai, J. Wang, M. J. Olszta and R. A. Bouffieux, *Materials Reliability Program: Stress Corrosion Crack (SCC) Initiation Testing of Ni-Base Alloys for PWR Applications Part 2 (MRP-448)*, EPRI Report #3002018002. June 2021.
- [10] M. B. Toloczko, M. J. Olszta, Z. Zhai and S. M. Bruemmer, "Stress corrosion crack initiation measurements of alloy 600 in PWR primary water", in *17th International Conference on Environmental Degradation of Materials in Nuclear Power Systems - Water Reactors*, 2015, Ottawa, ON, Canada: Canadian Nuclear Society.
- [11] Z. Zhai, M. J. Olszta, M. B. Toloczko and S. M. Bruemmer, *Summary of Stress Corrosion Crack Initiation Measurements and Analyses on Alloy 600 and Alloy 690*. Pacific Northwest National Laboratory: Technical Milestone Report M2LW-15OR0402034, Light Water Reactor Sustainability Program, DOE Office of Nuclear Energy, September 2015.
- [12] K. Arioka, "2014 Whitney Award Lecture: Change in Bonding Strength at Grain Boundaries before Long Term SCC Initiation", *Corrosion*, Vol.71, Iss.4, 2015, pp. 403-419.
- [13] K. Arioka, T. Miyamoto, T. Yamada and M. Aoki, "Role of Cavity Formation in Crack Initiation of Cold-Worked Carbon Steel in High-Temperature Water", *Corrosion*, Vol.69, Iss.5, 2013, pp. 487-496.
- [14] K. Arioka, T. Yamada, T. Miyamoto and T. Terachi, "Dependence of Stress Corrosion Cracking of Alloy 690 on Temperature, Cold Work, and Carbide Precipitation—Role of Diffusion of Vacancies at Crack Tips", *Corrosion*, Vol.67, Iss.3, 2011, pp. 035006-035001-035006-035018.

- [15] K. Arioka, R. W. Staehle, T. Yamada, T. Miyamoto and T. Terachi, "Degradation of Alloy 690 After Relatively Short Times", *Corrosion*, Vol.72, Iss.10, 2016, pp. 1252-1268.
- [16] Z. Zhai, M. Toloczko, K. Kruska and S. Bruemmer, "Precursor Evolution and Stress Corrosion Cracking Initiation of Cold-Worked Alloy 690 in Simulated Pressurized Water Reactor Primary Water", *Corrosion*, Vol.73, Iss.10, 2017, pp. 1224-1236.
- [17] Z. Zhai, M. Toloczko, K. Kruska, D. Schreiber and S. Bruemmer, "Grain Boundary Damage Evolution and SCC Initiation of Cold-Worked Alloy 690 in Simulated PWR Primary Water", in *Proceedings of the 18th International Conference on Environmental Degradation of Materials in Nuclear Power Systems – Water Reactors: Volume 1*, J. H. Jackson, D. Paraventi and M. Wright, Editors. 2018, Springer International Publishing: Cham, pp. 457-483.
- [18] Z. Zhai, M. B. Toloczko, K. Kruska, D. K. Schreiber, M. J. Olszta, N. R. Overman and S. Bruemmer, *Precursor damage evolution and stress corrosion crack initiation of cold-worked alloy 690 in PWR primary water*. Pacific Northwest National Laboratory: Technical Milestone Report M2LW-16OR0402034, Light Water Reactor Sustainability Program, DOE Office of Nuclear Energy, September 2016.
- [19] Z. Zhai, M. B. Toloczko and S. M. Bruemmer, *Stress corrosion crack initiation behavior of Alloy 600 and Alloy 690 in PWR primary water*. Pacific Northwest National Laboratory: Technical Milestone Report M2LW-18OR0402034, Light Water Reactor Sustainability Program, DOE Office of Nuclear Energy, September 2018.
- [20] Z. Zhai, M. B. Toloczko, M. J. Olszta and S. M. Bruemmer, *Grain boundary microstructure effects on stress corrosion crack initiation mechanisms in Alloy 600 and Alloy 690*. Pacific Northwest National Laboratory: Technical Milestone Report M2LW-19OR0402031, Light Water Reactor Sustainability Program, DOE Office of Nuclear Energy, September 2019.
- [21] Z. Zhai, M. J. Olszta, M. B. Toloczko and S. M. Bruemmer, *Long-term crack initiation behavior of Alloy 690 and its weld metals in PWR primary water*. Pacific Northwest National Laboratory: Technical Milestone Report M3LW-20OR0402037, Light Water Reactor Sustainability Program, DOE Office of Nuclear Energy, April 2020.
- [22] S. M. Bruemmer, M. B. Toloczko and M. J. Olszta, *Pacific Northwest National Laboratory Investigation of Stress Corrosion Cracking in Nickel-Base Alloys, Volume 2*. Pacific Northwest National Laboratory: NUREG/CR-7103 Vol. 2, Nuclear Regulatory Commission, Office of Nuclear Regulatory Research, 2012.
- [23] Z. Zhai, M. J. Olszta and M. B. Toloczko, *Quantitative Analysis of Precursor Damage and Crack Evolution in Alloy 690 and Its Weld Metals after Long-Term SCC Initiation Testing in PWR Primary Water*. Pacific Northwest National Laboratory: Technical Milestone Report M3LW-21OR0402033, Light Water Reactor Sustainability Program, DOE Office of Nuclear Energy, April 2021.
- [24] M. J. Olszta, D. K. Schreiber, M. B. Toloczko and S. M. Bruemmer, "High resolution characterization of film formation and localized corrosion in alloy 690 exposed to PWR primary water", in *Corrosion 2014*, 2014, San Antonio, Texas, USA: NACE International.